

A Preliminary Quantitative Systems Pharmacology (QSP) Model of Immune Interactions along the ‘Gut-Lung Axis’

A Thesis

submitted towards partial fulfilment of the requirements for the BS-MS Dual Degree programme in the Indian Institute of Science Education and Research (IISER) Pune

Submitted by

Madheshvaran S
20181144



Research Mentor

Dr Farnoush Farahpour
Faculty of Biology
Center for Medical Biotechnology
Universität Duisburg-Essen

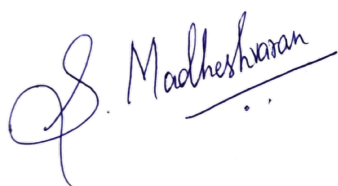
Thesis Advisor

Leelavati Narlikar
Associate Professor and Deputy Chair
Department of Data Science
IISER Pune

April 2023

Certificate

This is to certify that this dissertation entitled “**A Preliminary Quantitative Systems Pharmacology (QSP) Model of Immune Interactions along the ‘Gut-Lung Axis’**” towards the partial fulfilment of the BS-MS dual degree programme at the Indian Institute of Science Education and Research (IISER), Pune represents original research carried out by **Madheshvaran S** at Universität Duisburg-Essen, Essen, Germany under the supervision of **Dr Farnoush Farahpour**, Faculty of Biology, Center for Medical Biotechnology, Universität Duisburg-Essen, Essen, Germany during the academic year 2022-2023.



Madheshvaran S
(Student)
20181144
Fifth Year BS-MS Student
IISER Pune



Dr Farnoush Farahpour
(Supervisor)
Faculty of Biology
Center for Medical Biotechnology
Universität Duisburg-Essen, Essen

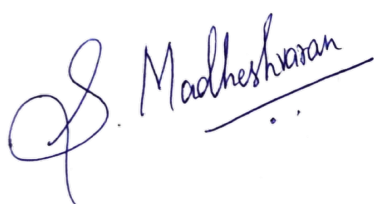


Prof Dr Leelavati Narlikar
(Expert)
Associate Professor and Deputy Chair
Department of Data Science
IISER Pune

This thesis is dedicated to my parents and my sister
for pushing me to pursue my aspirations and always supporting me
for one, will never forget the sacrifices they made

Declaration

I, hereby declare that the matter embodied in the report titled “**A Preliminary Quantitative Systems Pharmacology (QSP) Model of Immune Interactions along the ‘Gut-Lung Axis’**” is the results of the investigations carried out by me at the Group of Bioinformatics and Computational Biophysics, Center for Medical Biotechnology, Universität Duisburg-Essen from the period June 2022 to April 2023 under the supervision of **Dr Farnoush Farahpour**, Faculty of Biology, Center for Medical Biotechnology, Universität Duisburg-Essen and the same has not been submitted elsewhere for any other degree.



Madheshvaran S

(Student)

20181144

Fifth Year BS-MS Student

IISER Pune



Dr Farnoush Farahpour

(Supervisor)

Faculty of Biology

Center for Medical Biotechnology

Universität Duisburg-Essen, Essen

Table of Contents

Certificate	1
Declaration	3
Table of Contents	4
List of Tables	6
List of Figures	7
Abstract	9
Abbreviations	10
Acknowledgements	11
Contributions	12
1. Introduction	13
1.1. Gut Microbiome	13
1.2. Lung Cancer and Radiation Therapy	13
1.3. Gut-Lung Axis	15
1.4. Gut-Lung Axis in the context of Radiation Therapy	16
1.5. Computational Modelling to Understand the Gut-Lung Axis	17
1.6. Introduction to Quantitative Systems Pharmacology (QSP) Modelling	19
1.7. Quantitative Systems Pharmacology (QSP) model of the Gut-Lung Axis ...	21
1.8. Hypothesis	22
1.9. Aim	23
1.10. Objectives	23
2. Methods and Materials	24
2.1. Computational Methods	24
2.1.1. Model Formulation	24
2.1.2. Model Evaluation	27
2.1.3. Parameter Sensitivity Analysis	27
2.2. Experimental Methods	28
2.2.1. Mice	28
2.2.2. Isolation of Blood and Serum	28
2.2.3. Isolation of Lung Cells	29
2.2.4. Isolation of Spleen Cells	29

2.2.5.	Isolation of Cells from Lymph Nodes	30
2.2.6.	Flow Cytometric Staining	30
3.	Results	33
3.1.	Gut Compartment.....	33
3.1.1.	Formulation of Gut model	33
3.1.2.	Simulation of Gut Model	36
3.1.3.	Sensitivity Analysis of Gut Model.....	39
3.1.4.	Preliminary Evaluation of Gut Model	41
3.2.	Lung Compartment	43
3.2.1.	Formulation of Lung Model.....	43
3.2.2.	Simulation of Lung Model	45
3.2.3.	Sensitivity Analysis of the Lung Model.....	47
3.2.4.	Simulation of the Diseased Mode of the Lung Model	49
3.2.5.	Flow Cytometric Data of Immune Populations from Mice	52
3.3.	Gut-Lung Axis (GLA) Model	57
3.3.1.	Formulation of the GLA Model.....	57
3.3.2.	Simulation of the GLA Model	58
3.3.3.	Sensitivity Analysis of the GLA Model.....	60
3.3.4.	Simulation of the Sustained Gut Inflammation of the GLA Model	61
3.3.5.	Effect of the Sustained Gut Inflammation on the Sensitivity Factor of Inflammatory Cell Death in Lung	65
4.	Discussion.....	67
5.	Bibliography	72
6.	Appendix	79
6.1.	Appendix 1: List of State Variables and Parameters for ‘Gut-Lung Axis’ Model.....	79
6.2.	Appendix 2: List of Weighted Parameters for CD and UC modes of the Gut model.....	92
6.3.	Appendix 3: Simulation of Gut Model	93
6.4.	Appendix 4: Sensitivity Analysis of Gut Model.....	94
6.5.	Appendix 5: Simulation of Lung Model.....	96
6.6.	Appendix 6: Sensitivity Analysis of Lung Model	97
6.7.	Appendix 7: Flow Cytometric Data of Immune Populations from Mice	99
6.8.	Appendix 8: Sensitivity Analysis of Gut-Lung Axis Model.....	101

List of Tables

Table 1: Composition of ACK Buffer (for 1 L, pH 7.2 - 7.4)	29
Table 2: Composition of FACS Buffer (for 50 ml)	30
Table 3: Composition of Fix-Perm-Solution	31
Table 4: Composition of Perm-Buffer	31
Table 5: List of antibodies used for flow cytometric straining	31
Table 6: Summary of flow cytometric measurements of different immune cell populations from mice.	56
Table 7: List of all state variables (species) in the GLA model	80
Table 8: List of all parameters in GLA model	91
Table 9: List of weighted parameters for CD and UC modes of the Gut model	92
Table 10: Description of the top 25 sensitive parameters from the sensitivity analysis of CRP in blood of the Gut model	94
Table 11: Description of the top 25 sensitive parameters from the sensitivity analysis of gut activated neutrophils of the Gut model	95
Table 12: Description of the top 20 sensitive parameters from the sensitivity analysis of CRP in blood of the Lung model	97
Table 13: Description of the top 20 sensitive parameters from the sensitivity analysis of SPD in blood of the Lung model	98
Table 14: Description of the top 20 sensitive parameters from the sensitivity analysis of damaged alveolar AT2 cells of the Lung model	98
Table 15: Calculations of immune cell population in different tissues of the individual mice samples.	100
Table 16: Description of the top 25 sensitive parameters from the sensitivity analysis of CRP in blood of the Gut-Lung Axis model	101
Table 17: Description of the top 25 sensitive parameters from the sensitivity analysis of SPD in blood of the Gut-Lung Axis model	102

List of Figures

Figure 1: Schematic explaining the processes involved in the 'Gut-Lung Axis'.	16
Figure 2: Steps involved in the QSP modelling.	21
Figure 3: The simplified diagram of the QSP model of the 'gut-lung axis.'	24
Figure 4: Emission and Excitation spectrums of fluorophores used in lymphocytes staining.....	32
Figure 5: Overview of the mechanistic structure of the Gut compartment.	34
Figure 6: Time Evolution of species in HV, CD and UC modes of the gut model.....	37
Figure 7: Steady state values of CRP in blood and activated neutrophils in gut for the HV, CD and UC modes of the Gut model.	38
Figure 8: Sensitivity Analysis of CRP in blood and activated gut neutrophils.	40
Figure 9: Comparison of steady-state values of species from HV mode of the Gut model with experimental data.....	42
Figure 10: Overview of the mechanistic structure of the Lung compartment.	44
Figure 11: Time Evolution of species in the lung model upon radiation.	46
Figure 12: Sensitivity Analysis of CRP, SPD and damaged AT2 cells in the Lung model.	48
Figure 13: Time Evolution of species in the normal and radiation sensitive mode of the lung model upon radiation.	51
Figure 14: Gating Strategy for myeloid cells.....	52
Figure 15: Gating Strategy for alveolar and interstitial macrophages.	53
Figure 16: Gating Strategy for Lymphocytes.	54
Figure 17: Gating Strategy for Dendritic Cells (DCs).....	55
Figure 18: Simplified overview of the mechanistic structure of the Gut-Lung Axis model.	57
Figure 19: Time Evolution of $TNF\alpha$ and $TGF\beta$ in different compartments for the normal and radiation sensitive mode of the GLA model upon radiation.	59
Figure 20: Sensitivity Analysis of CRP and SPD in the GLA model.....	61
Figure 21: Time Evolution of species in the normal and radiation sensitive mode of the GLA model with normal or sustained gut inflammation upon radiation.	64
Figure 22: Steady-state value of CRP for different factor values of radiation sensitive virtual patient with healthy and inflamed gut environment.	66

Figure 23: Time Evolution of immune cell population and cytokines for the Gut model.	93
Figure 24: Time Evolution of pulmonary alveolar population, immune cell population and cytokines for the Lung model.	96

Abstract

The microbiome has been associated with maintaining normal human homeostasis and physiological functions. Numerous studies indicate that the gut microbiome and its related metabolites influence pulmonary immune homeostasis and lung physiology, and conversely, local respiratory tract processes are involved in the distal modulation of gut mucosal immune system. Additionally, the gut dysbiosis is associated with outcomes of radiation therapy for lung cancer and complications associated with radiotherapy such as radiation-induced pneumonitis and radiation fibrosis. The causation behind these associations is poorly understood and still speculative, although emerging experimental evidence indicates that the crosstalk of the gut microbiome and the lungs is primarily mediated through metabolism-related genotoxicity, defective immunosurveillance, and systemic inflammation. This bidirectional communication channel between the gut and the lung immune system is referred to as the gut-lung axis. Understanding this phenomenon in humans has been a challenge due to practical and ethical concerns associated with human experimentation. Computational models have recently been used to tackle this challenge, providing researchers with new tools to study immuno-oncology related problems. We aim to develop a Quantitative Systems Pharmacology (QSP) model that incorporates detailed mechanisms for important immune interactions along the gut-lung axis. The model comprises three compartments (gut, lungs, and blood) and the relevant cellular pathways, including replication, migration, and apoptosis of various immune cell types and production, transportation, and degradation of cytokines and inflammatory biomarkers. The model allows testing new hypotheses to understand the gut microbiome's influence on radiotherapy and radiation pneumonitis. Using parameter perturbation to simulate the response of inflammatory biomarkers, the model captured the biological heterogeneity associated with the onset and dynamics of radiation pneumonitis. With additional experimental validation, the model can enable researchers to examine the complex microbiome-associated immune responses and how the dysregulation of these processes may contribute to the pathobiology of the disease.

Abbreviations

QSP – Quantitative Systems Pharmacology

GLA – Gut Lung Axis

IBD – Inflammatory Bowel Disease

RT – Radiation Therapy

ODE – Ordinary Differential Equation

Vpop – Virtual Population

SC – Sensitivity Coefficient

CRP – C-reactive protein

SPD – Surfactant protein D

SS – Steady State (of the model)

HV – Healthy Volunteers

CD – Crohn's Disease

UC – Ulcerative Colitis

GI – Gastrointestinal

DAMPs – Damage-Associated Molecular Patterns

TGF- β /TGFB – Transforming Growth Factor-Beta

TNF- α /TNF α - Tumour Necrosis Factor Alpha

IL-x – Interleukin x (x is a number)

AT1/2 - Pulmonary alveolar type I/II

BALF – Bronchoalveolar Lavage Fluid

Acknowledgements

I would like to express my most profound appreciation to all those who provided me with the chance to work and learn despite the restrictions implemented in India and Germany due to the pandemic.

I am deeply indebted to **Dr Farnoush Farahpour**, who in spite of being extraordinarily busy with her duties, took time out to hear, guide and keep me on the correct path throughout the project. I am immensely thankful to her for taking me into her group as a master's project student notwithstanding the pandemic restrictions, and for her careful and valuable guidance and advice, which were extremely valuable for the execution and completion of my project.

I express my special gratitude to **Prof Dr Leelavati Narlikar** for agreeing to be an expert on my master's thesis advisory committee and for giving me great feedback and suggestions during my mid-year presentation.

I also express my deepest thanks to **Prof Dr Daniel Hoffmann** and **all lab members** of the Bioinformatics and Computational Biophysics group who provided constructive criticisms on my project and helped me to learn the technical aspects in the lab, and supported me whenever I needed it.

I'm extremely grateful to **Prof Dr Verena Jendrossek** and **Prof Dr Astrid Westendorf** for their valuable guidance and biological expertise, without which this project wouldn't have come to fruition. I also would like to thank for the continual support of **Dr Florian Wirsdörfer**, **Dr Alexandra Adamczyk** and **members of their labs** for their great advice and opinion, and providing experimental data to aid my thesis work.

I would like to acknowledge Deutscher Akademischer Austauschdienst (DAAD) and Deutsche Forschungsgemeinschaft (DFG) for providing financial support for the project, and especially the former for helping me expedite the German visa application. I would like to extend my sincere thanks to the Indian Institute of Science Education and Research, Pune, and Kishore Vaigyanik Protsahan Yojana (KVPY) for allowing me to study and delve into research during my undergraduate years.

Contributions

Contributor name	Contributor role
Dr Farnoush Farahpour Prof Dr Verena Jendrossek Prof Dr Astrid Westendorf	Conceptualization Ideas
Dr Farnoush Farahpour	Methodology
Dr Farnoush Farahpour Lara Schmalenstroer	Software
-	Validation
-	Formal analysis
Dr Florian Wirsdörfer Mario Hetzel	Investigation
Prof Dr Daniel Hoffmann Dr Florian Wirsdörfer Dr Alexandra Adamczyk	Resources
Dr Florian Wirsdörfer Dr Alexandra Adamczyk	Data Curation
-	Writing - original draft preparation
-	Writing - review and editing
-	Visualization
Dr Farnoush Farahpour	Supervision
Dr Farnoush Farahpour	Project administration
Deutscher Akademischer Austauschdienst (DAAD) and Deutsche Forschungsgemeinschaft (DFG)	Funding acquisition

1. Introduction

This introductory chapter first gives an overview of the biological concepts behind the ‘gut-lung axis.’ Subsequently, the chapter describes the motivation for this thesis and finishes with the aim and objectives of the thesis.

1.1. Gut Microbiome

The gastrointestinal (GI) tract is a host to a highly complex microbial ecosystem, comprising approximately 10^{14} bacteria, viruses and archaea of more than 1,000 species (Lv *et al.*, 2019). This collective genome of the microorganisms living in the gut is called as the gut microbiome. The microbial communities in the gut microbiome coexist with the host in a mutually beneficial symbiotic relationship. While the microbes benefit from a nutrient-rich, protective, and stable environment from the host, in return, they play a critical role in performing and maintaining a considerable number of the host’s physiological functions, including host metabolism (Fabbiano *et al.*, 2018), brain function (Rogers *et al.*, 2016), and host immunity (Valdes *et al.*, 2018). An emerging area of great interest is understanding the effect of the gut microbiome on local and systemic immune homeostasis. Dysbiosis of the gut microbiome is associated locally with various gastrointestinal diseases such as inflammatory bowel disease (Glassner *et al.*, 2020) and colorectal cancer (Wong and Yu, 2019), but also systematically with other diseases such as obesity (Valdes *et al.*, 2018), diabetes mellitus (Zhang *et al.*, 2021), acquired immunodeficiency syndrome (Kehrmann *et al.*, 2019), SARS-CoV-2 (Reinold *et al.*, 2021, 2022), lung cancer (Liu *et al.*, 2020) and neuroinflammatory conditions like multiple sclerosis, Alzheimer’s and Parkinson’s diseases (Rutsch *et al.*, 2020).

1.2. Lung Cancer and Radiation Therapy

Lung cancer is a type of cancer characterised by uncontrolled cell growth in the lung tissues. It is one of the most commonly diagnosed forms of cancer, with an incidence rate of 11.4% of total cancer cases (Sung *et al.*, 2021). Despite the recent advances in diagnosis and treatment, patients’ overall survival is still poor, and thus, lung cancer has remained by far the leading cause of cancer death in 2020 in both sexes, with a mortality rate of about 18.0% and an estimated 1.8 million deaths worldwide (Sung *et al.*, 2021). Although there are a variety of treatment options for lung cancer, including

chemotherapy, radiotherapy, and immunotherapy, which are selected depending on the patient's TNM stage and individual health circumstances, the majority of patients are diagnosed at an advanced stage and are left with few limited treatment options leading to a high mortality rate (Thai *et al.*, 2021). Therefore, there is a growing demand and interest in understanding the mechanisms of carcinogenesis and cancer progression and to explore new treatment strategies and therapeutics for this disease.

One particular interest is in radiation therapy (or radiotherapy); more than 60% of all cancer patients receive radiotherapy during the course of their disease (Tyldesley *et al.*, 2001). However, not all patients benefit from this treatment: some respond poorly to such therapy due to factors such as intrinsic radio-resistance and tumour-promoting mutations which adversely affect the response of tumour cells to radiotherapy (Baumann *et al.*, 2016; Herbst *et al.*, 2018), while others develop acute and late tissue toxicity such as radiation-induced pneumonitis and radiation fibrosis after the treatment which can be caused by excessive immune system activation (Jarzebska *et al.*, 2021). Although there have been technological improvements in delivering the radiation dose more accurately to the tumour, it is still inevitable that some normal lung tissue adjacent to the tumour will also be exposed to ionising radiation during the treatment. This exposure to ionising radiation causes death and damage of resident lung epithelial and endothelial cells, resulting in activation of damage-associated responses, which includes increased production of cytokines and growth factors and increased recruitment of immune cells in the damaged microenvironment (Wirsdörfer and Jendrossek, 2016). If this pro-inflammatory response is too excessive, patients may develop clinical symptoms of pneumonitis, mostly at 3 to 12 weeks after the radiation therapy (Graves *et al.*, 2010). This emergence of chronic inflammation after radiation therapy is called radiation-induced pneumonitis, and this can result in hypoxia, fibroblasts recruitment and activation in the environment and excessive deposits of extracellular matrix in the lung tissue, eventually leading to lung fibrosis in the late phase of the radiation-induced lung injury (Jarzebska *et al.*, 2021). The current primary strategy to minimise radiation-induced pulmonary fibrosis is to lower the radiation dose delivered, which may lead to decreased treatment efficacy (Schaue *et al.*, 2015).

1.3. Gut-Lung Axis

Numerous studies have indicated that the microbiome have associations with pulmonary physiology and homeostasis (Gopalakrishnan et al., 2018; Zhuang et al., 2019), and a growing consensus suggests that the GI tract and the lungs share a mucosal immune system regulating various processes in both organs (Rooks and Garrett, 2016). This presence of a bidirectional communication channel between the gut and the lung mucosal immune system is referred to as the 'gut-lung axis' (Budden et al., 2016), as shown in Figure 1. Emerging experimental evidence suggests that the gut microbiome and its related metabolites influence the pulmonary immune homeostasis and physiology of the lungs through this vital, bidirectional cross-talk (Liu et al., 2020), and gut dysbiosis is associated with carcinogenesis, progression, and outcome of anticancer therapy of lung cancer through metabolism-related genotoxicity, defective immunosurveillance and systemic inflammation (Liu et al., 2021). Conversely, impaired lung function caused due to external triggers such as cigarette smoking, antibiotic treatment, and chronic lung diseases such as asthma, chronic respiratory infections (like drug-resistant *Staphylococcus aureus* pneumonia) and chronic obstructive pulmonary disease is associated with patient's susceptibility to developing inflammatory bowel disease (IBD) or irritable bowel syndrome (Keely et al., 2012; Rutten et al., 2014; Budden et al., 2016).

Although the mechanisms through which this cross-talk between the gut and the lungs influence the occurrence and progression of lung cancer are not completely known, the speculation is that the gut microbiome can promote systemic inflammation or cause immune and metabolic dysregulation, which can provide favourable environments for carcinogenesis and progression of cancer (Zhuang et al., 2019; Liu et al., 2020; Martins et al., 2021). Pulmonary inflammatory balance can also be influenced by gut microbiome-associated metabolites. For example, recent research has identified some metabolites, such as short-chain fatty acids (SCFA) (Rutting et al., 2019) and bile acid (Flynn et al., 2020), with potential influences on inflammatory processes. These observations suggest that the gut microbiome can be used both in diagnosis by identifying potential biomarkers of lung carcinogenesis (Zheng et al., 2020), and in the prevention and treatment of lung cancer through the alteration of microbiome composition (Liu et al., 2020).

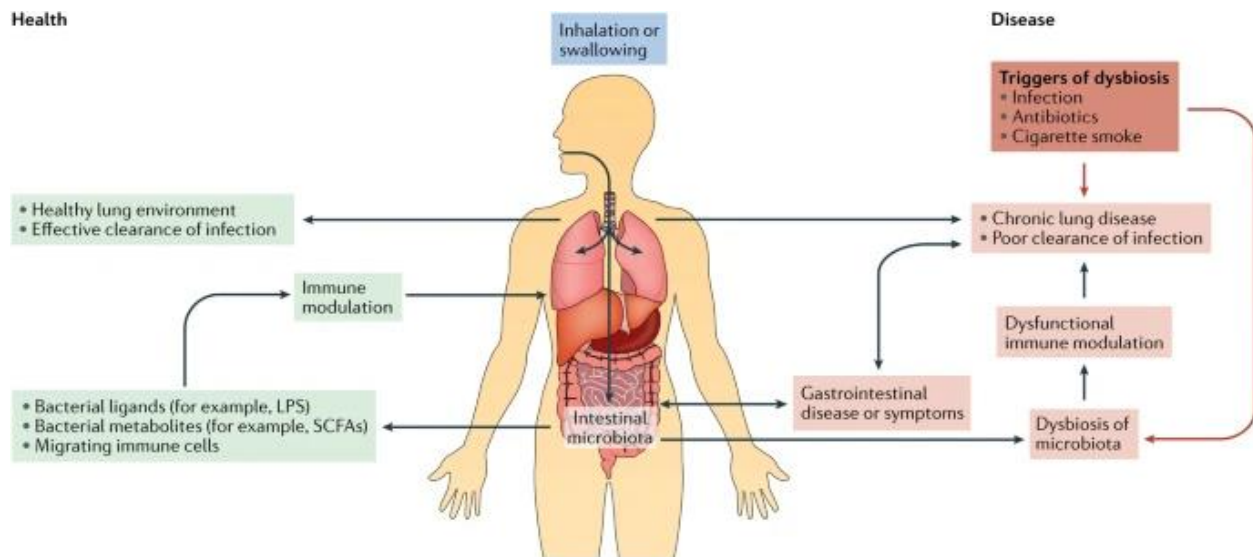


Figure 1: Schematic explaining the processes involved in the ‘Gut-Lung Axis’. A healthy gut microbiome can cause both local and systemic immune modulation through bacterial structural ligands (such as lipopolysaccharides and peptidoglycans) or secreted microbial metabolites (such as SCFA and bile acid). These immune modulations can cause better pulmonary outcomes such as infection clearance and healthy pulmonary immune homeostasis. However, gut microbiome dysbiosis can cause dysfunctional immune modulation, which leads to poor pulmonary outcomes. The triggers for the gut microbiome dysbiosis can originate from the gastrointestinal tract (like antibiotics and infections) or the respiratory tract like cigarette smoking or pulmonary diseases. (Figure taken from Budden *et al.*, 2016).

1.4. Gut-Lung Axis in the context of Radiation Therapy

The dysfunction of the gut-lung axis can be triggered by external stimuli such as infections and cigarette smoking (Budden *et al.*, 2016). Radiation therapy could also potentially trigger a dysfunction of this system as radiation-induced pulmonary tissue damage can cause acute and chronic local immune modulation that can develop to radiation-induced pulmonary pneumonitis and fibrosis. Studies show that gut microbiota composition changes in response to radiotherapy and its associated toxicity (Uribe-Herranz *et al.*, 2020). Radiation-induced damage from pelvic radiotherapy is shown to cause an increase in pro-inflammatory cytokines such as IL-1 β , IL-2, IL-6, and IL-8 (Indaram *et al.*, 2000) and cause dysbiosis of the gut microbiome (Gerassy-Vainberg *et al.*, 2017). So, it is hypothesised that radiation therapy can cause a disruption in the composition of the gut microbiome, which may alter an individual patient’s immune response to the tumour, thereby affecting tumour growth and the efficacy of cancer therapy; additionally, the alteration in the gut microbiome caused due to the radiotherapy can affect the systemic immune system activity, thus promoting

acute and chronic inflammation leading to the pathogenesis of radiation pneumonitis and fibrosis, and affecting patient's susceptibility to GI and pulmonary infections.

To test out the hypothesis, the experimental project examining the cross-talk between host's gastrointestinal and pulmonary processes in response to radiation-induced lung toxicity is currently being carried out jointly by Prof Dr Verena Jendrossek (Molecular Cell Biology at the Institute of Cell Biology - Tumour Research at the University Hospital Essen) and Prof Dr Astrid Westendorf (Infection Immunology at the Institute for Medical Microbiology at the University Hospital Essen) under the framework of Deutsche Forschungsgemeinschaft (DFG) funded GRK2762 project. They use established C57BL/6 mouse models to determine dynamic changes in the immune responses in gut and lungs along with the changes in the composition and diversity of the host microbiota after thoracic radiation. Their collected data includes fresh faecal pellets, lung tissue, and bronchoalveolar lavage fluid (BALF) before t_0 and t_1 , t_4 , t_{10} , t_{21} , t_{84} , and t_{168} days after treatment, the level of bacterial metabolites (e.g., short-chain fatty acids) over time and immune cell phenotyping (innate and adaptive immune cell repertoire and subtypes, cytokine/chemokine profile) of the mice.

1.5. Computational Modelling to Understand the Gut-Lung Axis

Despite all the cavities in our understanding of the bidirectional communication between the gut microbiome and the lung immune processes (Liu *et al.*, 2020; Schluter *et al.*, 2020), the accumulated knowledge of the previous studies on gut-lung interactions gives us an interesting picture with a reasonable resolution of the major routes of communications over the gut-lung axis (Liu *et al.*, 2021). For example, several local and systemic mechanisms have already been identified to play a role in the regulatory function of the gastrointestinal microbiome on lung inflammation and immunity (Gallacher and Kotecha, 2016). However, the complexity of the interconnected network of the numerous players in this phenomenon makes hypothesis testing very challenging. Finding reliable biomarkers for diagnosis or promising targets for therapy requires extensive studies in all different conditions of human patients, an objective that cannot be easily achieved merely by experimental studies due to several restrictions. This challenge is particularly pronounced in human studies because of practical and ethical concerns associated with human experimentation (De Jong and Maina, 2010).

Recently, mathematical and computational models have been utilised to address this challenge, providing researchers with novel tools to study and understand immuno-oncology-related problems. They do so by dissecting their complexity and quantitatively testing biological hypotheses under fully controlled conditions with negligible cost regarding time, resources, and animal lives (Metzcar *et al.*, 2019). These models enable researchers to examine the relationships between complex regulatory processes and how disruptions of these biological processes may contribute to the pathophysiology of the disease. Mechanistic mathematical models can serve as *in silico* virtual experiments that give us the ability to understand the dynamics of both the innate and adaptive immune responses at different biological scales ranging from molecular to tissue levels (Eftimie *et al.*, 2016). These models also enable us to simulate and study heterogeneous multi-scale mechanisms that are involved in cancer development and progression (Valentinuzzi and Jeraj, 2020). So, computational models can help bridge the present gap and provide mechanistic insights into the 'gut-lung axis', which can then be experimentally challenged and verified.

Using continuous compartmental models based on ordinary differential equations to model tumour-immune system dynamics have a long history (ed. JA Adam, and N Bellomo, 1997). Over the years, several modelling approaches are developed for understanding immuno-oncology related systems, such as pharmacodynamic /pharmacokinetic (PD/PK) models, evolutionary game theory models, agent-based models, spatial-temporal models, and boolean (logic-based) models (Sancho-Araiz *et al.*, 2021). Recently, Quantitative Systems Pharmacology (QSP) models have become an essential component in modelling for immuno-oncology applications such as treatment and drug development (Leil and Ermakov, 2015; Sové *et al.*, 2020). These models allow the construction and simulation of large-scale compartmental models of the human immune response (Rogers *et al.*, 2021a) and understand the pharmacokinetic and pharmacodynamic perspectives of different drug treatment strategies (Rogers *et al.*, 2021b). For example, QSP models have been used to study hemodynamics by modelling cardiovascular and renal function (Helmlinger *et al.*, 2019a), to simulate neoadjuvant PD-1 inhibition in non-small cell lung cancer (Jafarnejad *et al.*, 2019), and to predict clinical responses to novel combined immunotherapy in breast cancer (Wang *et al.*, 2019).

1.6. Introduction to Quantitative Systems Pharmacology (QSP) Modelling

Quantitative systems pharmacology (QSP) modelling is a modelling approach which initially emerged in pharmaceutical industries as a response to the need for more quantitative approaches to drug discovery and development and to study the relationship between a drug of interest, its potential target, and its interaction with the biological system (Visser *et al.*, 2014). This style of modelling integrates ideas from a wide range of disciplines, including pharmacology, systems biology, mathematics, biochemistry, and computer science, with the goal of developing quantitative models that can help to understand and predict the behaviour of complex biological systems (Leil and Ermakov, 2015). Though initially used to address questions in the fields of pharmacology and drug development, QSP modelling approaches are increasingly being used in basic and translational research, for example in the study of nutritional and metabolic diseases such as type-2 diabetes mellitus, neurological diseases such as Alzheimer's disease, immuno-oncology and immunotherapy (Aghamiri *et al.*, 2021).

QSP models can integrate and incorporate data from various sources, such as pharmacokinetic, pharmacodynamic, and disease physiology data, to create a comprehensive mechanistic and quantitative understanding of the various interactions in the biological system. This, along with increased computational capacity and better modelling and parallelisation methodologies, allows us to get a more accurate and realistic representation of the biological system, which can lead to better predictions and hypothesis testing (Sorger *et al.*, 2011). QSP models also have the feasibility to use experimental/clinical cohort sample data to generate virtual populations which reproduce the population statistics and represent the biological heterogeneity found in real-world populations (Allen *et al.*, 2016). Virtual populations can be a powerful tool for generating and testing new hypotheses as they allow one to test them *in silico* in a large and diverse population without the need for extensive and expensive experimental studies. This allows the researchers to directly validate the results in experimental settings and/or clinical trials with a complementary approach, thus saving time and resources in the process (Visser *et al.*, 2014). Additionally, QSP models have the flexibility to be constructed modularly, which allows for the easy incorporation of new mechanisms and new modules/compartments and modification of the existing interactions in the model (Knight-Schrijver *et al.*, 2016).

However, these models are not without their limitations. One of their main constraints is the complexity of the model and underlying assumptions made, which can lead to issues in parameter identifiability and overparameterisation of the model (Stein and Looby, 2018; Sher *et al.*, 2022). QSP models also face validation challenges requiring large datasets to validate the model, which may not be available at the time of validation or can be inaccessible at certain biological scales (Aghamiri *et al.*, 2021). These models often tend to have a limited scope of applicability to a particular disease or drug setting, which can limit the model's applicability to other biological systems or disease conditions (Peterson and Riggs, 2015). Moreover, given their recent emergence, there is no standardisation for the file format, which makes inter-compatibility between computational platforms difficult, limiting its transparency, transferability and reusability within the modelling community (Ermakov *et al.*, 2019). Therefore, QSP models require careful consideration and validation to ensure their applicability, accuracy, and reliability to the biological system in question.

The typical process of developing a QSP model involves three main steps (Leil and Bertz, 2014):

- (i) **Model Scope** which involves defining the objectives and mechanistic pathways representing all biological and pharmacological processes involved
- (ii) **Model Development** which includes mathematical descriptions of the biological pathways, standardisation of input data, parameter estimation and simulation analysis
- (iii) **Model Qualification** which includes integrating data from target populations to generate virtual populations and utilising them to generate new hypotheses based on end goals (for example, drug development from pharmacological perspective)

Figure 2 explains the general workflow in the development of QSP models. The core elements in this workflow are as follows: formulating the biological problem that is being addressed, translating the biological knowledge and experimental data into a set of mathematical equations that describe the behaviour of the system, parameter estimation to calibrate the developed model, simulating the model under different conditions in order to represent the healthy and the diseased state and validating the model by comparing its predictions from the simulations to experimental data that was not used in the parameter estimation process (Leil and Bertz, 2014; Helmlinger *et al.*,

2019b; Niarakis and Helikar, 2021). Once a model is validated, one can explore the impact of known variability and uncertainty of the estimated parameters of the model to generate “ensembles of parameterisations,” otherwise called virtual populations (Allen *et al.*, 2016). This is a usually a very time-consuming process to finally get the validated model which is useful, interpretable, and informative to testing biological hypotheses, suggesting targets or biomarkers and ultimately generating a model with translational value.

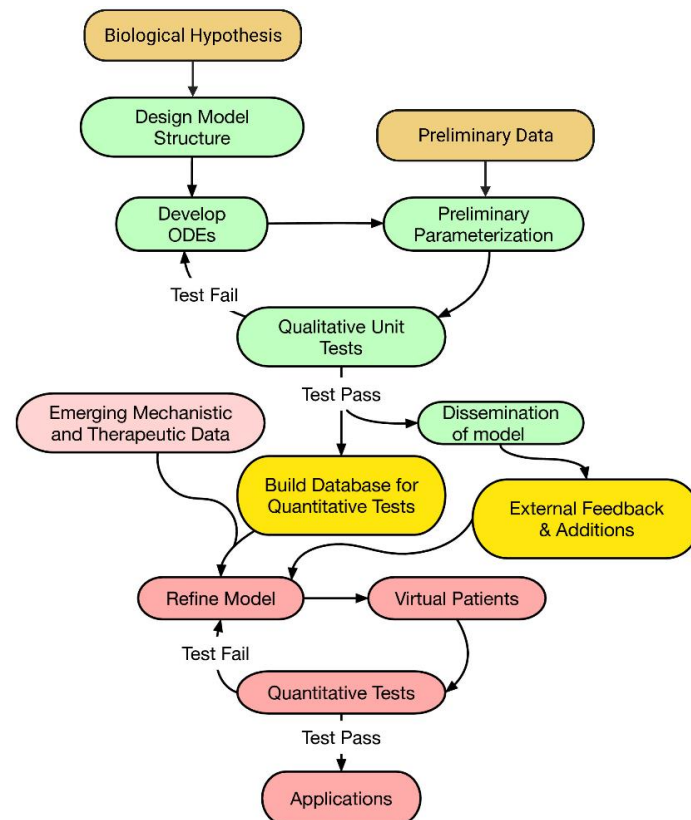


Figure 2: Steps involved in the QSP modelling. The development of the QSP model involves model formulation, parameterisation, model validation and virtual population generation, after which the model is used for its intended applications (Figure adapted from Dai *et al.*, 2021).

1.7. Quantitative Systems Pharmacology (QSP) model of the Gut-Lung Axis

Modelling microbiome-associated immune response in the gut-lung axis is highly complex because this phenomenon involves the interplay among various cell types including innate and adaptive immune cells, as well as endotoxins, cytokines, and microbial metabolites that are released into the systemic circulation. The complexity of immune interactions along the gut-lung axis makes the development of a

computational model of the 'gut-lung axis' system challenging. Additionally, issues such as variability observed in experimental measurements, the diversity and errors associated with analytical techniques used to generate those measurements, quantitatively integrating the measurements into the model and accounting for the heterogeneity in the response of the biological population, and most importantly, our limited understanding of the interactions between different immune system components in the gut-lung axis make modelling this system even more challenging.

QSP modelling is a potential approach that can be used to quantitatively and dynamically understand this system to study the complex interactions between the gut microbiome, the immune system, and the respiratory epithelium. By incorporating the existing mechanistic knowledge of immune interactions along the gut-lung axis and integrating with measurements from multiple types of data such as flow-cytometry, ELISA, RNA sequencing and faecal metabolomics datasets, one can use QSP models to elucidate the underlying immunological mechanisms that contribute to the bidirectional communication channel between the GI tract and the lungs. The experimental data generated from the GRK2762 project can be used for the parameterisation and validation of the QSP model of the gut-lung axis. The validated model can be used to generate and test new hypotheses, identify new biomarkers, study the effects of various interventions, including radiation therapy, and predict the response of an individual to such interventions.

1.8. Hypothesis

The hypothesis of the project is that a computational model, upon validation, can reliably be used to accurately simulate the immune dynamics along the gut-lung axis and quantitatively test biological hypotheses. The model will enable studying the system from two perspectives: how cancer therapy impacts the gut microbiota composition and how changes in the microbiome can affect tumour growth and the effectiveness of the cancer treatments. The model can help to understand how perturbations in the system from the healthy state (such as radiation therapy in lungs and sustained chronic inflammation in gut) can disrupt the local and systemic immune homeostasis, which in turn can affect the efficacy of the cancer therapy including radiotherapy, and the patient's susceptibility to developing complications from the treatments such as radiation pneumonitis, pulmonary fibrosis and bacterial infections.

1.9. Aim

The aim of this project is to create a computational QSP model that incorporates detailed mechanisms of both innate and adaptive immunological interactions along the 'gut-lung axis' to investigate the above-mentioned hypothesis.

1.10. Objectives

The main objective of the project for the Master's thesis is to develop a general QSP model of immune interactions along the 'gut-lung axis.' The initial focus to concentrate on the immune interactions and exclude the gut microbial interactions and bacterial metabolites dynamics is decided based on the time and scope of the project. The sub-objectives include:

- 1) To develop and validate the gut compartment
 - a) To develop a model of immune interactions between major lymphoid and myeloid immune cells and their associated cytokines in the gut compartment
 - b) To validate the model with experimental data
 - c) To explore the model's applicability in the context of Inflammatory Bowel Disease (IBD)
- 2) To develop and validate the lung compartment
 - a) To develop a model of immune interactions between major lymphoid and myeloid immune cells and their associated cytokines in the lung compartment
 - b) To include the radiation dynamics of epithelial cells and damage-associated immune mechanisms in the model
 - c) To validate the model with experimental data
 - d) To explore the model's applicability in the context of radiation pneumonitis
- 3) To develop and validate the 'gut-lung axis' (GLA) model
 - a) To combine the individual compartments to establish the final GLA model
 - b) To revalidate the model with experimental data

2. Methods and Materials

This chapter is divided into two sections: computational and experimental methods used in the project with their respective descriptions in each section.

2.1. Computational Methods

2.1.1. Model Formulation

The QSP model for this project was based upon significant adaptations of prior models of inflammatory bowel disease (Rogers *et al.*, 2021a) for the gut compartment and SARS-CoV-2 for the lung compartment (Dai *et al.*, 2021). The overall simplified representation of the ‘gut-lung axis’ model showing the major compartments and interactions between them is shown in

Figure 3. The final gut-lung axis (GLA) model was built using MATLAB R2022a (MathWorks) and consists of 3 compartments, 76 state variables (species) and 533 parameters. The model structure includes the gut compartment, the lung compartment and the systemic circulation compartment (also referred to as blood compartment). It is to be noted that a single biological entity can be counted up to three different species in the model to differentiate its presence in each compartment. For example, cytokine interleukin 6 (IL-6) is considered to be three species in the model: Gut_IL6, Blood_IL6 and Lung_IL6. The exhaustive list of all the state variables, the parameters and their description are provided in Table 7 & Table 8 in Appendix 1.



Figure 3: The simplified diagram of the QSP model of the ‘gut-lung axis.’ The final model consists of three compartments: Gut, Lung, and Blood (also referred as systemic circulation in later sections, used interchangeably) and their interactions between the compartments. The model also includes species such as immune cells and cytokines in each compartment.

The QSP model, which is deterministic in nature, is structured as a system of ordinary differential equations (ODEs) which is of the form as shown below:

$$\frac{dx_i}{dt} = \sum_j R_{ij}(\vec{x}) \cdot x_j$$

Here in the equation, for the state variable x_i , its differentiation with respect to time t is the summation of the rates contributed by all state variables in the model to state variable x_i . \vec{x} denotes the vector of the model state variables and R_{ij} denotes the velocity fluxes (or rates) contributed by x_j to the state variable x_i . R_{ij} is a function of the vector \vec{x} and indicates the overall mechanistic structure of the model.

The final GLA model is composed of several individual but interconnected species such as lymphoid cells (T cells including helper T cells and cytotoxic T cells), myeloid cells (macrophages, dendritic cells, and neutrophils), and cytokines (such as interleukins and growth factors). The ODE equations that model the interaction between immune cells and cytokines were mainly adapted from the IBD model (Rogers *et al.*, 2021a), which includes relevant cellular pathways, including replication, differentiation, migration, and apoptosis of various immune cell types and production, transportation, and degradation of cytokines.

As an example, the following ODE equation describes the dynamics of transforming growth factor beta (TGF- β) in the gut compartment:

$$\frac{d(\text{Gut_TGF}\beta)}{dt} = r_{\text{prod}} + r_{\text{bloodtogut}} - r_{\text{guttoblood}} - r_{\text{deg}}$$

where,

- r_{prod} = rate of production/secretion
- $r_{\text{bloodtogut}}$ = rate of transportation from Blood compartment to Gut compartment
- $r_{\text{guttoblood}}$ = rate of transportation from Gut compartment to Blood compartment
- r_{deg} = rate of degradation

These terms further expand as follows:

$$\begin{aligned} r_{\text{prod}} &= k_{\text{basal_prod}} + k_{\text{Th17}} * (\text{Gut_Th17}) + k_{\text{Treg}} * (\text{Gut_Treg}) + k_{\text{M2}} * (\text{Gut_M2}) \\ r_{\text{bloodtogut}} &= k_{\text{bloodtogut}} * (\text{Blood_TGFb}) \\ r_{\text{guttoblood}} &= k_{\text{guttoblood}} * (\text{Gut_TGFb}) \\ r_{\text{deg}} &= k_{\text{deg}} * (\text{Gut_TGFb}) \end{aligned}$$

k_y refers to the rate of the reaction with respect to the species y

The dynamics of TGF- β in the gut compartment are determined by the four fluxes: production rate of TGF- β by immune cells, transportation rates between the gut and blood compartments and the degradation rate of TGF- β . In the model, we assume that the TGF- β is produced at a basal rate and immune cells, T helper 17 cells (Th17), Regulatory T cells (Treg), and alternatively activated macrophages (M2) contribute to the production rate of TGF- β in the gut compartment of the model. TGF- β can also enter into the gut from the blood compartment and vice versa. Additionally, the model considers that TGF- β gets degraded in the gut compartment at a linear rate.

The immune dynamics in both gut and lung compartments can be broadly classified into two categories: pro- and anti-inflammatory immune interactions, which keep each other in balance in the healthy state of the model. The detailed explanations of these immune interactions are described in the gut compartment of the ‘Results’ chapter.

The lung compartment also includes the dynamics of radiation-induced damage, which were added to the GLA model to understand the impact of radiation on pulmonary immune and systemic immune homeostasis. The model considers the dynamics of pulmonary alveolar epithelial cells and the corresponding radiation and cytokine-associated damage responses. The details of the mechanisms are discussed in the lung compartment of the ‘Results’ chapter.

Additionally, we also included the production, transportation, and degradation of C-reactive protein (CRP) and Surfactant protein D (SPD) in the final model as two endpoint biomarkers. CRP is a marker of the systemic inflammation state of the host (Capelozzi et al., 2017), and in the model, we consider that IL-6 induces the production of CRP in the liver and gets released into the systemic circulation from the liver. SPD is an indicator of alveolar cell damage and a useful marker of radiation-induced lung injury (Śliwińska-Mossoń *et al.*, 2020), and it is produced when damaged cells get cleared in the model.

2.1.2. Model Evaluation

Once each compartment was finalised, the steady-state results obtained from the simulation of the model were compared with the experimental data in different disease settings. For the gut compartment, the comparison was made in the context of inflammatory bowel disease (IBD) with in-house data from the collaborators as well as data used by the authors (Rogers *et al.*, 2021a). For the lung compartment, this comparison was made in the context of radiation pneumonitis with data generated by experimental collaborators. Since the model parameters have not been parameterised for mice data, this comparison was a qualitative comparison between experimental mice data and simulation results.

2.1.3. Parameter Sensitivity Analysis

We performed a local sensitivity analysis of the steady-state results on the parameters of the gut and lung compartments of the model. Sensitivity analysis is a type of analysis that determines how the target state variables are affected by changes in the parameters and other input variables in the model (Hoops *et al.*, 2016). It is an assessment of the sensitivity of a mathematical model to its modelling assumptions, and it is routinely performed to understand the impact of a parameter on the variable of interest in complex computational models. The sensitivity coefficient for each parameter for a particular state variable is calculated by the following equation:

$$SC_p = \text{mean}_{\text{sim}} \left(\frac{\partial y}{\partial p} \cdot \frac{p_n}{y_n} \right) = \text{mean}_{\text{sim}} \left(\frac{p_n}{y_n} \cdot \frac{\partial y}{\partial p} \right)$$

Here, in the equation, SC_p denotes the sensitivity coefficient of parameter p , mean_{sim} denotes the mean of all perturbed simulations and p_n and y_n denote the value of parameter p and steady-state value of state variable y at nominal (unperturbed) simulation respectively. The parameter p is perturbed by a small ∂p and the resultant change in the steady-state value of the state variable y is used to calculate the sensitivity coefficient of that parameter with respect to the state variable (IntiQuan GmbH, 2022). The mathematical principles behind performing sensitivity analysis to explore uncertainty in parameters are described in Saltelli *et al.*, 2007. The sensitivity analysis was performed using IQR Tools package version 99.0.0 in R (Version 4.1.3).

2.2. Experimental Methods

This section discusses the experimental methods used during the training internship at Dr Jendrossek's lab to generate flow cytometric measurements of the immune cell populations in control mice.

2.2.1. Mice

Wild-type C57BL/6J0laHsd mice used for the experiments were bred and housed under specific pathogen-free conditions in the animal facility laboratory of the Institute of Cell Biology (Tumour Research) at the University Hospital Essen. The mice were humanely euthanised using carbon dioxide (CO₂), and efforts were made to minimise suffering. All procedures involving mice were approved by the local animal welfare committee (State Agency for Nature, Environment and Consumer Protection (LANUV), Regierungspräsidium Düsseldorf, North Rhine-Westphalia, Germany) and were performed in accordance with the guidelines mandated by the University Hospital Essen, and the recommendations of the Gesellschaft für Versuchstierkunde (GV-SOLAS) and Federation of European Laboratory Animal Science Association (FELASA).

2.2.2. Isolation of Blood and Serum

An incision was made in the mice using a scalpel in the linea alba from the pelvis to the rib cage. The vena cava caudalis was exposed and punctured with a needle (Dispomed) attached to a 1 ml Tuberculin syringe (Becton Dickinson) at the branching point of the vein with the open side of the needle facing up. The blood was gently taken without collapsing the vein and transferred into an EDTA collection tube (Sarstedt). The tubes were centrifuged for 5 min at 3000 rpm and supernatant (serum) was collected. The cell pellet was transferred to 15 ml Falcon containing 2 ml Ammonium-Chloride-Potassium (ACK) (Table 1) buffer and kept on ice for approximately 1 min to perform erythrocyte lysis until the colour disappeared, upon which 8 ml of Dulbecco's Modified Eagle Medium (DMEM) (Invitrogen, 41966029) was added. The blood cells were centrifuged for 5 min at 1500 rpm and kept at 4°C, and the supernatant was discarded. The cell pellet was carefully resuspended in DMEM medium.

Components	Amount
Ammonium chloride (Merck)	8.29 g
Potassium bicarbonate (Roth)	1.00 g
0.5 M EDTA (Invitrogen)	200 μ L

Table 1: Composition of ACK Buffer (for 1 L, pH 7.2 - 7.4)

2.2.3. Isolation of Lung Cells

The peritoneum was opened and the thoracic cavity was accessed by removing the diaphragm. Using a 10 ml syringe, 4 ml phosphate buffer saline (PBS) solution (Thermofisher Scientific) was injected into the right ventricle of the heart until the lungs turn white in colour. Lungs were isolated from the mice by using scalpels and the lung lobes were rigorously minced. The tissue suspension was transferred to 50 ml Falcon tubes containing 5 ml of 1% Collagenase D (Roche Life Science, 11088866001) in PBS solution. The cell suspension was incubated in a water bath at 37°C for 40 min, vertexing every 15 min. After the collagenase digestion, 20 μ l of 0.5M ethylenediaminetetraacetic acid (EDTA) (Invitrogen, 8043.2) was added and the Falcon tubes were incubated in the water bath for 5 minutes. After incubation, the lung cell suspension was transferred and sequentially filtered through a 70 μ m cell strainer (VWR) and 30 μ m cell strainer (Sysmex) placed on top of another Falcon tube and flushed with PBS. The cells were centrifuged for 5 min at 1500 rpm kept at 4°C, and the supernatant was discharged. The cells were resuspended in 1 ml ACK buffer and kept on ice for 1 min. To stop further lysis, 14 ml of Dulbecco's Modified Eagle Medium (DMEM) (Invitrogen, 41966029) was added. The cells were centrifuged for 5 min at 1500 rpm kept at 4°C, and the supernatant was discarded. The cells were resuspended using 5 ml DMEM and kept on ice for flow cytometric (FACS) staining.

2.2.4. Isolation of Spleen Cells

Spleen was harvested from the peritoneum of the mice. The spleen placed upon a 70 μ m cell strainer underneath a petri dish (Greiner Bio-One) and slowly injected with 2ml of ACK buffer into the spleen. The spleen was then passed through the 70 μ m cell strainer and 3 ml of DMEM medium was used to wash the spleen on the cell strainer. The cells were then pipetted from the petri dish and filtered through a 30 μ m cell strainer placed on top of 15 ml Falcon tube. The cells were centrifuged for 5 min at 1500 rpm kept at 4°C, and the supernatant was discarded. The cell pellet was carefully resuspended using 5 ml DMEM medium.

2.2.5. Isolation of Cells from Lymph Nodes

The superficial cervical lymph nodes were isolated from mice and transferred to a petri dish containing 4 ml DMEM. The lymph nodes were lacerated apart using tweezers and the cells released can be observed as white cloud around lymph nodes. The remaining tissue was discarded and the medium was transferred to a 15 ml Falcon tube. The cells were centrifuged for 5 min at 1500 rpm kept at 4°C, and the pellet was resuspended in 5 ml DMEM.

2.2.6. Flow Cytometric Staining

The cell suspensions from blood, lungs, spleen, and lymph nodes were added to 96-well plate with each well containing 50-100 µl of the cell suspension to have approximately 10^6 cells per well. The plate was centrifuged for 5 mins at 1500 rpm at 4°C and the supernatant was discarded. The plate was vortexed to break the pellet and 100 µl of the antibody mixture cocktail (Table 5) and fixable viability dye, eFluor780 (APC-Cy7) (ThermoFisher Scientific, 65-0865-18) was added per well. The 96-well plate was incubated in dark for 10 minutes at 4°C. After the incubation, 100 µl FACS Buffer (Table 2) was added per well and centrifuged for 5 min at 1500 rpm.

For surface staining, after this step, 100 µl of 1% paraformaldehyde (Roth, 0335.2) in FACS buffer was added to fix the cells. For intracellular staining, the wells were washed with PBS and 100 µl Fix-Perm-Solution (Table 3) was added per well and incubated in dark for 1.5 hours at 4°C or 40 min in room temperature for the permeabilisation of the cell membrane. The cells were washed with 100 µl Perm-Buffer (Table 4) and centrifuged for 5 mins at 1500 rpm. The supernatant was discarded and the cell plate was vortexed. The intracellular antibody mixture was added to the well and incubated in dark for 30 mins at 4°C. The wells were washed with 100 µl Perm-Buffer and the supernatant was discarded after centrifugation. The cell pellet was resuspended in 100 µl of FACS buffer.

Components	Amount
PBS	50 ml
Fetal Bovine Serum (FBS) (Sigma Aldrich)	250 µL
0.5 M EDTA	200 µL

Table 2: Composition of FACS Buffer (for 50 ml)

Components	Dilution Ratio
Cytofix/Cytoperm (Becton Dickinson)	1
BD Perm/Wash (Becton Dickinson)	4

Table 3: Composition of Fix-Perm-Solution

Components	Dilution Ratio
BD Perm/Wash	1
dH ₂ O	10

Table 4: Composition of Perm-Buffer

Antibody Name	Dilution	Animal Host	Catalog No.	Source
PerCP/Cy5.5anti-mouse CD11b	1:400	Rat IgG2b,k	101227	BioLegend
APC anti-mouse CD11c	1:400	Armenian Hamster IgG	117309	BioLegend
APC Anti-mouse MHC Class II (8I-A/I-E)	1:1000	Rat IgG2b,k	17-5321	eBioscience
Pacific blue anti-mouse CD45	1:333	Rat IgG2b,k	103126	BioLegend
APC anti-mouse CD3	1:100	Armenian Hamster IgG	100312	BioLegend
PE-Cy7 anti-mouse F4/80	1:200	Rat IgG2a,k	123113	BioLegend
PE anti-mouse/human CD45R/B220	1:800	Rat IgG2a,k	103208	BioLegend
FITC anti-mouse CD8a	1:200	Rat IgG2a,k	11-0081	eBioscience
PE/Cy7 anti-mouse CD25	1:100	Rat IgG1	102016	BioLegend
Pacific Blue Rat anti-Mouse CD4	1:800	Rat (DA) IgG2a,k	558107	BD
BV510 Rat Anti-Mouse CD335 (NKp46)		Rat IgG2a,k	563455	BD
APC anti mouse Ly-6G	1:1000	Rat IgG2a, κ	127614	BioLegend
Brilliant Violet 605 anti-mouse Ly6C		Rat IgG2c,k	128035	BioLegend
Brilliant Violent 650 anti-mouse CD45		Rat IgG2b,k	103151	BioLegend
PE anti-mouse CD86	1:600	Rat IgG2a,k	105008	BioLegend

Table 5: List of antibodies used for flow cytometric straining

Different myeloid cells and lymphocytes and their subtypes bind to different cell surface markers. When using a multi-colour flow cytometer, it is important that the peaks of emission spectrum of the fluorophores minimally overlap with each other so that the detected signals are discriminable with a proper compensation. By analysing their in-silico excitation and emission spectrum using BD Fluorescence Spectrum Analyzer webtool (Spectral Viewer, 2023) to ensure minimal overlap, the antibodies for the cell surface markers corresponding to the immune subtypes of interest were

selected. Figure 4 shows the in-silico analysis done using the BD Spectrum Analyser webtool for the flow cytometric staining for lymphocytes. Additionally, in the staining panel, the antibodies' specificity during the experiments was controlled using isotype controls, which are used to examine for levels of unspecific binding between the antibodies and cells in the sample of interest. The gating strategy for the different immune cell populations is discussed in the 'Results' section.

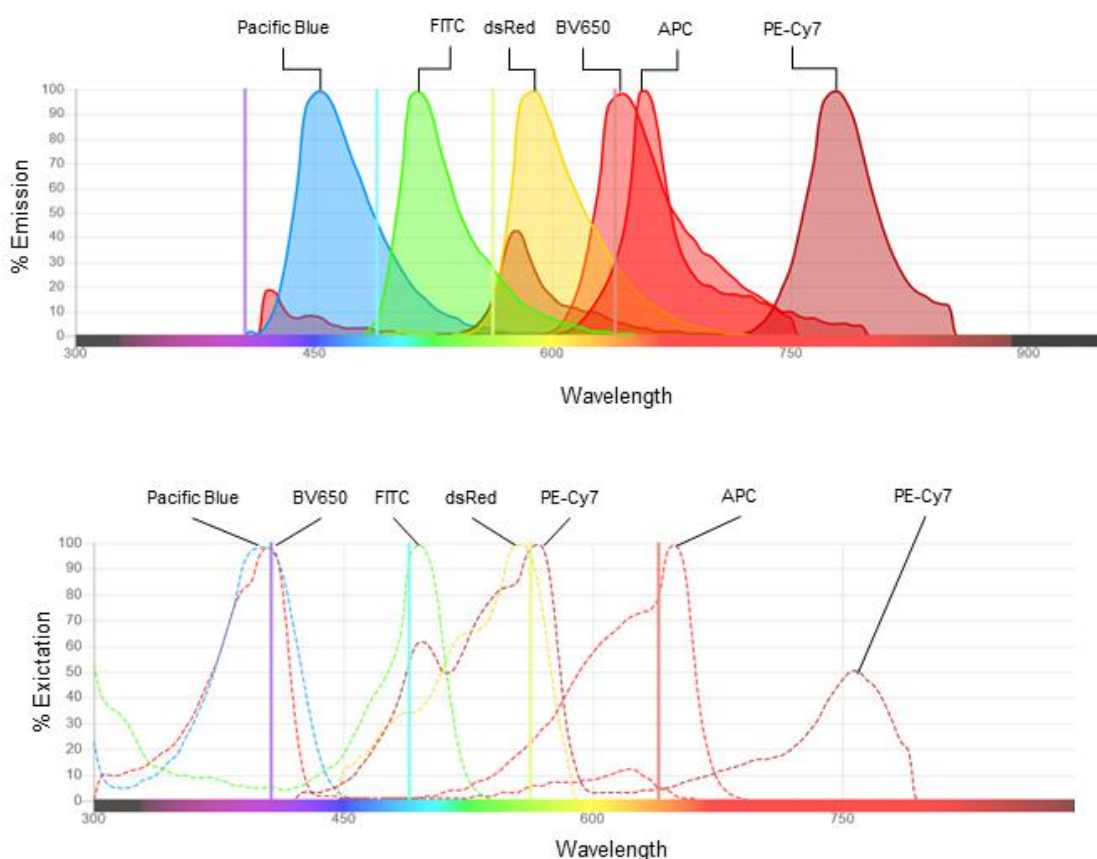


Figure 4: Emission and Excitation spectrums of fluorophores used in lymphocytes staining. The fluorophores of antibodies used for the lymphocytes staining are chosen based on ensuring minimal overlap of peaks of emission spectrum of those fluorescent probes. The violet, cyan, yellow and red solid lines in the plots indicates the four lasers (405 nm, 488 nm, 561 nm and 638 nm laser respectively) used to excite the fluorophores. It is to be noted that BV650 and APC signals can be distinguished with proper compensation. Plot generated from the Beckman Coulter in-built webtool, Spectral Viewer, 2023.

After the staining, the cells were analysed with BD CytoFLEX Flow Cytometer (Beckman Coulter, S V4-B2-Y4-R3). The data was evaluated using CytExpert Acquisition and Analysis Software Version 2.3 (Beckman Coulter) and visualised using Prism 7.0c (GraphPad Software).

3. Results

This chapter is divided into three sections: Gut Model, Lung Model and Gut-Lung Axis Model. This is done to emphasise the flow of the modular build of each compartment during the course of the thesis and the results associated with each compartment. The first two sections focus on the immune interactions in detail within each of their respective compartments and their application in different disease settings. The final section discusses the processes involved in the amalgamation of the compartments, and the overall picture of the model and its associated implications.

3.1. Gut Compartment

3.1.1. Formulation of Gut model

The QSP model of the gut compartment is adapted from the inflammatory bowel disease (IBD) model (Rogers *et al.*, 2021a). The authors developed a comprehensive IBD model with an extensive network of immune interactions between CD4+ helper T cells and their subpopulations (Th1, Th2, Th17 and Treg), M1 and M2 macrophages, effector and tolerogenic dendritic cells (DCs), natural killer (NK) cells, neutrophils and their associated cytokines. This model was built using the SimBiology toolbox in MATLAB, which was incompatible with our platform. So, the ODE equations were recoded to be compatible with the base packages in MATLAB.

The gut model developed has two compartments: Gut and Blood compartments. The model has 46 species and 336 parameters describing the interactions between the adaptive and innate immune cell populations and cytokines, as well as the dynamics of the CRP (Figure 5). The model parameters were directly taken from the IBD model as the authors estimated and validated them using data from human clinical trials (Rogers *et al.*, 2021a). The model also has the flexibility to simulate the model in the diseased mode, i.e., the two subtypes of inflammatory bowel disease: Crohn's disease (CD) and ulcerative colitis (UC). The difference between healthy mode (referred to as healthy volunteers (HV) in the model) and the two diseased mode (CD and UC) is the basal production rates of certain immune cells and cytokines in the system (see Table 9 in Appendix 2). The remaining parameters barring these 24 basal production rates remain constant between the HV, CD and UC modes.

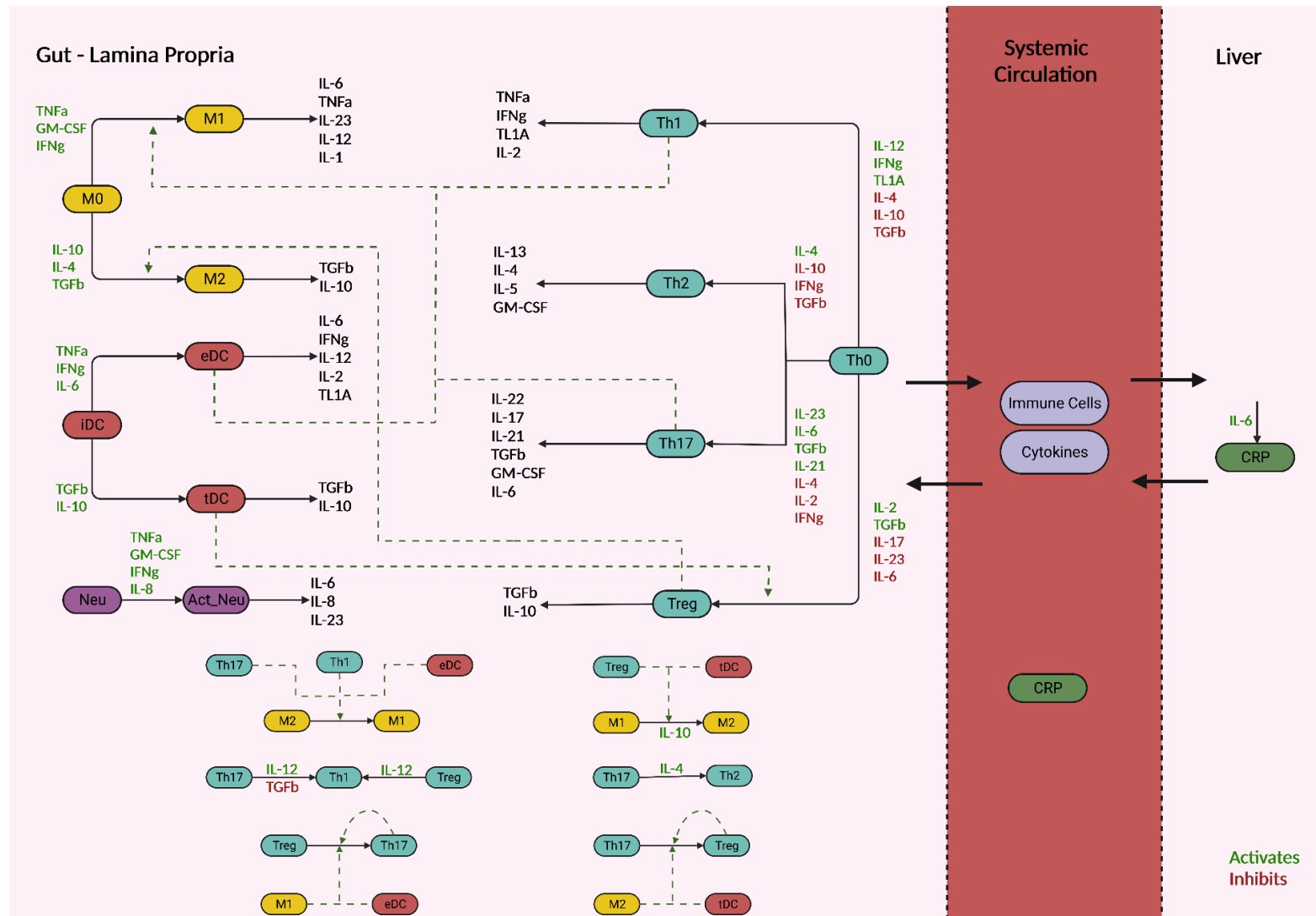


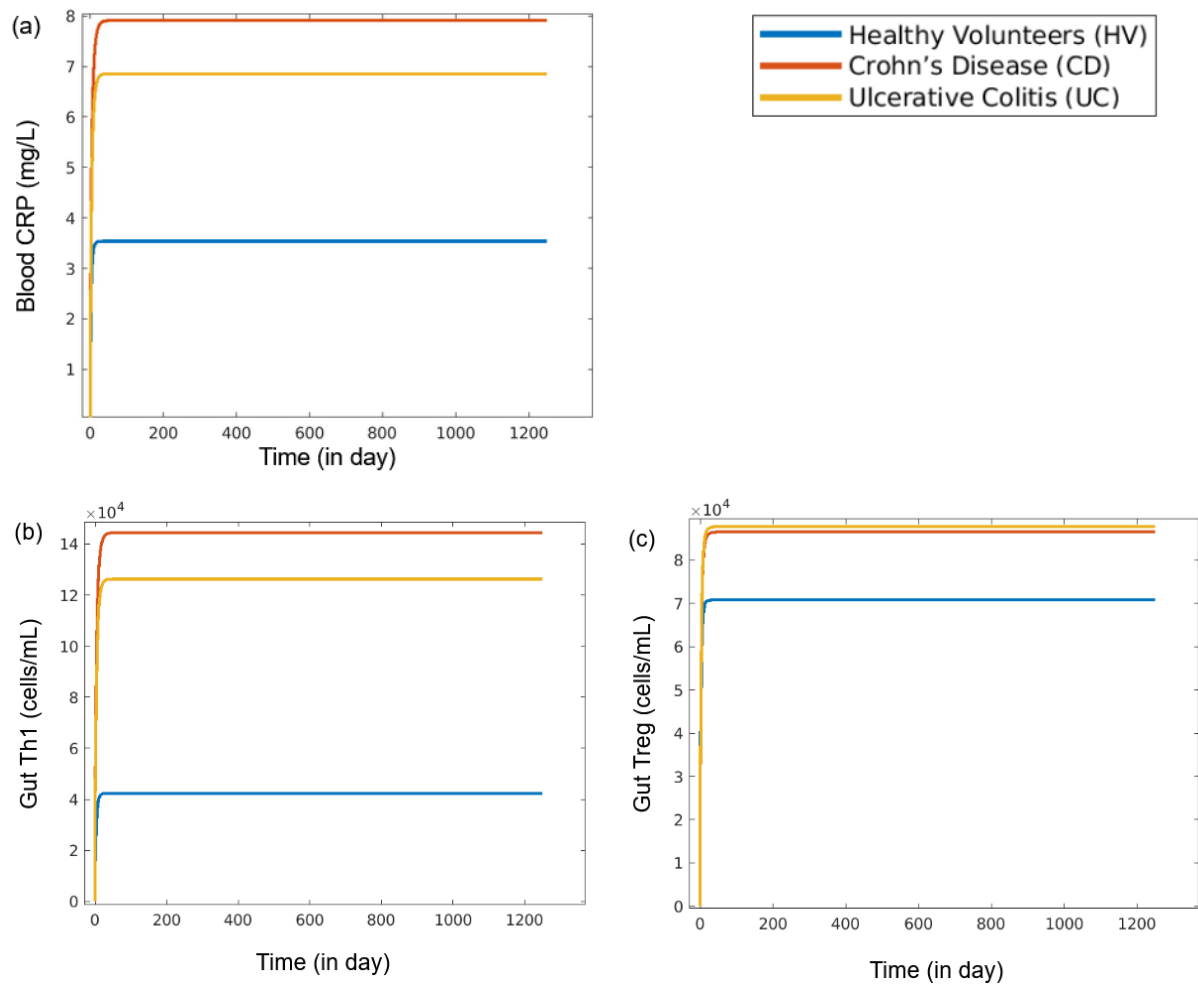
Figure 5: Overview of the mechanistic structure of the Gut compartment. The gut compartment has the major lymphoid and myeloid immune cell, and cytokine interactions. The immune processes in the gut happen in the lamina propria and there is a migration of immune cells and cytokines between the gut and blood. Hepatic CRP production and its systemic circulation serves as an indicator of inflammation. The solid black arrows indicate the reaction such as production, differentiation or transportation of species, whereas the dotted lines indicate that the species has a positive (green) or negative (red) influence on the reaction. Cytokines in green and red indicates that it has a positive or negative impact on the reaction respectively. Figure created with BioRender.com

The gut model includes the major immune interaction networks, which are based on existing literature knowledge. Immune cells produce distinct cytokines particular to them, and the cytokines present in the system determine the cell differentiation rates (Fig. 4). Naïve helper T cells (Th0) get recruited into the gut and get differentiated into Th1, Th2, Th17 and regulatory T cells (Treg) based on the cytokine profile which can preferentially activate or inhibit certain helper T cell subpopulations. Similarly, naïve macrophages and DCs can differentiate into their respective subpopulations based on the cytokine levels present in the system. The differentiated T cell and macrophage populations can change their phenotype (subtype), that is, the cells in one subtype can differentiate into other subtypes; in other words, differentiated helper T cells and macrophages are phenotypically plastic (Geginat *et al.*, 2014; Bercovici *et al.*, 2019). The model considers this phenotypic plasticity of the helper T cell and macrophage subpopulations, which can help to create more accurate immune dynamics. The cytokines produced by the immune subpopulations play a significant role in determining the inflammatory balance between the pro-inflammatory and anti-inflammatory components of the immune system in the gut.

When the balance is disturbed by perturbations in the system, for example, resulting in higher levels of pro-inflammatory cytokines such as Tumour Necrosis Factor alpha (TNF α) and Interferon gamma (IFN γ), this can lead to an increase in the proliferation of pro-inflammatory immune cells such as M1 macrophages, Th1 cells, effector DCs (eDC), and activated neutrophils (Act_Neu), which in turn produces pro-inflammatory cytokines, effectively creating positive feedback loops in the system. The anti-inflammatory immune components such as Treg cells, M2 macrophages and tolerogenic DCs (tDC) produce responses that dampen this positive feedback loop, thus effectively creating negative feedback loops in the system. The ability to return back to the initial immune homeostatic state depends on the strength of these feedback loops, which can be modified in the model through the manipulation of the parameters. This allows the model to create and simulate different disease modes by manipulating certain parameter values which has a significant impact on key immune pathways determining the immunological balance between the pro- and anti-inflammatory processes.

3.1.2. Simulation of Gut Model

The gut model is simulated until the state variables reach the steady state. We examined the dynamics of the simulations of the gut model for the immune cell populations and cytokines (see Figure 23 in Appendix 3). The model has the flexibility to be simulated in the default healthy mode (HV) and two diseased modes (CD and UC). Figure 6 shows the dynamics of CRP in the blood compartment, Th1 and Treg cells, TNF α and TGF β in the gut compartment for the three modes of the model. The steady-states of Th1 and Treg cells, TNF α and TGF β in the gut compartment indicates the lamina propria is inflamed in the CD and UC model modes compared to the healthy mode; this is also supported by CRP dynamics which indicates there is a systemic inflammation in case of CD and UC, which is observed in patients with Crohn's disease and ulcerative colitis in the clinical setting (Fagan *et al.*, 1982).



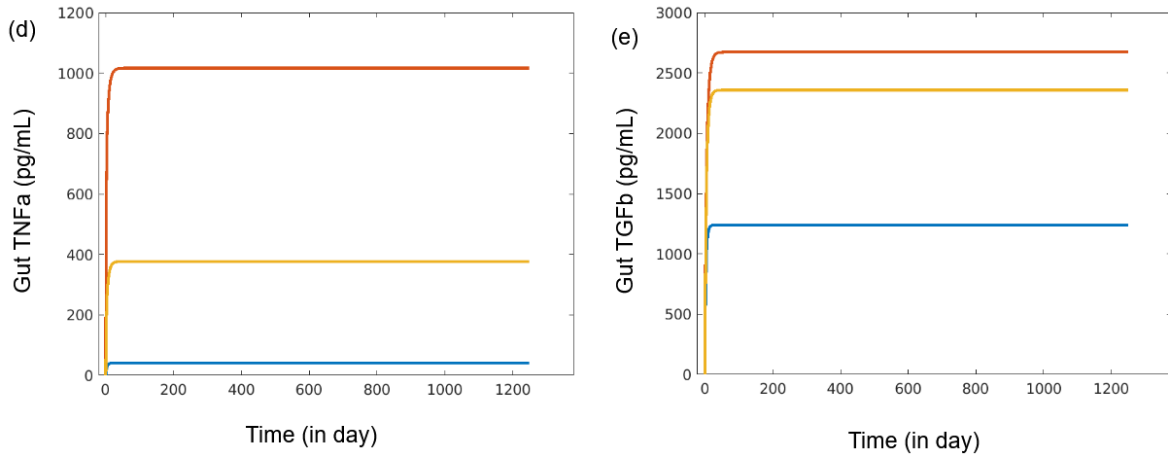


Figure 6: Time Evolution of species in HV, CD and UC modes of the gut model. The dynamics of the simulation of the HV, CD and UC modes of the model for CRP levels in blood (a), helper T cells 1 (b), regulatory T cells (c), TNF α (d) and TGF β (e) levels in gut reveals higher immune activity with increased inflammation in the CD and UC modes of the model.

The model was then simulated for the entire virtual population (Vpop), which was estimated by the authors, to reassess and confirm the conclusions from the paper (Rogers *et al.*, 2021a). We simulated for all 357 virtual patients in the Vpop for all three model modes and the steady state values of the simulation for CRP and activated neutrophils in Gut (Gut_Neu_act) are shown in Figure 7. It is to be noted that we define virtual patient in this thesis as a set of model parameters, and we define a Virtual population as a collection of such parameter sets (virtual patients). Higher activated neutrophil population is indicator of tissue inflammation as they contribute to reactive oxygen species (ROS) level in the microenvironment, which leads to activation of redox-sensitive inflammatory pathways and increased epithelial barrier damage (Biasi *et al.*, 2013). Sustained excessive neutrophil activation is commonly observed in IBD, promoting chronic inflammation and impairment of epithelial barrier function (Wéra *et al.*, 2016). Additionally, calprotectin, whose levels are elevated in faeces of IBD patients, is a cytosolic protein mainly found in neutrophils, and its presence in faeces is an indicator of neutrophil migration and activation in the GI tissue due to inflammation (Erbayrak *et al.*, 2009).

From the figure below (Figure 7), elevated levels of CRP in UC and CD indicates higher systemic inflammation compared to the HV mode and increased activated neutrophil population in CD and UC in comparison to HV suggests gut inflammation

and epithelial tissue damage. This observation is concurrent with the existing literature where CRP and faecal calprotectin (surrogate for neutrophil levels) correlates IBD disease activity (Moniuszko *et al.*, 2013).

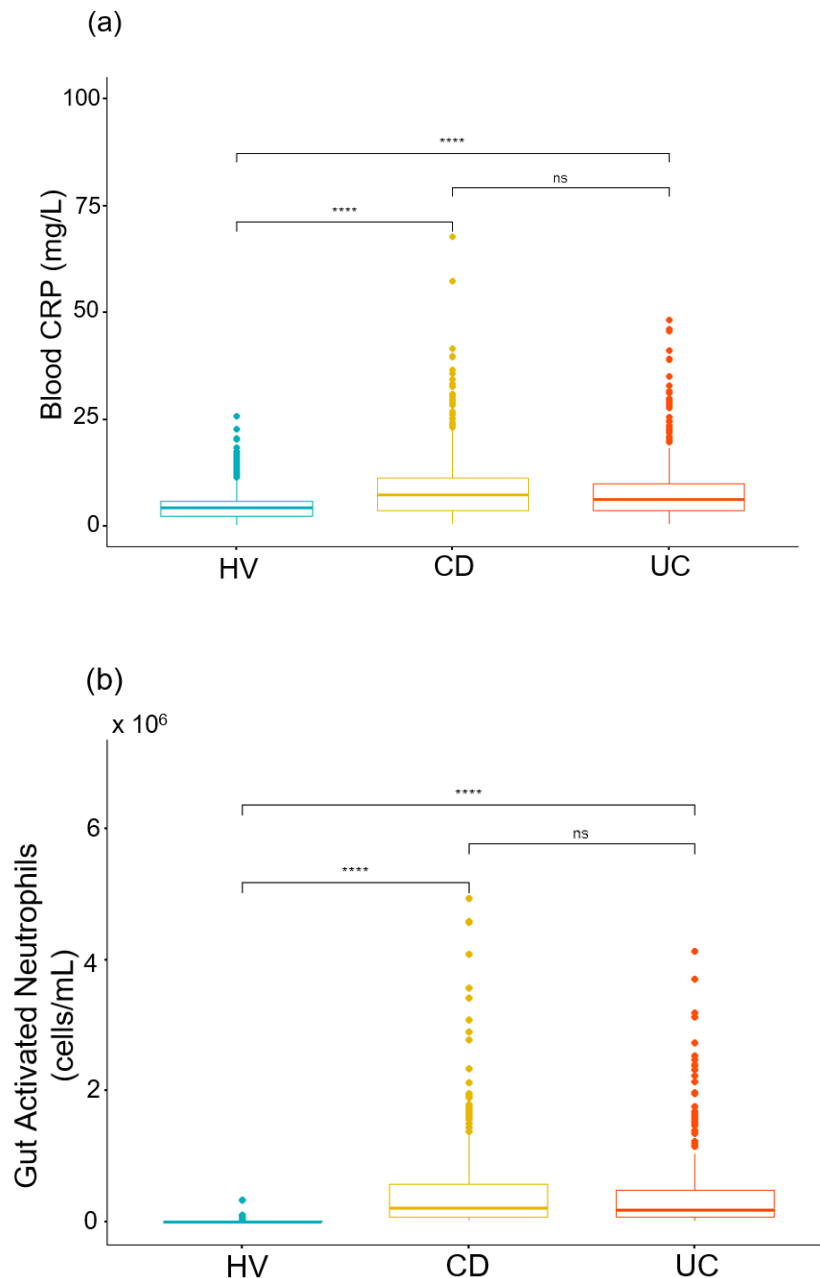
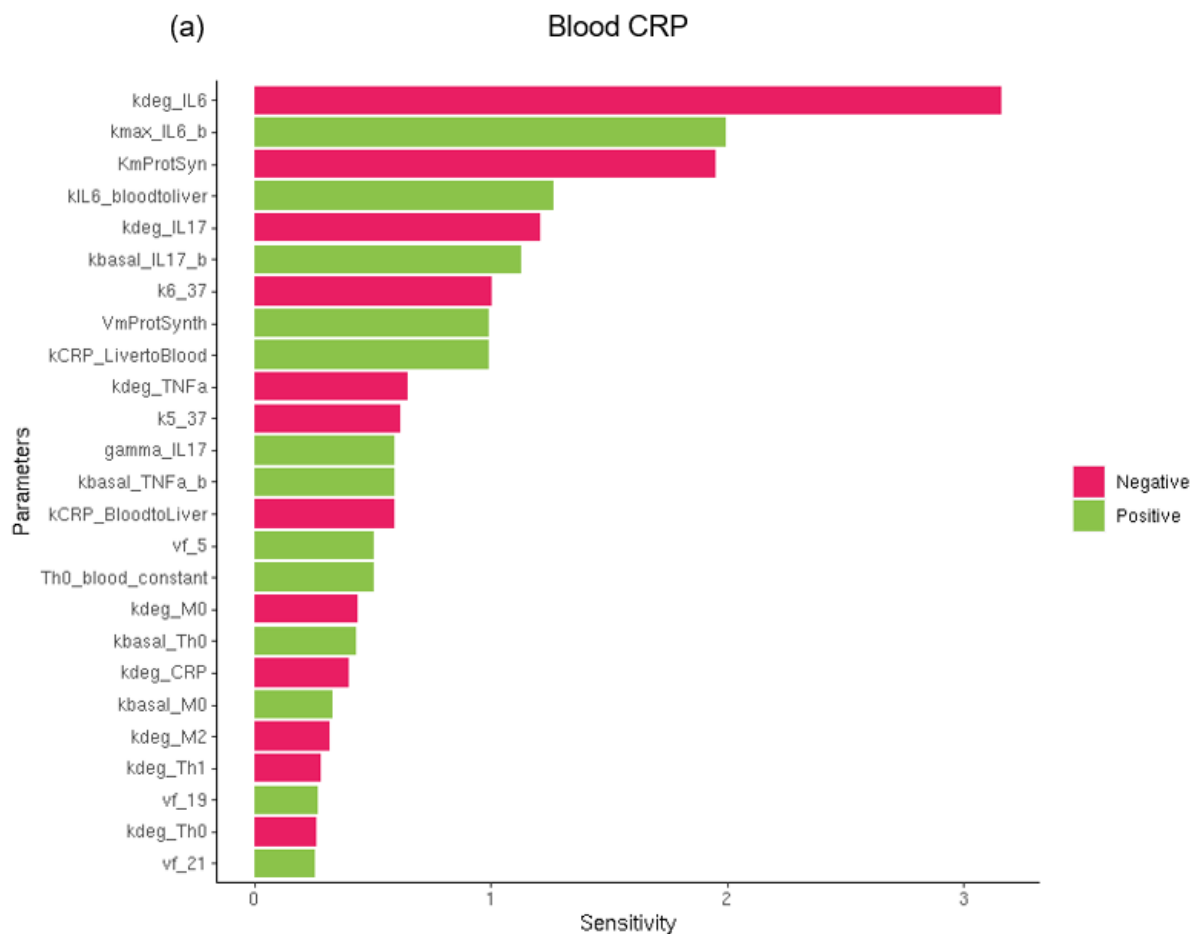


Figure 7: Steady state values of CRP in blood and activated neutrophils in gut for the HV, CD and UC modes of the Gut model. The steady state values of Crohn's disease (CD) and ulcerative colitis (UC) diseased virtual patients is significantly different (p -value $< 2.2e-16$, Kruskal-Wallis's test) compared to healthy volunteers (HV) for both Blood CRP (a) and activated gut neutrophils (b). The bars represent the upper and lower quartiles and the solid line indicates the median.

3.1.3. Sensitivity Analysis of Gut Model

We performed a sensitivity analysis on CRP and activated neutrophils in the gut (Gut_Neu_act) to identify the key mechanisms and interactions that affect their levels in the gut. Figure 8 shows the top 25 parameters that have high sensitivity coefficients, which are obtained from the results of the sensitivity analysis of CRP and Gut_Neu_act respectively. The description of these parameters can be found in Appendix 4 (Table 10 and Table 11). The most sensitive parameters that affect the C-reactive protein (CRP) and gut activated neutrophils levels, which in turn affect the overall immune homeostasis and systemic inflammatory level of the host, are mainly related to IL-6, TNF α , IL-17, neutrophil production, transportation and degradation, the degradation of Th cells and macrophages pathways. These pathways give a mechanistic insight to the influence of gut microenvironment on the systemic immune homeostasis. These observations match with the conclusions made with the IBD model, thus giving an additional verification (Rogers *et al.*, 2021a).



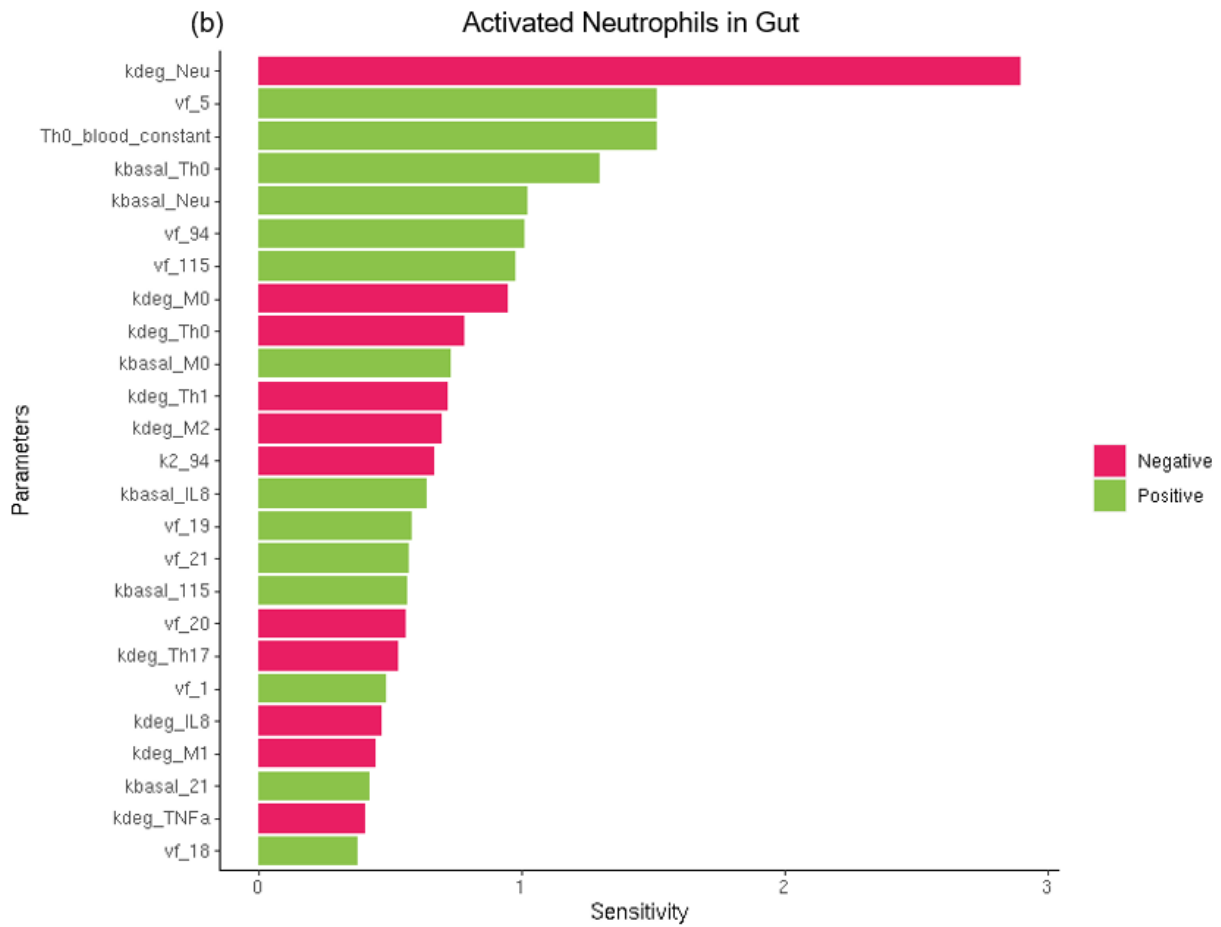
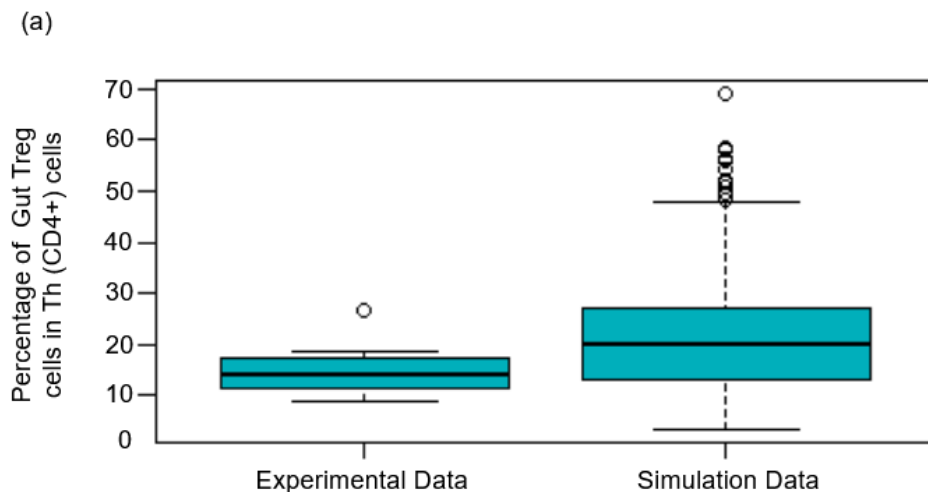


Figure 8: Sensitivity Analysis of CRP in blood and activated gut neutrophils. The sensitivity analysis of CRP in blood (a) and activated neutrophils in gut (b) indicates parameters that associate with IL-6, TNF α , IL-17 pathways as well as pathways affecting production and recruitment of naïve T cells, macrophages, and neutrophils into the gut compartment. The absolute values of the sensitivity coefficient of the parameters are plotted. The colours, red and green, indicates that the parameter has a positive or negative sensitivity coefficient respectively, meaning, a positive valued perturbation in the parameter leads to an increase (green) or decrease (red) in the steady state value of the species compared to the unperturbed parameter simulation of the model.

3.1.4. Preliminary Evaluation of Gut Model

The gut model is evaluated with experimental data generated by the collaborators' groups to give a preliminary qualitative understanding of the model. The HV mode of the model is compared with control mice data generated from the Infection Immunology lab. The IBD model developed by Rogers et al., has also published the parameter values of the Virtual Population, which are validated by the authors with data from the literature as well as their in-house experimental data (Rogers *et al.*, 2021a).

The Virtual Population (Vpop) data from Rogers et al., model is used in the simulations of the HV mode of the Gut model and compared with cytokine measurements and immune cell populations from control mice data, as shown in Figure 9. This preliminary qualitative analysis enabled us to give a precursory understanding of which model species can be evaluated with experimental data, and to what extent the current parameters (parameterised using human clinical data by the authors) fits the mice data and future strategy for model parameterisation using mice data. From Figure 9, though experimental and simulated values of certain species such as Treg, IL6 and TNF α have ranges and median lines overlapping with each other, for other species such as IL17 and IL10, the experimental and simulated values do not overlap with each other. This preliminary qualitative analysis indicates the model has to be reparametrised to fit with experimental data from mice as originally the model parameters for the Vpop, which are taken from the IBD model (Rogers et al., 2021a), were parametrised on human data from clinical settings.



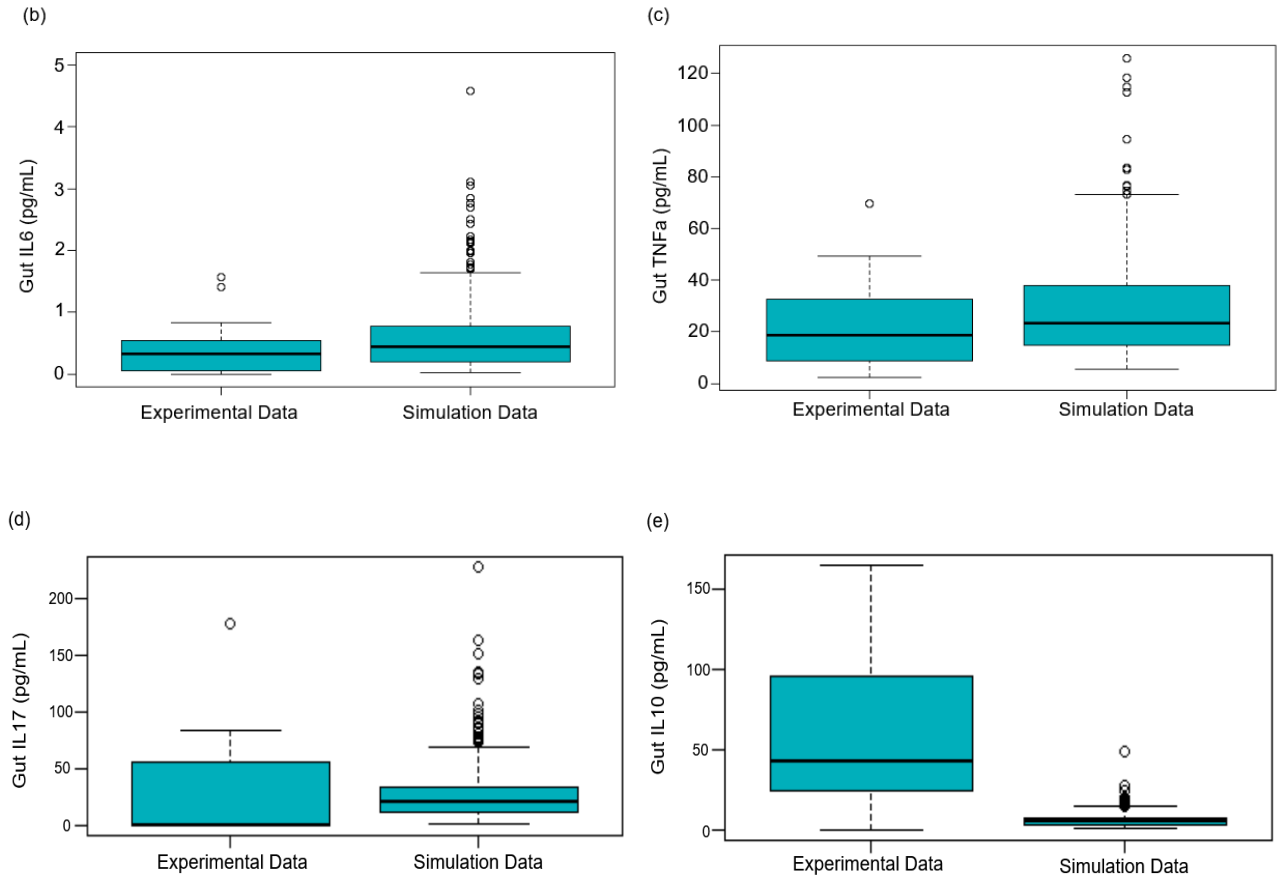


Figure 9: Comparison of steady-state values of species from HV mode of the Gut model with experimental data. The simulated values of the HV mode of the Gut model using the Vpop dataset are compared with flow cytometric and ELISA data from control mice samples for regulatory T cells (a), IL6 (b), TNFa (c), IL17 (d), and IL10 (e) in the gut. The simulated data category in the box plots represents the steady state values of the species indicated in the plots from the HV mode of the model. Comparing the model simulation with experimental data, the steady state value of species from model simulation using parameter values from in the IBD model match with certain species, although many other species do not lie within the ranges of the simulated species values, indicating the model needs to be reparametrised using mice data. For the subplot (a), the percentage of Treg cell population in the total helper T cell population, which includes Th0, Th1, Th2, Th17 and Treg species, was used to generate the box plot for the simulated data category. The bars represent the upper and lower quartiles and the solid line indicates the median. The experimental data used for the analysis is from the Infection Immunology group (headed by Prof Dr Astrid Westendorf) at the Institute for Medical Microbiology at the University Hospital Essen.

3.2. Lung Compartment

3.2.1. Formulation of Lung Model

The QSP model of the lung compartment was adapted from both the inflammatory bowel disease (IBD) model (Rogers *et al.*, 2021a) and the SARS-CoV-2 model (Dai *et al.*, 2021). The immune cell and cytokine interactions for the lung compartment were adapted from the Rogers *et al.*, model and the pulmonary alveolar epithelial cell interactions and its associated damage response mechanisms were adapted from Dai *et al.*, model. The event of radiation and its corresponding immune dynamics were later added into the model. The ODE equations were written in base MATLAB to be compatible with the gut compartment of the model. The resultant lung model has two compartments: Lung and Blood compartments. The model has 49 state species and 231 parameters. Figure 10 shows the mechanistic overview of the lung model with simplified immune dynamics and radiation interactions.

The immune interactions between the immune cells and the cytokines are similar to the interactions modelled in the gut compartment (Figure 5). The lung model couples the interactions of the pulmonary alveolar type 1 and 2 epithelial cells (AT1 and AT2 cells respectively) with the immune components, including pro-inflammatory and anti-inflammatory species. The model also includes the dynamics of the systemic inflammatory marker, C-Reactive protein (CRP), and the alveolar cell damage marker, Surfactant protein D (SPD), which helps to evaluate and compare the model with literature. The lung model also incorporates the dynamics of radiation induced damage mechanisms as well as cytokine-associated damage mechanisms, and inflammatory responses associated with the clearance (cell death) of irradiated and damaged cells.

The detailed explanation of the damage-associated pathways are as follows: the model consists of healthy alveolar AT1 and AT2 epithelial cells, which upon radiation, become irradiated cells. These irradiated cells release damage-associated molecular patterns (DAMPs) into the alveolar space, which damages healthy cells and initiates pro-inflammatory signalling pathways. The healthy cells can also become damaged cells as the result of pro-inflammatory cytokines released by the corresponding immune cells. The damaged and the irradiated cells elicit an inflammatory response mainly dominated by release of pro-inflammatory cytokines (such as IL1, IL6, type 1 interferons and TNF α) into the system when undergoing inflammatory cell death.

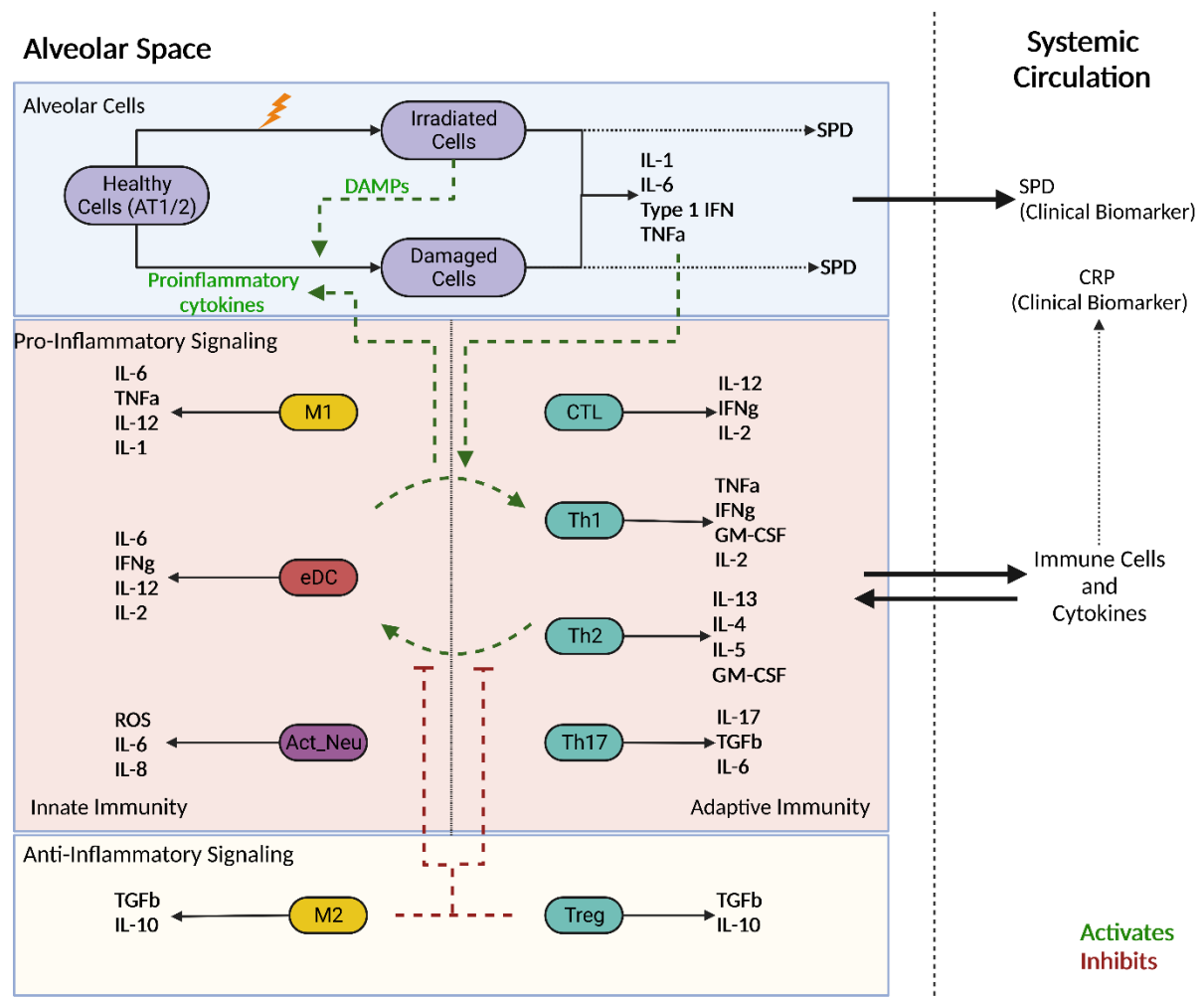
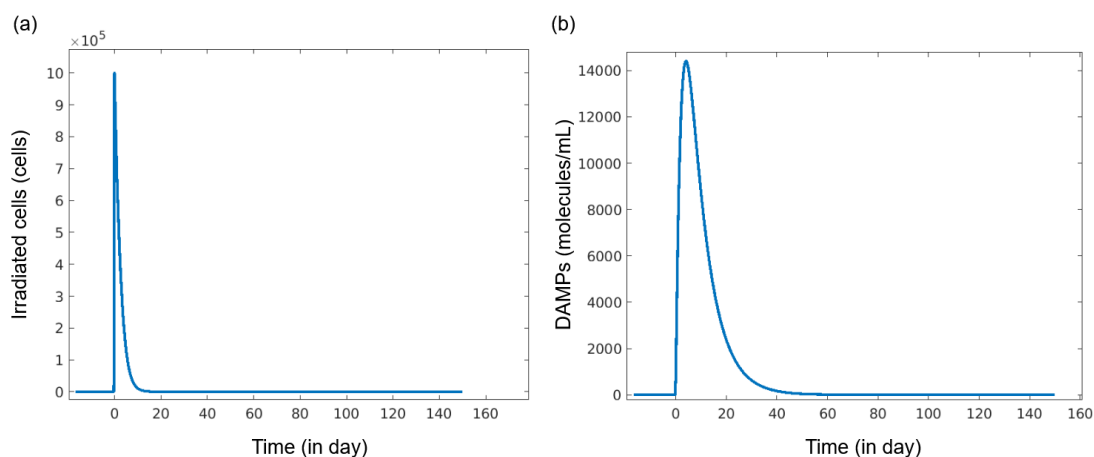


Figure 10: Overview of the mechanistic structure of the Lung compartment. The lung compartment has two major components: the immune interactions, whose simplified mechanics are shown here, has the pro-inflammatory innate and adaptive immune cells along with its corresponding cytokines creating a positive feedback loop and the anti-inflammatory immune cells and cytokines which create a negative feedback loop (for detailed pathways, refer Figure 5); and the alveolar cell interactions, which includes irradiated cells arising from healthy AT1 and AT2 cells upon radiation and damaged cells produced from healthy cells via radiation-induced and cytokine-associated damage mechanisms. The model incorporates the interaction between the two major model components through inflammatory cell death of irradiated and damaged cells, and pro-inflammatory cytokines-associated immune damage creating another positive feedback loop in the system. The model also considers the dynamics of two clinical biomarkers: CRP, a systemic inflammatory marker, modelled as IL-6 induced hepatic production and degradation, and SPD, an indicator of alveolar cell damage and a marker of radiation-induced pneumonitis, modelled as the leakage side-product of damaged and irradiated alveolar cells. The solid black arrows indicate the individual reaction, whereas the coloured dotted lines has a positive (green) or negative (red) influence on the reaction. The black dotted lines for the clinical biomarkers represent the production (indirect) of them. Species in green and red indicates that it has a positive or negative impact on the reaction respectively. Figure created with BioRender.com

3.2.2. Simulation of Lung Model

After the formulation, the lung model is simulated, and the ODE simulation settings are set appropriately to ensure that the state variables reach the steady state. The dynamics of the alveolar cell and immune cell populations, and cytokines in the model are examined and are shown in Figure 24 in Appendix 5. The radiation event is modelled into the lung compartment and the event is triggered after the system reaches the steady state. Figure 12 shows the dynamics of irradiated cells, damage-associated molecular patterns (DAMPs) and damaged cells as well as immune cell populations and cytokines in lung compartment, and CRP in blood compartment.

Upon the event of radiation, there is an increase in the irradiated cell population which results in acute inflammation in the lung compartment, which can be inferred by examining the dynamics of CRP and pro-inflammatory cells and cytokines such as M1, Th1 cells and $\text{TNF}\alpha$. In addition to the cytokine-associated damage caused by pro-inflammatory cytokines, the DAMPs produced by irradiated cells cause an increase in damaged AT1 and AT2 cell populations, which further increases inflammation in the system. The anti-inflammatory species such as Treg cells and $\text{TGF}\beta$ get activated in response to the acute inflammation and starts damping the pro-inflammatory interactions. This anti-inflammatory response results in pro-inflammatory responses to peak and starts reducing, which results in anti-inflammatory responses peaking and decreasing their response to maintain the balance between both of these responses, thus ensuring the system is brought back to its original state. The model also captures the qualitative dynamics, such as time lags between the peaks of pro-inflammatory and anti-inflammatory species. However, the model needs to be validated for quantitative inferences and conclusions.



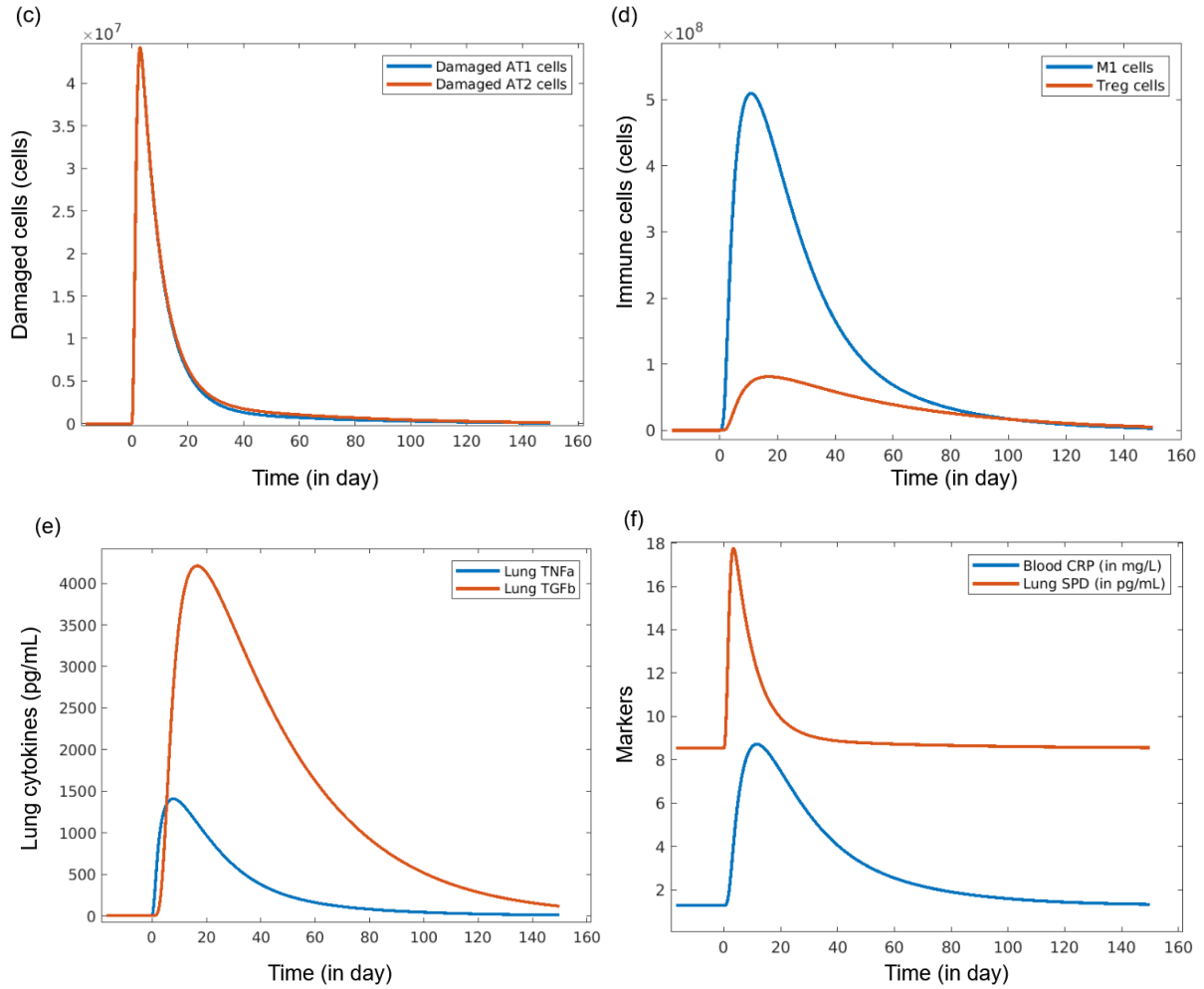
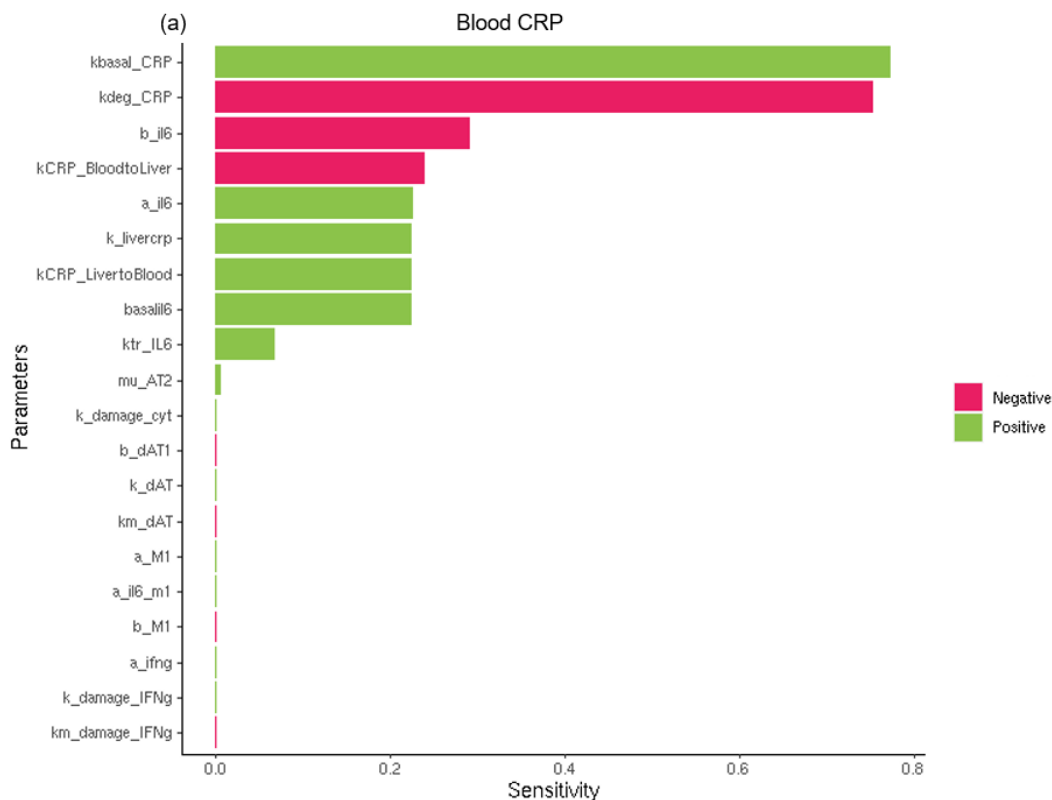


Figure 11: Time Evolution of species in the lung model upon radiation. The model is simulated until the species reaches the steady state, upon which, at time $t = 0$, the radiation event is initiated. This results in the irradiated cell population (a) to increase, which results in the production of DAMPs (b). The DAMPs cause healthy cells to become damaged AT1 and AT2 cells (c, blue and red respectively), which activates the pro-inflammatory species such as M1 cells (d, blue) and $\text{TNF}\alpha$ (e, blue), which results in inflammation locally and systemically, indicated by CRP (f, blue), as well as leads to increase in pro-inflammatory cytokine-associated damage, indicated by SPD (f, red). The anti-inflammatory components in the system, such as Treg cells (d, red) and $\text{TGF}\beta$ (e, red), contribute to the reduction of inflammation in the lungs which brings the system back to its original steady-state values. This can be noted by the time lag between the peaks of pro-inflammatory components (M1 and $\text{TNF}\alpha$) and anti-inflammatory components (Treg and $\text{TGF}\beta$) respectively. It is to be noted that the dynamics of damaged AT1 and AT2 cells are similar and their population graphs overlap with each other. Also, to be noted that the units of CRP and SPD are different even though they are shown in the same numerical y-axis.

3.2.3. Sensitivity Analysis of the Lung Model

In order to identify parameters in the key pathways that affect the biomarkers in the lung model, a sensitivity analysis of CRP and SPD was performed, and the top 20 parameters and their corresponding sensitivity coefficients were reported (Figure 12, a and b). Additionally, we also performed a sensitivity analysis on damaged alveolar cells to identify mechanisms that played an important role in determining the damage responses in the lung model (Figure 12, c). The description of the sensitive parameters is given in Table 12 to Table 14 in Appendix 6. From the analysis of these species, we identified pathways that are known in literature and have a direct effect on the dynamics of the species. For example, parameters that correspond to the IL6 production and degradation have a significant impact on the CRP levels, as it directly affects the rate of production of CRP. However, we identified parameters that have an indirect impact on the output of the species, which is of interest to us; for instance, parameters that relate to the sensitivity of inflammatory cell death for IL6, IL1b, IFN γ and TNF α pathways were identified to be of interest in the sensitivity analysis of SPD and damaged AT2 cells, and these parameters, when changed, show differential dynamics and outcomes when the model is simulated even if the rest of the parameters are left unmodified.



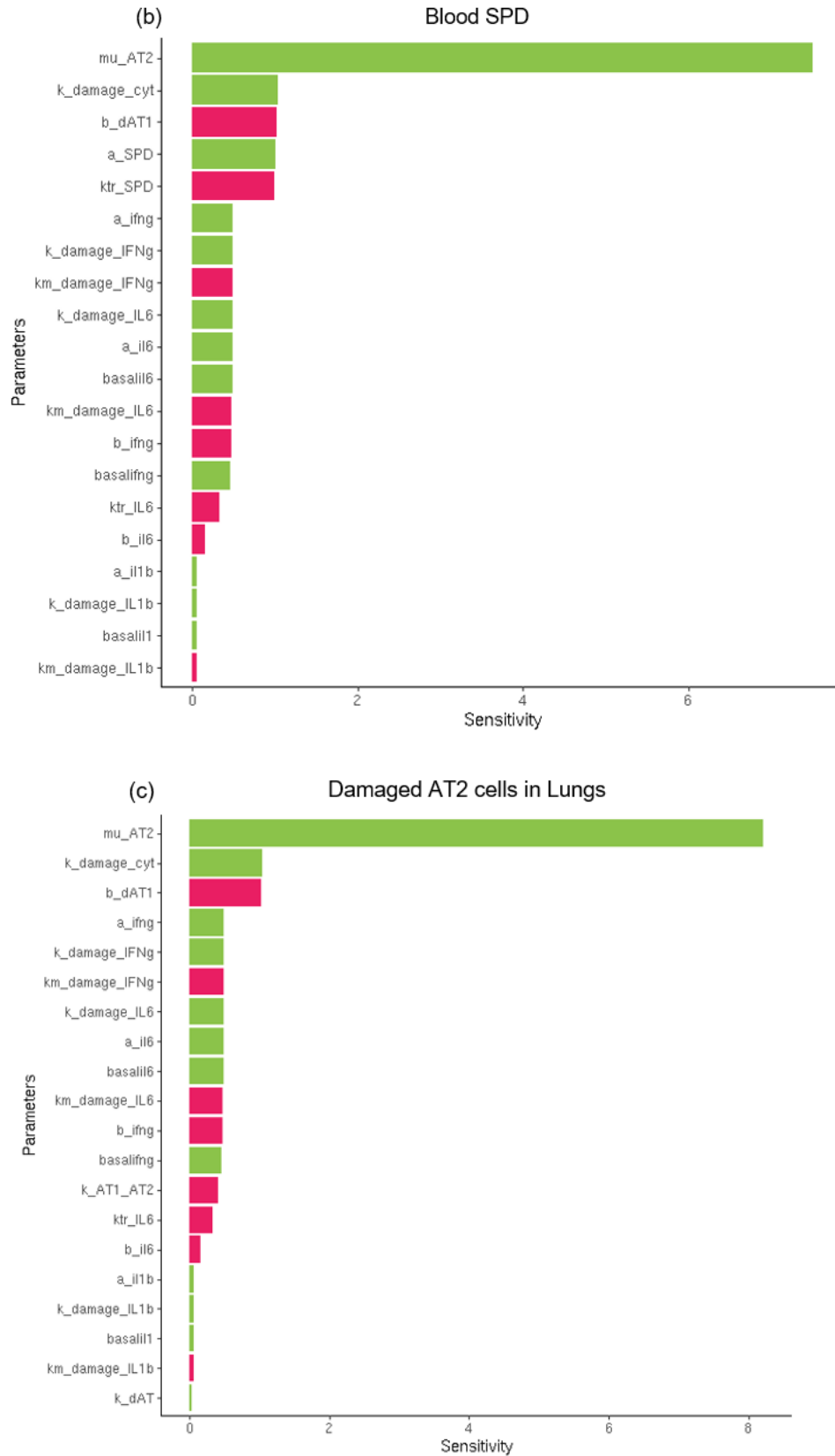


Figure 12: Sensitivity Analysis of CRP, SPD and damaged AT2 cells in the Lung model. The sensitivity analysis of CRP in blood (a) identifies sensitive parameters mainly related to the IL6 pathway along with parameters that relate to the production, transportation, and degradation of CRP. The

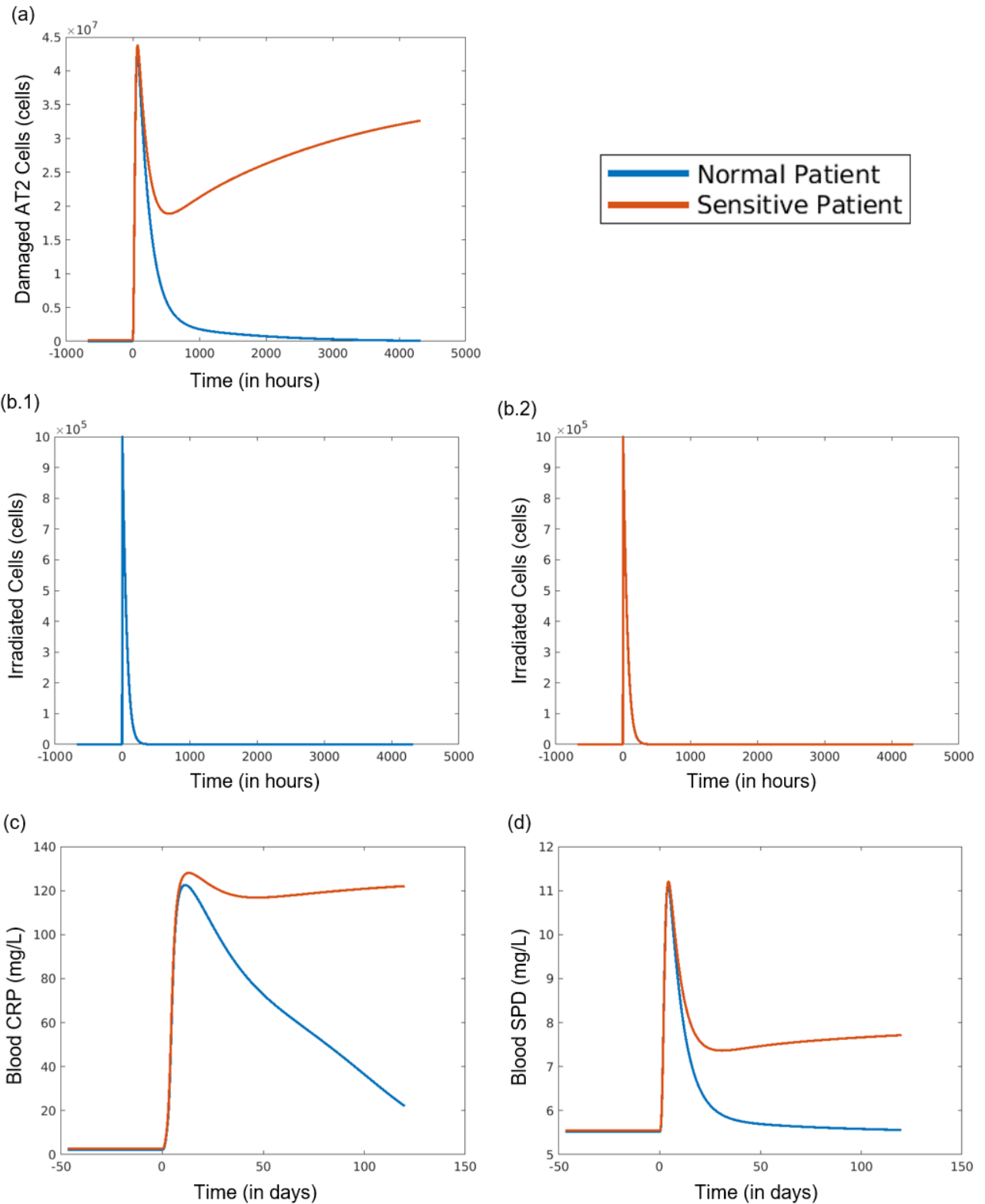
sensitivity analysis of SPD in blood (b) and damaged AT2 cells in lungs (c) reveals parameters of interest that relate to inflammatory cell death ($k_{\text{damage_IFNg}}$, $k_{\text{damage_IL6}}$, $k_{\text{damage_IL1b}}$ and $k_{\text{damage_TNFa}}$). The absolute values of the sensitivity coefficient of the parameters are plotted. The colours, red and green, indicate that the parameter has a positive or negative sensitive coefficient, respectively.

3.2.4. Simulation of the Diseased Mode of the Lung Model

The parameters identified from the sensitivity analysis of SPD in blood and damaged alveolar type-2 epithelial cells (AT2) in lungs were increased by a factor of 10, retaining the original values of the other parameters and the resultant lung model is simulated. The steady-state dynamics of the state variables of the simulation were similar to that of the original simulation, where all parameter values were kept unchanged. However, upon the event of radiation, there were differential species dynamics observed between the model's two modes, as shown in Figure 13. The species dynamics of the unmodified model (hereafter referred to as the normal mode or normal virtual patient in the thesis) returned back to the original levels, indicating a return back to the normal state. However, the dynamics of the modified model (hereafter referred to as radiation sensitive virtual patient or simply, sensitive virtual patient in the thesis), whose parameters correspond to the cell's sensitivity to cytokine-associated damage, remains elevated and doesn't return back to the normal levels, indicating the onset of chronic inflammation upon radiation, which resembles patients susceptible to developing radiation-induced pneumonitis after radiotherapy, which usually observed between 3 and 12 weeks (Graves *et al.*, 2010). This is supported by the increased levels of CRP and SPD in blood compared to the normal mode of the model, suggesting systemic inflammation and higher pulmonary alveolar damage, which are characteristics of radiation pneumonitis (Schaue *et al.*, 2015).

The differential simulation dynamics of the normal and the radiation sensitive virtual patients lead to the conclusion that even though both of these patients are healthy and do not show any signs of inflammation and alveolar damage pre-radiation, the radiation sensitive virtual patient develops chronic inflammation and increased damage responses post-radiation compared to the normal virtual patient, thus suggesting that the radiation sensitive virtual patient is susceptible to developing radiation pneumonitis after radiation. This can provide a mechanistic explanation of

the heterogeneity observed in populations developing complications such as pneumonitis after radiotherapy.



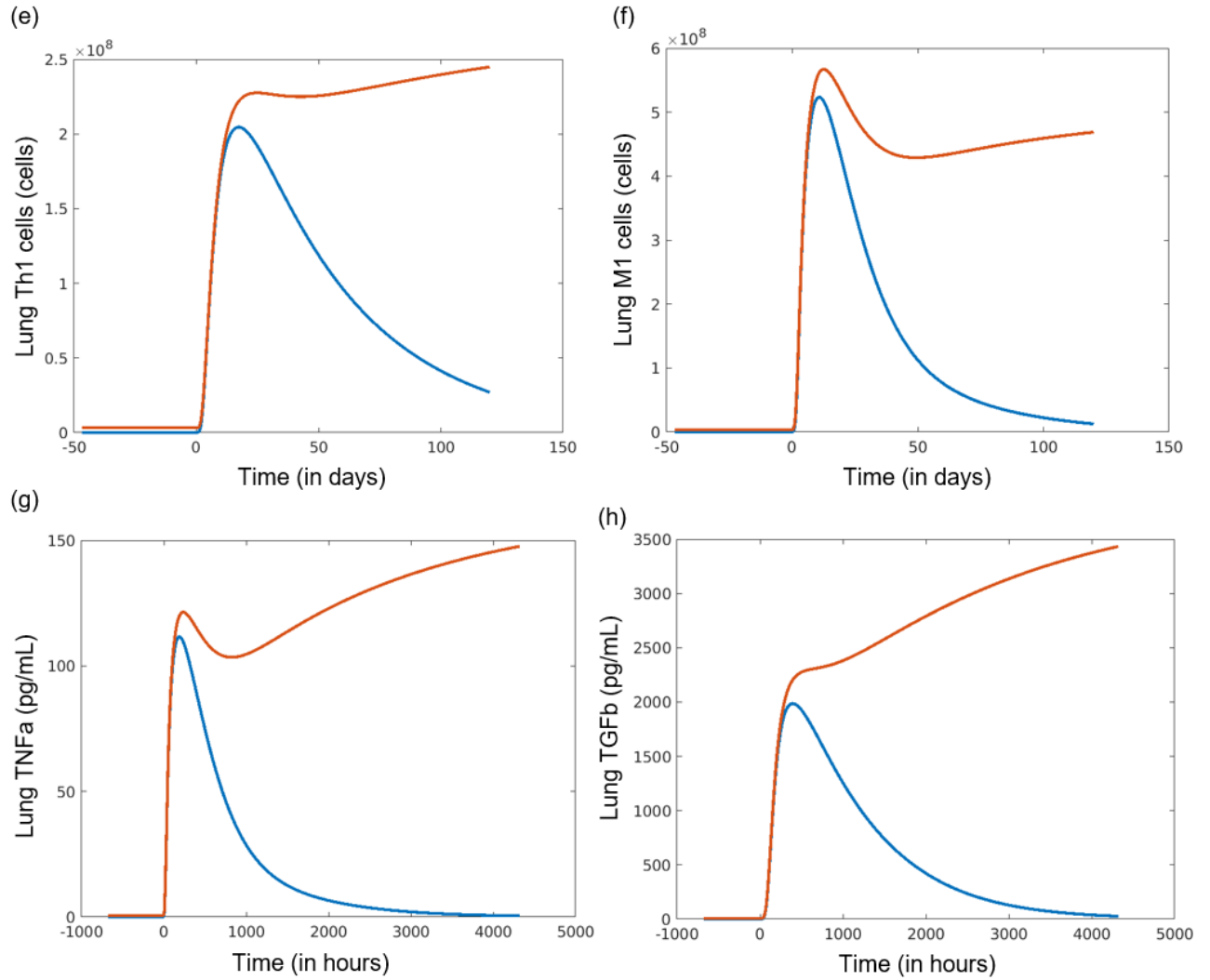


Figure 13: Time Evolution of species in the normal and radiation sensitive mode of the lung model upon radiation. The two modes of the lung model, normal (blue) and radiation sensitive (red) virtual patient, were simulated until they reach steady state. The radiation event is initiated at $t = 0$, and the two modes of the model were simulated for 180 days. Upon radiation, the damaged AT2 cells (a) for the sensitive patient remains higher than the normal patient even though the irradiated cell population for the sensitive patient (b.1) and the normal patient (b.2) declines and becomes zero, indicating the damaged AT2 cells are produced through cytokine-associated damage processes. The virtual patient has a higher inflammation and alveolar damage responses than normal patient, suggested by CRP (c) and SPD (d) in blood. This increased inflammation and alveolar damage is mediated through imbalance between pro-inflammatory and anti-inflammatory processes. The pro-inflammatory components such as helper type 1 T cells (e), M1 macrophages (f) and $\text{TNF}\alpha$ (g) are excessive in radiation sensitive patient in comparison to the normal patient, thus contributing to the chronic inflammation in the radiation sensitive patient. The anti-inflammatory species such as $\text{TGF}\beta$ (h) are also higher in virtual patient compared to the normal patient, but they aren't able to dampen the pro-inflammatory processes in the virtual patient and bring the system back to the original normal state as observed in the normal patient.

3.2.5. Flow Cytometric Data of Immune Populations from Mice

Various immune cell populations including major myeloid cells and lymphocytes in different tissues were measured using flow cytometry. The optimal gating strategy for the acquisition of the major immune cells and their subtypes in the lungs, spleen, blood and lymph nodes were chosen, and the description of the chosen gating strategies for myeloid cells, alveolar/interstitial macrophages, lymphocytes and dendritic cells are reported in Figure 14 to Figure 17 respectively.

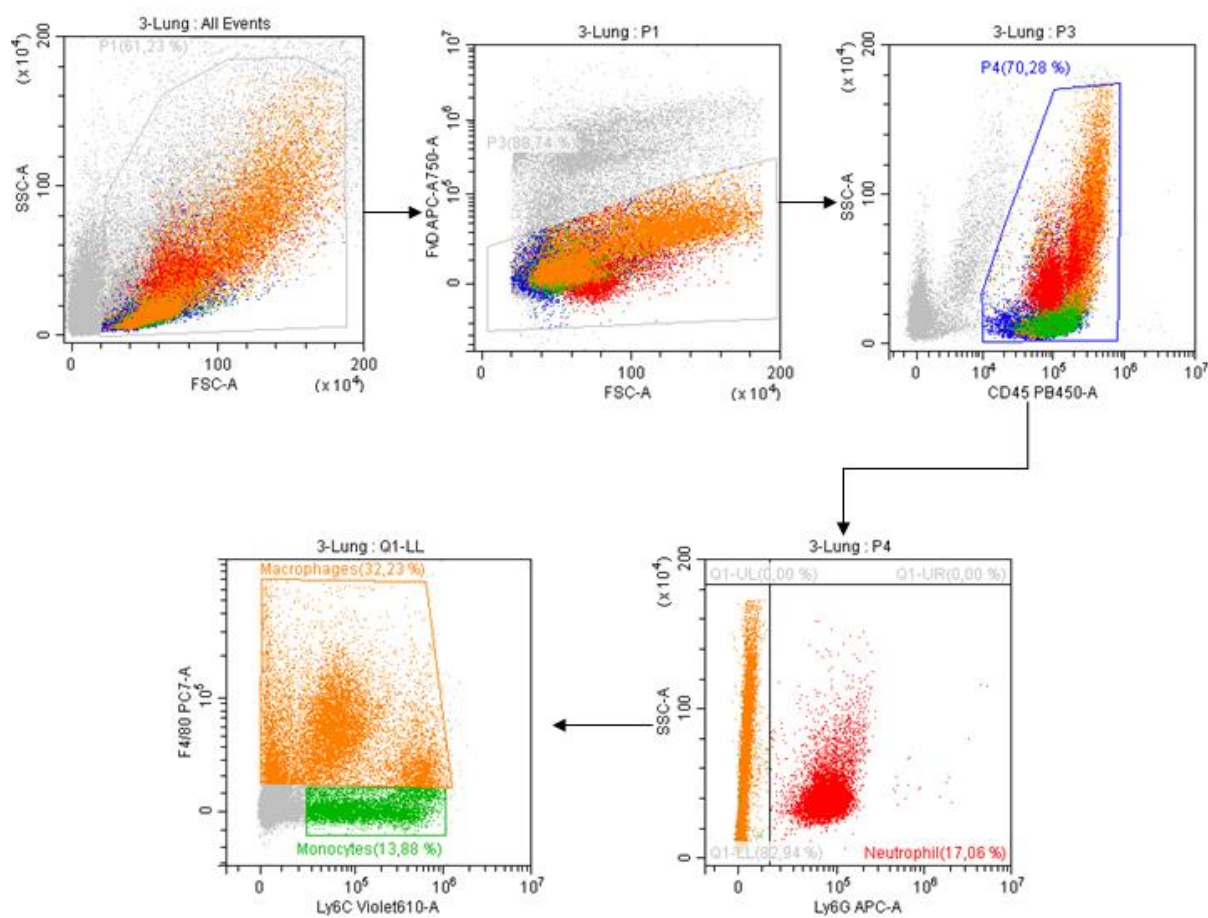


Figure 14: Gating Strategy for myeloid cells. All the acquired events in the instrument were gated based on the FSC-A and SSC-A and debris was excluded. Living cells were selected based on their negative stain for the fixable viability dye. The immune cells were selected based on the expression of CD45 marker. These cells were gated based on Ly6G expression and cells that were positive for Ly6G marker were considered to be neutrophils. The cells that were negative for Ly6G were further gated based on F4/80 and Ly6C expression. The cells that were positive for the expression of F4/80 were classified as macrophages and cells that are Ly6C positive were considered as monocyte cells.

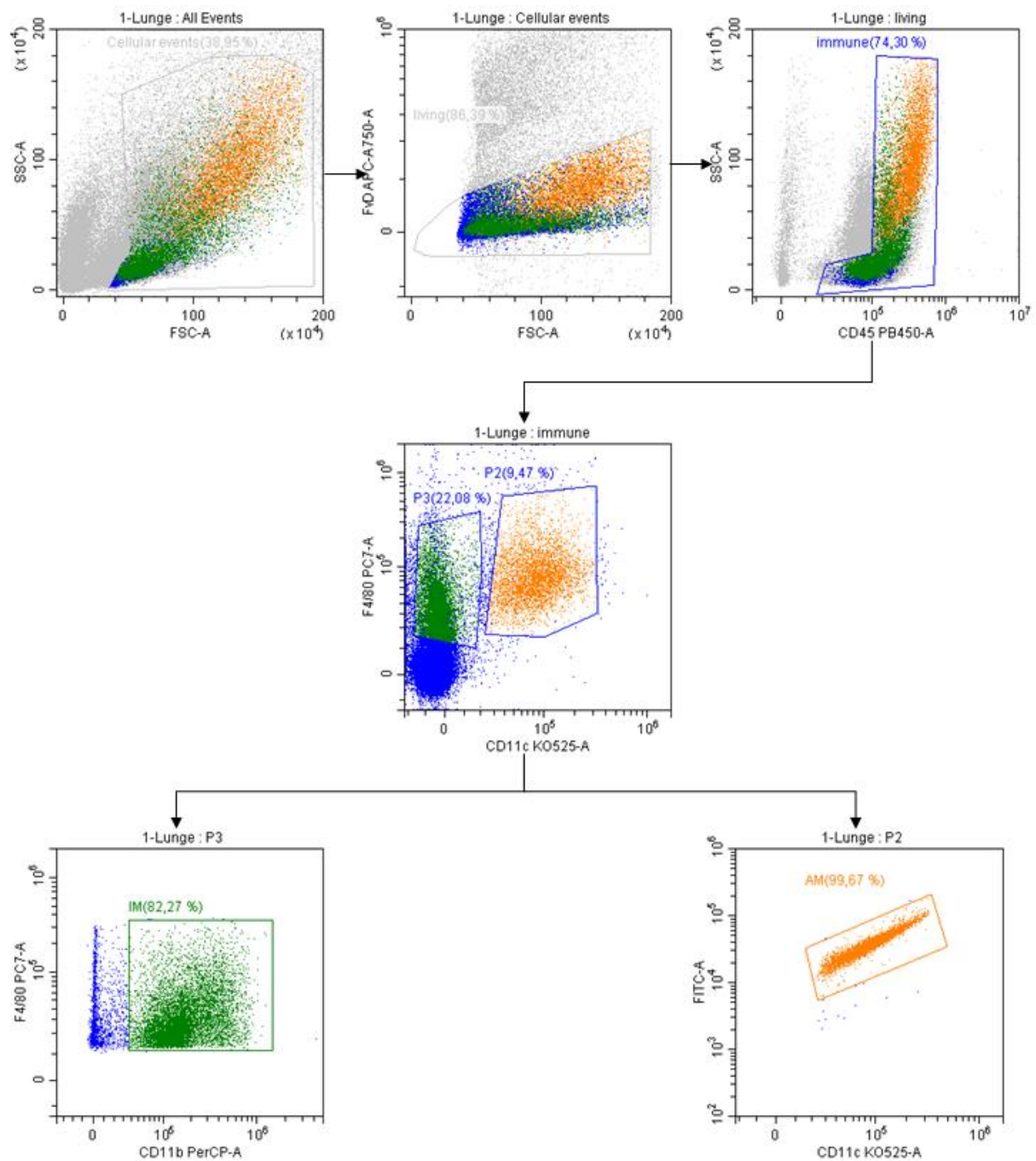


Figure 15: Gating Strategy for alveolar and interstitial macrophages. After the initial gating based on forward scatter (FSC-A) and side scatter (SSC-A) to exclude debris, living cells were selected based on the exclusion of the dead cells through the FvD staining. Cells that were positive for CD45 were considered to be as cells with hematopoietic origin, and this population was further gated based on the expression of F4/80 and CD11c markers. The cells that were positive for F4/80 and negative for CD11c were selected, and these cells which are CD11b positive were considered as interstitial macrophages. The other population that was positive for both F4/80 and CD11c were considered as alveolar macrophages.

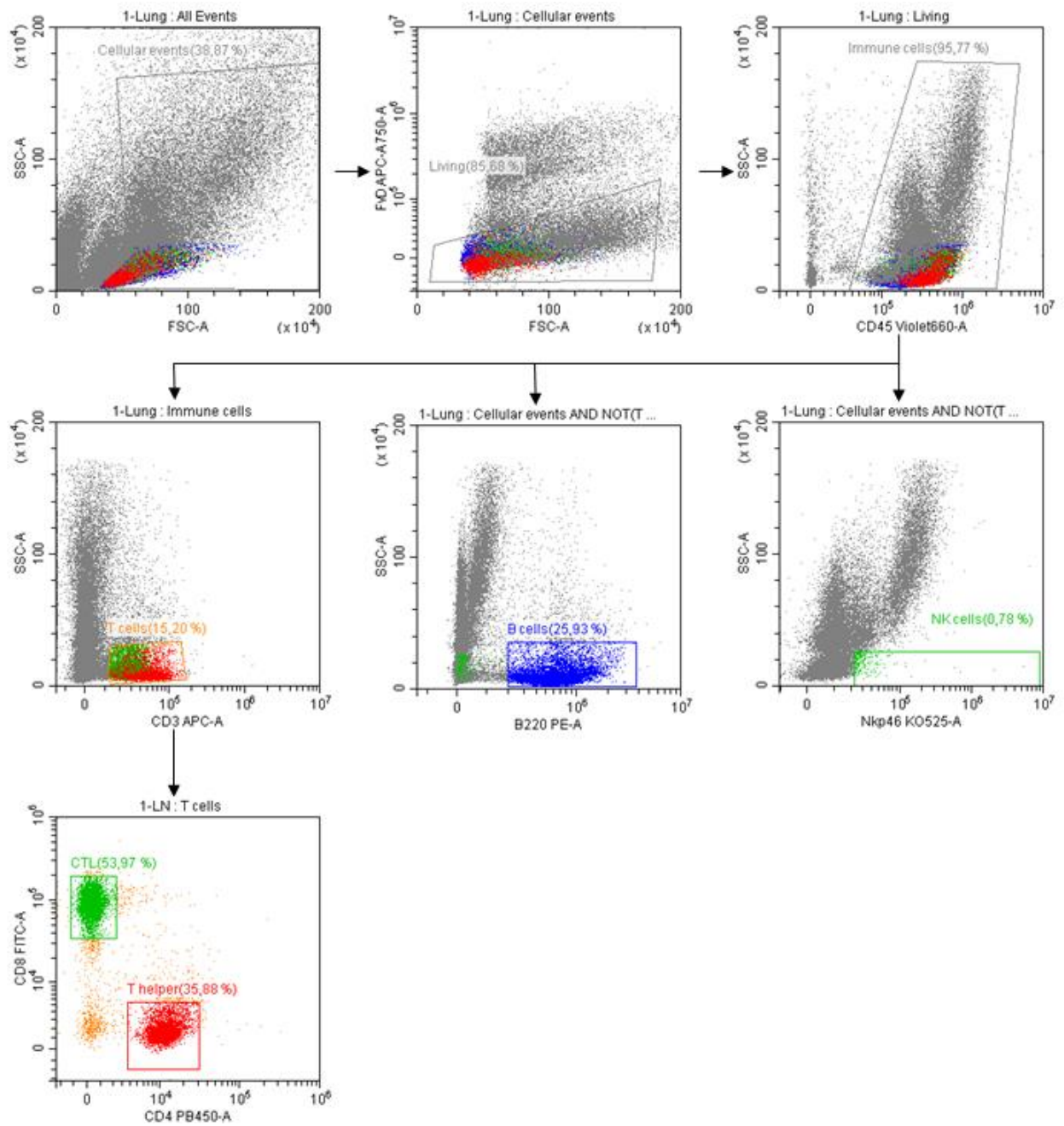


Figure 16: Gating Strategy for Lymphocytes. All events recorded on the flow cytometer were gated on the FSC-A and SSC-A, and living cells were selected based on their negative stain for FvD (eFluor780). Cells with hematopoietic origin were gated based on the CD45+ expression from the living cells. From the immune cell population, cells that were positive for CD3 were considered to be T cells, and cytotoxic and helper T cells were selected by gated from the T cell population based on their CD8 and CD4 expression respectively. Immune cells that were not T cells were further gated into B cells and NK cells based on the B220 and Nkp46 expression.

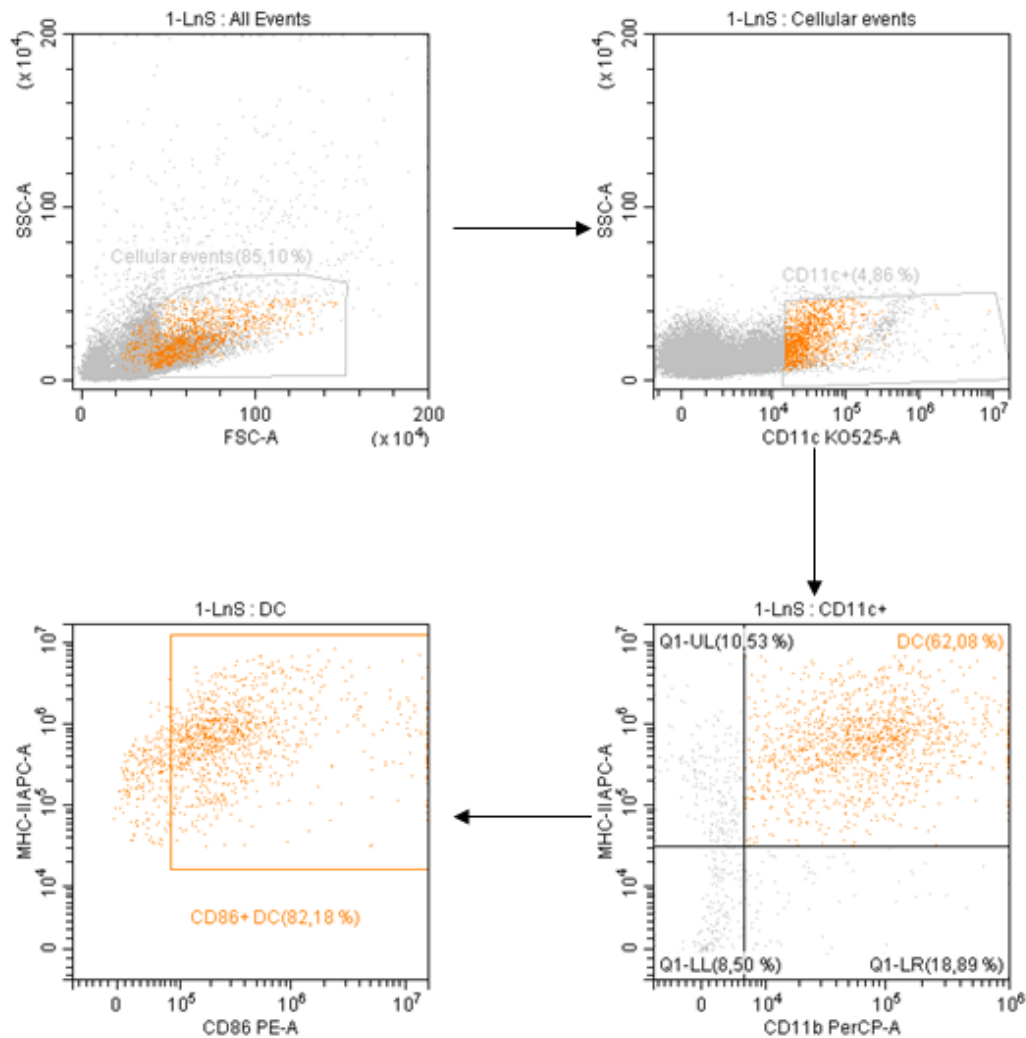


Figure 17: Gating Strategy for Dendritic Cells (DCs). The cellular events were gated based on their characteristic forward scatter (FSC-A) and side scatter (SSC-A) plot and this population was gated on the expression of CD11c marker. Cells that were positive for CD11c expression were then gated based on CD11b and MHC-II marker expressions. Cells that both positive for CD11b and MHC-II markers were considered as dendritic cells. This DC cell population was further gated based on CD86 expression to identify mature DC cells.

The flow cytometric data collected from the lungs, spleen, blood and lymph nodes of three control mice, and the average immune cell population for all the mice samples is reported in Table 6. The individual cell count data for each mouse and their corresponding calculations are described in Table 15 in Appendix 7. This data is merged with the experimental data provided by Jendrosseck's lab from previous and ongoing projects.

Organ	Cell Type	Average percentage of cell type in total immune population
Lungs	T cells	20.09123384
Lungs	Cytotoxic T cells	7.098509688
Lungs	B cells	41.14852614
Lungs	NK cells	0.262301605
Lungs	Neutrophils	14.52179225
Lungs	Monocytes	7.982348146
Lungs	Total Macrophages	19.49375433
Lungs	Alveolar Macrophages	11.61278644
Lungs	Interstitial Macrophages	15.33663491
Blood	T cells	12.92067565
Blood	Cytotoxic T cells	6.083434797
Blood	Helper T cells	4.949494563
Blood	B cells	24.08700398
Blood	NK cells	0.485328553
Spleen	T cells	38.71010656
Spleen	Cytotoxic T cells	16.93919305
Spleen	Helper T cells	16.17360597
Spleen	B cells	49.38912646
Spleen	NK cells	0.057256651
Spleen	Dendritic Cells	3.71319298
Lymph Nodes	T cells	51.48301425
Lymph Nodes	Cytotoxic T cells	24.46496919
Lymph Nodes	Helper T cells	22.09624425
Lymph Nodes	B cells	38.96490316
Lymph Nodes	NK cells	0.015948945
Lymph Nodes	Dendritic Cells	2.591262319

Table 6: Summary of flow cytometric measurements of different immune cell populations from mice. The table shows the average percentage of immune cell type, including major lymphocytes and myeloid cell lineages, in the total immune cell population in different tissues such as lungs, blood, spleen and lymph nodes. The numbers reported in the above table are the mean of all mice samples and the detailed calculations of individual samples are outlined in Table 15 in Appendix 7.

The results from the flow cytometric measurements, along with additional data from the collaborator's group (Prof Dr Verena Jendrosseck) will be used to evaluate the lung model. Currently, the lung model does not have a virtual population, so evaluating the present model with one simulated data point against the experimental data does not bear investigation. So, the evaluation of the lung model needs to be performed in the future to ensure accuracy, reliability and, more importantly, the validity of the results generated from the model.

3.3. Gut-Lung Axis (GLA) Model

3.3.1. Formulation of the GLA Model

The modularity of the Gut and the Lung model, which are developed separately, enables the models to be combined to form the final Gut-Lung Axis (GLA) model. The gut-lung axis model is implemented by combining the gut and the lung compartments, allowing for the inter-compartmental migration of species through the blood compartment. The ODE equations relating to the transportation of immune species such as cytokines between the blood compartment and the gut and lung compartments were included in the model. The final GLA model consists of 76 state variables and 533 parameters, which is described in Table 7 and Table 8 in Appendix 1, respectively. Figure 18 gives the overall picture of the compartments present in the model and the major processes happening in the final GLA model.

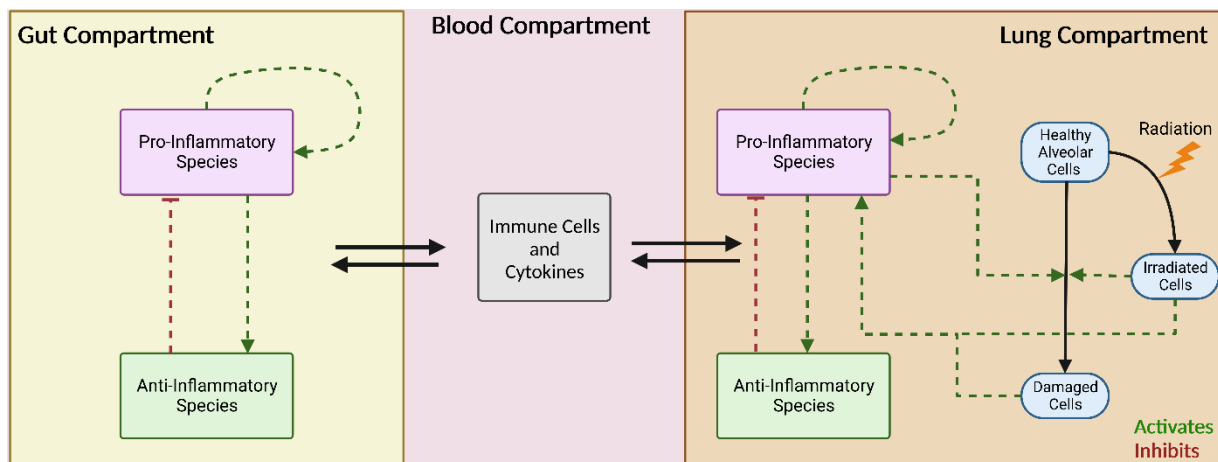
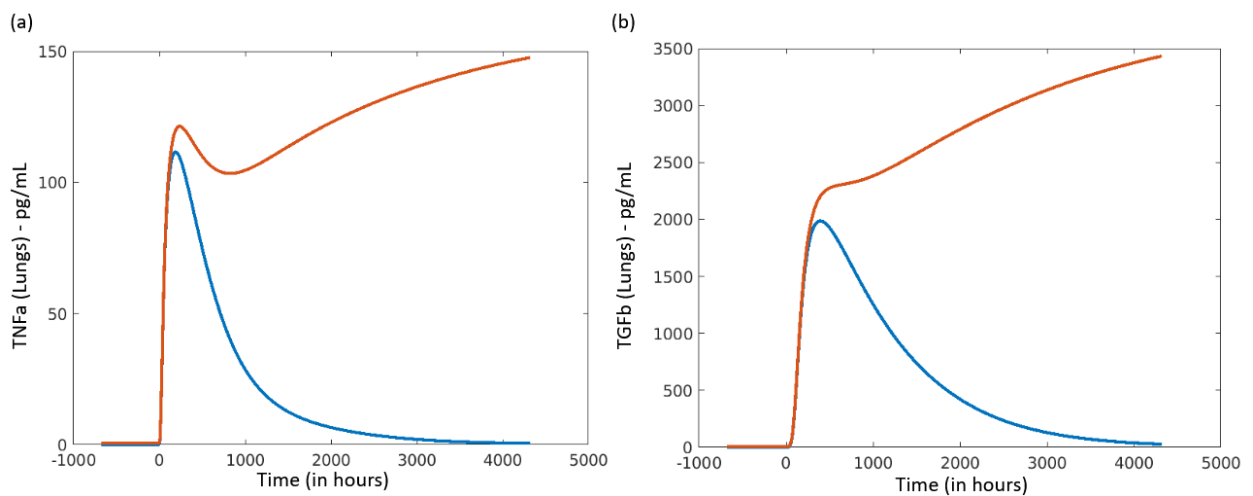


Figure 18: Simplified overview of the mechanistic structure of the Gut-Lung Axis model. The final Gut-Lung Axis (GLA) model has three compartments: Gut, Blood and Lung compartments. The Gut and the Lung compartments include the major immune interactions including both pro-inflammatory and anti-inflammatory processes. The Lung compartment additionally has interactions related to alveolar damage processes induced by irradiation as well as pro-inflammatory cytokines-associated damage processes. The immune cells and the cytokines get transported between the Gut and the Lung compartments through the Blood compartment. The model also has biomarkers, CRP and SPD, dynamics (not shown in the figure). The solid black arrows indicate the reaction such as the production or transportation of species, whereas the coloured dotted lines indicate that the species has a positive (green) or negative (red) influence on the reaction. For detailed information on the individual processes happening in each compartment, refer to Figure 5 and Figure 10 for the interactions in the Gut and the Lung compartments, respectively. Figure created with BioRender.com

3.3.2. Simulation of the GLA Model

The GLA model is simulated until all species reach their steady state upon which the radiation event is introduced. The model is simulated for both normal and radiation sensitive virtual patient modes as described in Figure 13, essentially the parameters that varied between the normal and the radiation sensitive virtual patient (i.e., parameters relating to inflammatory cell death, which are $k_{\text{damage_IFNg}}$, $k_{\text{damage_IL6}}$, $k_{\text{damage_IL1b}}$ and $k_{\text{damage_TNFa}}$) are changed by a factor of eight for the radiation sensitive patient, which is chosen based on parameter perturbation as seen in Figure 22. The dynamics of the $\text{TNF}\alpha$ and $\text{TGF}\beta$ upon the event of radiation are recorded and plotted as shown in Figure 19. The dynamics of the species in the lung compartment are similar to the individual lung model (Figure 13). However, a perturbation in the lung, i.e., changes in the species dynamics of the lung compartment, caused as the result of radiation event, propagates to the other compartment and is reflected in the blood and the gut compartments. This indicates the radiation event has a systemic effect on the model resulting in the changes in the species dynamics in the blood and gut compartment. The impact on the immune processes in the gut compartment is much higher when the virtual patient develops radiation pneumonitis, as seen in Figure 19. The immunological modulation in the gut, as the result of developing radiation pneumonitis in lungs, and the emerging inflammation in the gut can potentially have an impact on the gut microbiome composition and functionality, which needs to be investigated.



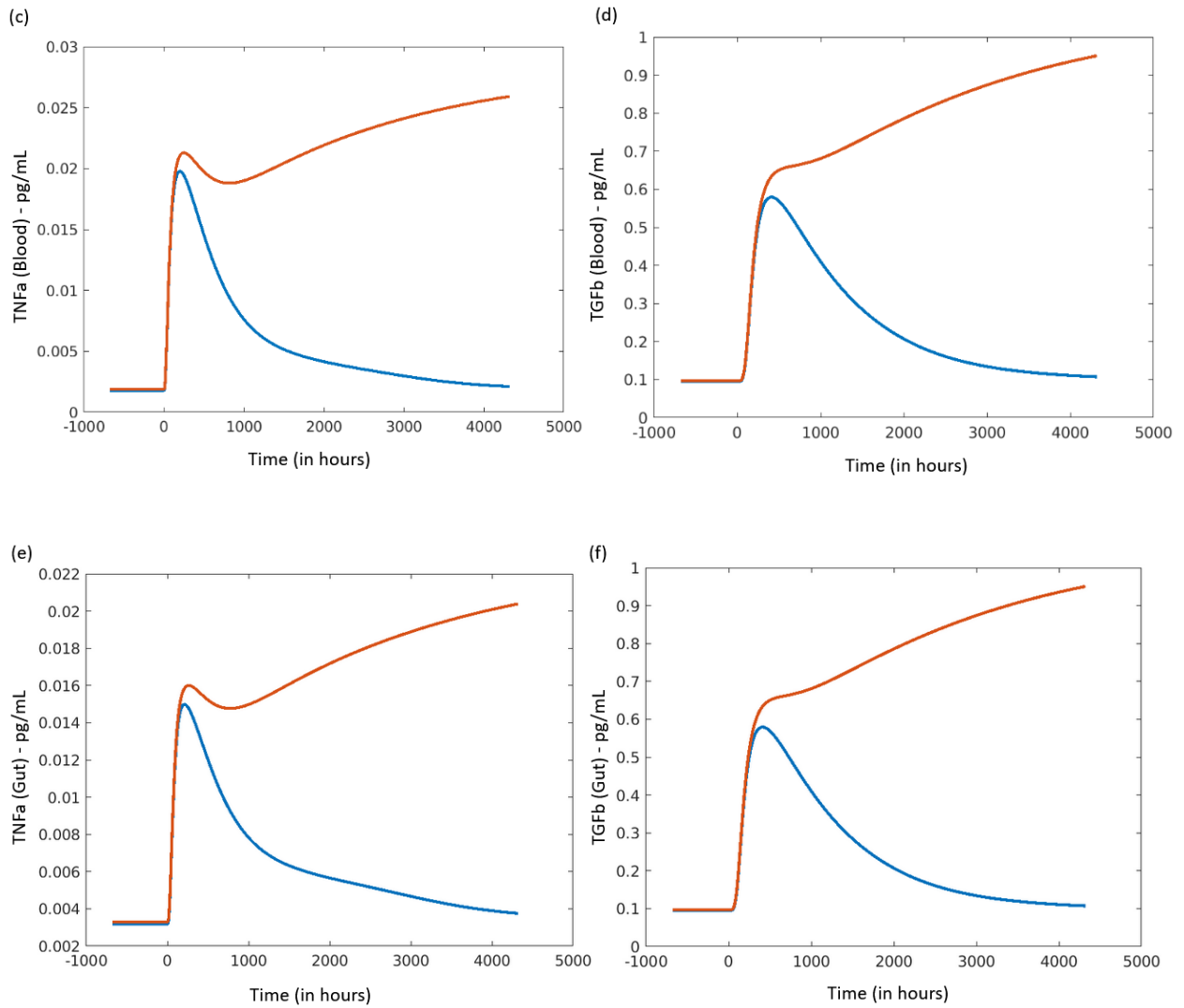
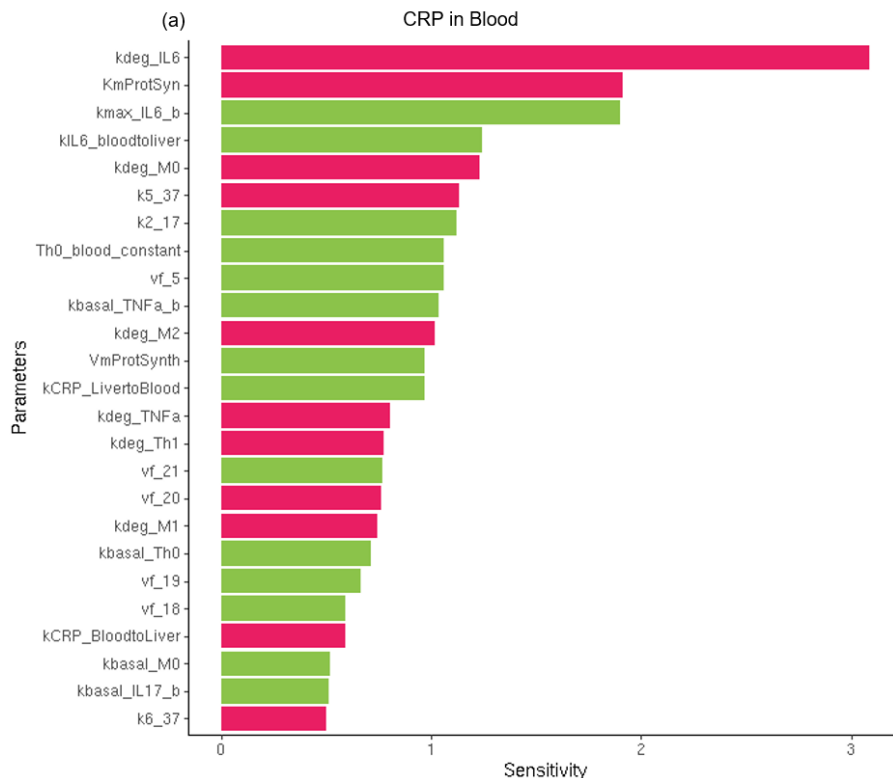


Figure 19: Time Evolution of TNF α and TGF β in different compartments for the normal and radiation sensitive mode of the GLA model upon radiation. The GLA model is simulated for the two modes in the lung compartment, the normal (blue) and the radiation sensitive (red) virtual patient. The radiation event is initiated at time $t = 0$ after the species in the model reaches the steady state. The dynamics of the pro-inflammatory cytokine, TNF α , and anti-inflammatory cytokine, TGF β , in the lung compartment (a and b respectively) are similar to the Lung model, and in the normal mode of the model, the cytokines return back to the original levels, whereas in the sensitive mode of the model, there is chronic inflammation in the system and the virtual patient displays the pathobiology of radiation pneumonitis. The impact of the radiation event is seen for TNF α and TGF β in the blood compartment (c and d respectively) as well as the gut compartment (e and f respectively), indicating the systemic immune modulation happening in the GLA model upon radiation. In the normal virtual patient, the immune dynamics return to the original levels in the blood and the gut compartments, whereas there is a chronic inflammation in the gut compartment for the radiation sensitive virtual patient.

3.3.3. Sensitivity Analysis of the GLA Model

A sensitivity analysis on CRP and SPD was performed against the parameters of the model to identify the key mechanisms and interactions that affect their levels in the blood. Figure 20 shows the top 25 sensitive parameters that affect the steady state values of CRP and SPD levels in the blood. The description of these parameters is listed in Table 16 and Table 17 in Appendix 8. From the figure and the tables, we can conclude that the parameters that affect the CRP levels are related to IL-6, TNF α and IL-17 pathways as well as recruitment and differentiation rates of naïve T cells and macrophages in the gut compartment, which is similar to the conclusions of the sensitivity analysis of CRP in the Gut model (Figure 8). The sensitivity analysis of SPD in the GLA model reveals sensitive parameters that relate to the sensitivity of inflammatory cell death for IL6, IL1b, IFN γ and TNF α pathways, which is also similar to the results obtained from the Lung model (Figure 12). In addition to those parameters, we can also observe gut parameters that relate to the production and degradation of TNF α , IL6 and naïve macrophages and T cells having an impact on the steady state levels of SPD, which is produced in the lung compartment in response to alveolar damage. This implies that specific immune mechanisms in the gut have a crucial effect on the pulmonary alveolar damage-associated pathways.



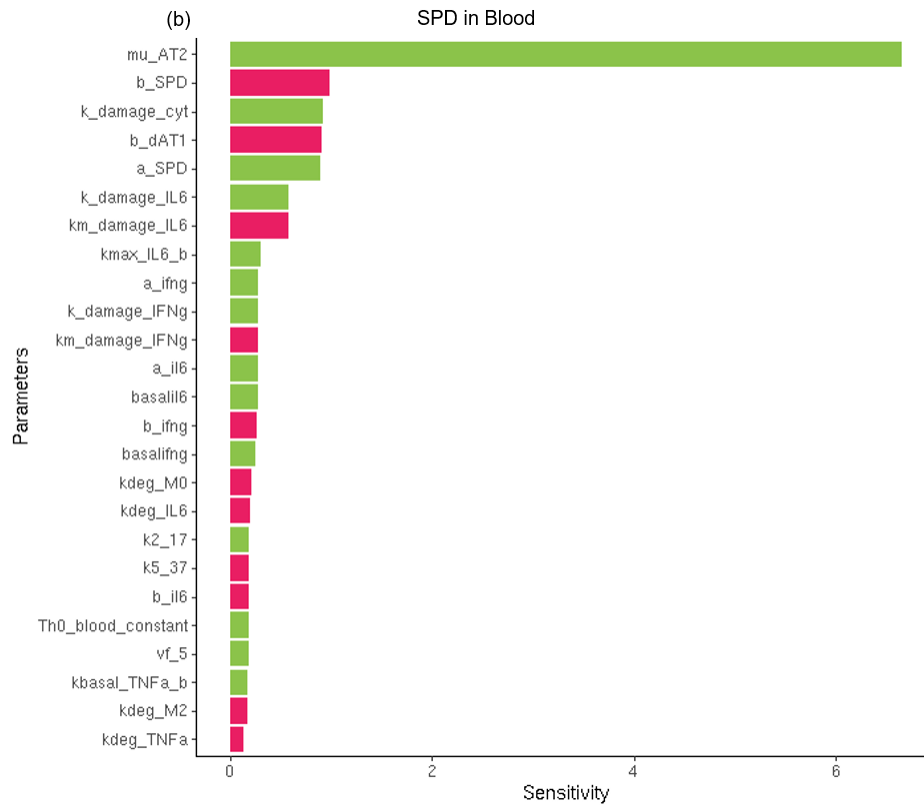


Figure 20: Sensitivity Analysis of CRP and SPD in the GLA model. The sensitivity analysis of Blood CRP (a) mainly indicates sensitive parameters relating to pathways that determine the production, transportation, and degradation of IL6, TNF α and IL17 as well as recruitment, differentiation and degeneration of T cells and macrophages. The sensitivity analysis of Blood SPD (b) relates to parameters that affect the pulmonary alveolar sensitivity to the inflammatory cell death caused by pro-inflammatory cytokines; moreover, additional gut parameters that relate to the production and degradation of TNF α , IL6 and naïve macrophages and T cells in the gut compartment are also reported as sensitive parameters in the analysis, hinting at the indirect effects of immune interactions in the gut on the SPD level in the blood, which is a marker of alveolar damage and primarily produced in the lung compartment as the result of activation of epithelial damage responses. The colours, red and green, indicate that the parameter has a positive or negative sensitive coefficient, respectively.

3.3.4. Simulation of the Sustained Gut Inflammation of the GLA Model

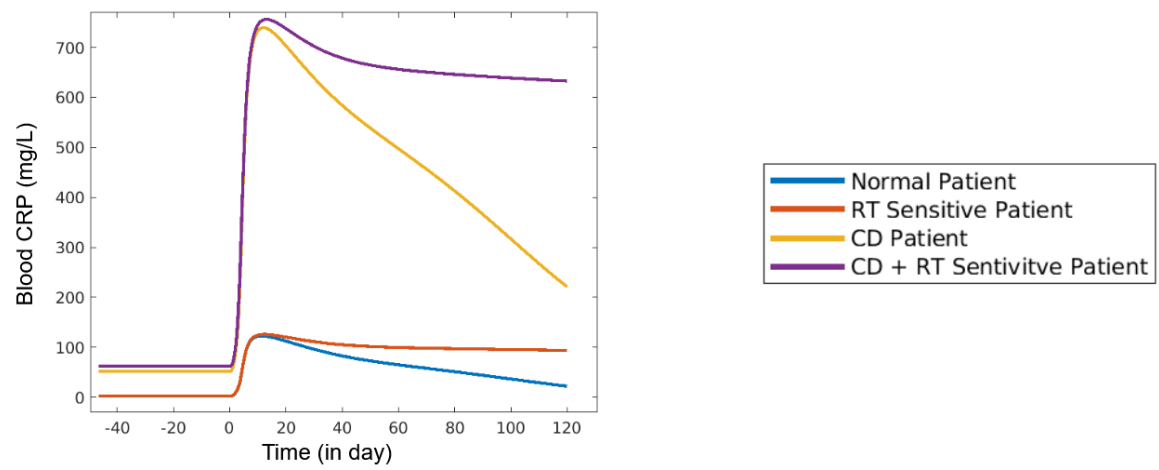
The sensitivity analysis of Blood SPD reveals the indirect effects of gut immune pathways on the damage-associated interactions in the lung compartments. Given that the gut compartment has the flexibility to be simulated in two modes: healthy mode (HV) and sustained gut inflammation (CD or UC mode), we decided to study the impact of sustained gut inflammation on the dynamics of radiation event and subsequent development of pneumonitis in the GLA model.

The GLA model is simulated in four parameter combinations: normal virtual patient (who is not susceptible to developing radiation pneumonitis) and radiation sensitive virtual patient with a normal and healthy gut environment (HV patient), and normal and radiation sensitive virtual patient with a chronically inflamed gut environment (CD patient). The parameters relating to inflammatory cell death that varied between the normal and the radiation sensitive virtual patient are changed by a factor of five for the sensitive patient, which is chosen based on parameter perturbation as seen in Figure 22. The event of radiation is initiated after the model is simulated until all species reach a steady state. The dynamics of species such as biomarkers, immune cells and cytokines in the GLA model under the four modes mentioned above are shown in Figure 21.

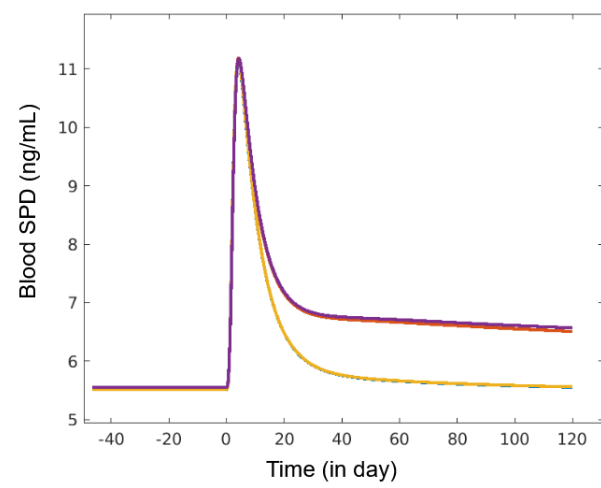
From Figure 21, the virtual patient who has CD, resulting in sustained gut inflammation and develops radiation pneumonitis after radiation (purple) has the highest systemic inflammation (Figure 21 - a) and further increase in inflammation in the gut (Figure 21 – d and e) and lungs (Figure 21 – h to k), even though there is minimal increase in pulmonary damage responses (Figure 21 – b and c) compared to a radiation sensitive patient with healthy gut (red), and potentially increasing the burden of both diseases. The radiation has a high impact on the virtual patient who has CD but is not susceptible to developing radiation pneumonitis (yellow) who initially has increased systemic inflammation (Figure 21 - a) and elevated pro-inflammatory cytokines (Figure 21 – d, f and h) but over time when the damage responses in the lungs become normal (Figure 21 – b and c), these processes come back to normal; essentially this dynamics can be inferred as potentially causing a higher acute burden on gut compared to the same patient before radiation.

Looking from the direction of the gut to lung axis, having a sustained gut inflammation, regardless of whether normal or radiation sensitive patient, increases the inflammatory status of the lungs (Figure 21 - h to k), and this has inter-compartmental effects on the cytokine-associated damage responses (Figure 21 – b and c); however, this inter-compartmental interaction is observed to be small. It is to be noted that since the combined gut-lung axis model is still not parametrised and validated, the rates of transportation of species between compartments may vary, which can potentially affect the strength of these inter-compartmental interactions.

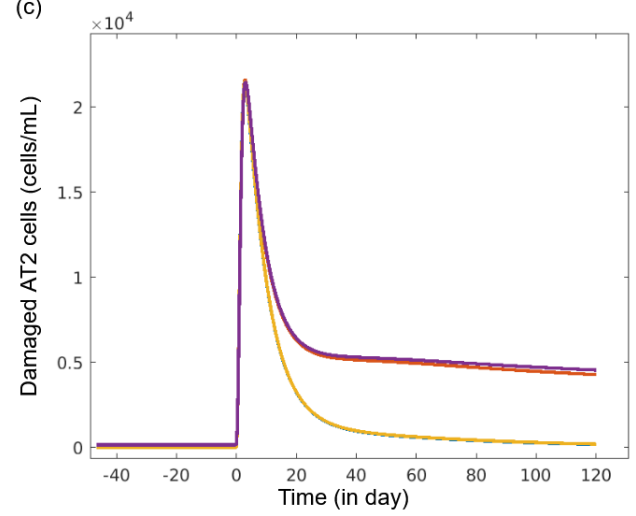
(a)



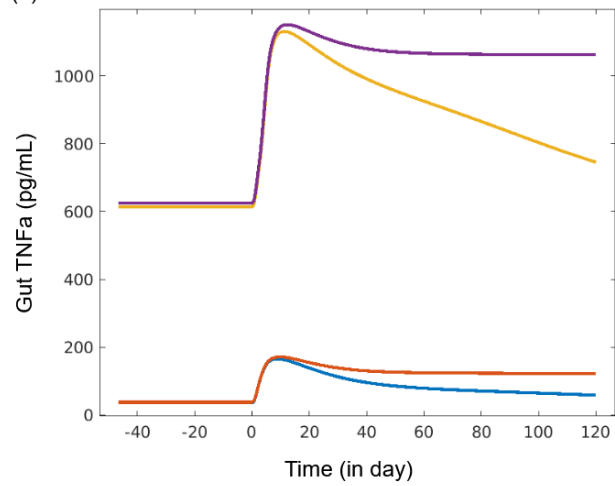
(b)



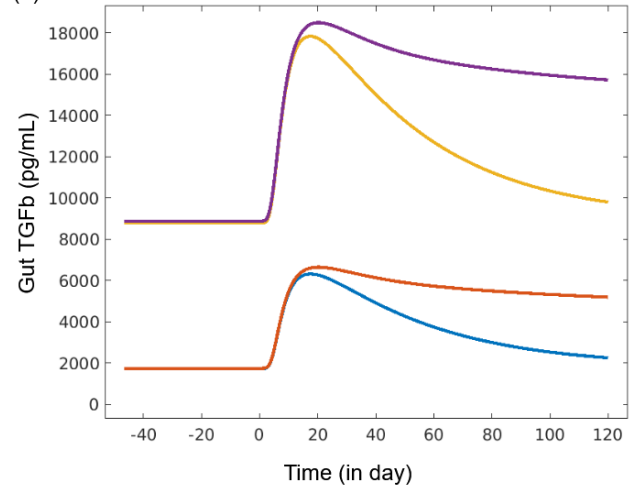
(c)



(d)



(e)



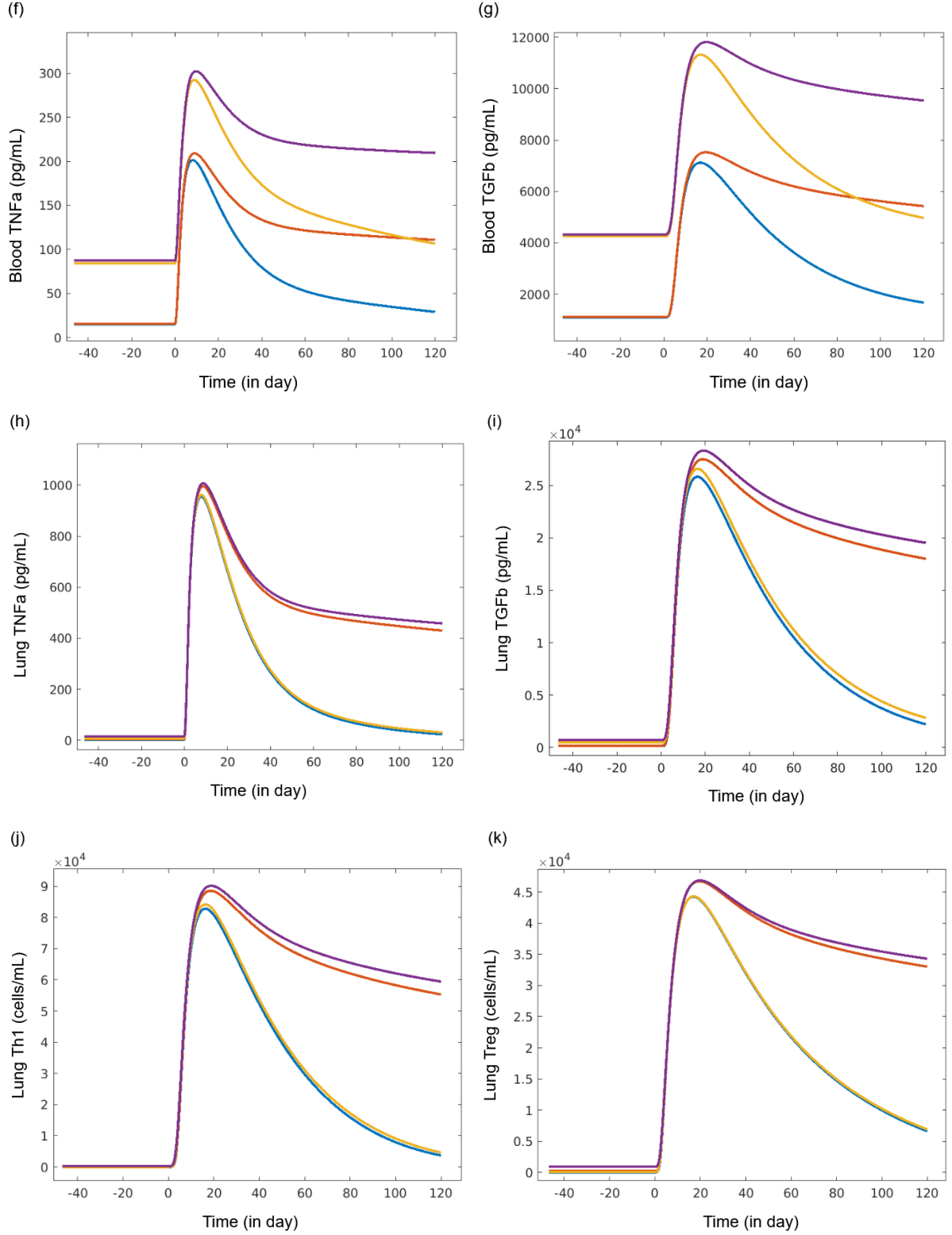


Figure 21: Time Evolution of species in the normal and radiation sensitive mode of the GLA model with normal or sustained gut inflammation upon radiation. The four modes of the GLA model, normal and radiation (RT) sensitive virtual patient with a normal gut environment (red and blue respectively) and with a CD mode which has sustained gut inflammation (yellow and purple respectively), are simulated, and the species dynamics is plotted upon radiation event, which is

introduced at time $t=0$. The CRP in the blood (a) indicates that the CD mode with RT-sensitive patient has the highest systemic inflammation among all the simulation modes, potentially alleviating both diseases. The dynamics of SPD (b) and damaged AT2 cells (c) indicate that their dynamics are primarily dictated by the parameters affecting pulmonary epithelial cytokine-associated damage and inflammatory cell death sensitivity. However, having sustained gut inflammation has a slight yet observable increase in these species values compared to a patient having a normal uninfamed gut. The dynamics of $\text{TNF}\alpha$ and $\text{TGF}\beta$ in the gut compartment (d and e respectively), blood compartment (f and g respectively) and the lung compartment (h and i respectively) show the differential dynamics between these cytokines in different compartments. The differential dynamics also can be observed in immune cell populations, such as Th1 cells (j) and Treg cells (k) in the lung compartment. These results show the two axes of bidirectional communication between the gut and the lungs, with inflammation in the lungs and/or the gut caused due to radiation and CD, respectively, having a consequential inter-compartmental effect. The strength of these effects determines the overall dynamics of immune responses in each compartment, essentially determining the onset and progression of the diseased mode of the virtual patient.

3.3.5. Effect of the Sustained Gut Inflammation on the Sensitivity Factor of Inflammatory Cell Death in Lung

For the normal and the radiation sensitive virtual patient of the GLA model, all parameters except four are kept unchanged between the two modes of the model. The parameters relating to inflammatory cell death (i.e., $k_{\text{damage_IFNg}}$, $k_{\text{damage_IL6}}$, $k_{\text{damage_IL1b}}$ and $k_{\text{damage_TNFa}}$) are changed between the two modes of the models. These four parameters are multiplied by a factor in the radiation sensitive virtual patient. If the factor is 1, it corresponds to the normal virtual patient. The model is simulated by changing this factor, starting from one (corresponding to the normal virtual patient) and incremented by one, and the steady state values for a species (here, in this case, Blood CRP) are calculated and plotted as shown in Figure 22. The model is also simulated using CD virtual patient's parameter values to simulate sustained gut inflammation and the corresponding plot is also generated.

The factor chosen to simulate the model is determined by the maximum value for which the steady-state value of the CRP remains (almost) the same as the steady-state value for the normal virtual patient. The biological reasoning for this criterion is that the radiation sensitive patient, before radiation, should show similar dynamics as the normal patient. Based on this criterion, the factor of 8 is chosen for radiation sensitive patient with healthy uninfamed gut environment and 5 for radiation sensitive patient with sustained gut inflammation (CD). It is to be noted that when the model is

compared to healthy and sustained inflamed gut modes, the lowest of the factors (in this case, five) is chosen for both modes.

From Figure 22, the difference in the maximum value of the sensitivity factor in normal and CD virtual patient indicates that the virtual patient with a sustained inflammation in the gut has a lower tolerance to cytokine-associated damage compared to a normal virtual patient. In other words, the gut inflammation in the CD virtual patient has a systemic effect which propagates to the lung compartment; this propagation influences parameters relating to inflammatory cell death in the lungs which in turn affects the virtual patient's sensitivity to radiation event and its subsequent immune dynamics. This can be biologically interpreted as those patients with chronic gut inflammation (in the case of Ulcerative colitis or Crohn's disease) are much more susceptible to developing radiation-induced pneumonitis in the lungs upon radiation treatment compared to patients with a healthy gut.

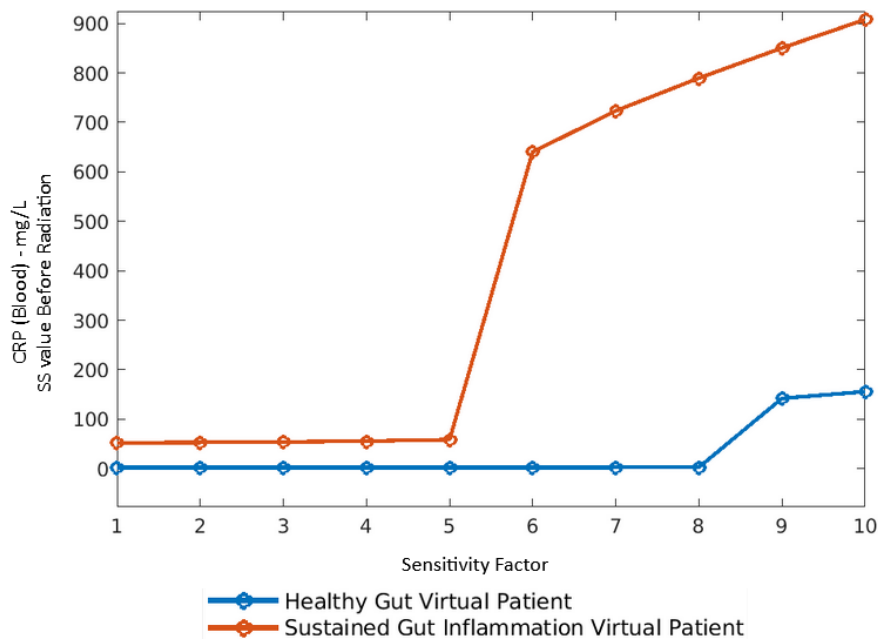


Figure 22: Steady-state value of CRP for different factor values of radiation sensitive virtual patient with healthy and inflamed gut environment. The model is simulated for two modes, normal (HV) gut and inflamed (CD) gut environment, to determine the factor to multiply the four parameters relating to inflammatory cell death for the radiation sensitive virtual patient. The factor is chosen as the maximum value for which the steady-state value of the CRP remains similar to that of the steady-state value of CRP for the normal patient (factor = 1). Based on this criterion, 8 and 5 are the factors chosen to represent the radiation sensitive virtual patient for HV and CD modes of the GLA model respectively.

4. Discussion

The project was commenced with the aim to create a computational QSP model that incorporates detailed mechanisms for immunological interactions along the 'gut-lung axis,' with the intention that the model will potentially enable us to better understand and characterise the dynamics of the systemic biological processes at play, which will allow us to identify potential biomarkers and suggest novel therapeutic approaches to lung cancer. Given the flexibility of building the individual compartments modularly, the gut and the lung compartments were modelled and tested separately, upon which they are combined to form the final Gut-Lung Axis (GLA) model. The combined model also has accounted for the radiation-mediated immune responses, intending to understand how immune interactions in the 'gut-lung axis' can affect the outcome and dynamics of radiation-induced pneumonitis.

The sensitivity analysis was used to identify the major pathways that regulate the dynamics of the model state variables. This analysis primarily identified sensitive parameters that are involved in key biological mechanisms which are compatible with the well-grounded literature knowledge, an instance being the impact of IL6 pathways on CRP levels in blood identified from sensitivity analysis of CRP is known and established in the literature (Eklund, 2009). However, the sensitivity analysis also identifies indirect and/or hidden effects of key mechanisms affecting the dynamics of the species under investigation. For example, the initial sensitivity analysis (Figure 12) revealed that changing certain parameters in the lung compartment led to differential dynamics of immune cells and cytokines upon the event of radiation, thus indicating the existence of crucial parameters resulting in a virtual patient being sensitive to radiation therapy and developing radiation-induced pneumonitis. This analysis gives us preliminary mechanistic insight into the influential mechanisms in the gut and lung compartments on systemic immune homeostasis.

The combined model captures the dynamics of perturbations in the lung (radiation event) and gut (sustained inflammation) and its effects along the 'gut-lung axis.' The GLA model also encapsulates inter-compartmental interactions, where the perturbations in the gut or lung are not entirely isolated within their respective compartments, but get cascaded (or propagated) into the other compartment through systemic interactions at play, which can be observed in Figure 21. We can also see

these inter-compartmental interactions be involved in determining the final steady-state values of the species in the model; for example, the sensitivity analysis of SPD in Figure 20 shows sensitive parameters that relate to specific gut immune processes affecting the levels of SPD in blood, indicating their indirect involvement in damage-associated responses in the alveolar epithelial cells (AT1 and AT2) in the lung compartment.

From understanding the dynamics of the final GLA model under perturbations, we could capture the bidirectional communication channel between the gut and the lung compartment through immunological interactions, which was one of the primary aims in developing the model for the thesis. We could observe that upon radiation and the onset of radiation-induced pneumonitis in the model, there is an increase in systemic inflammation (indicated through CRP dynamics) as well as an increase in pro-inflammatory cytokines and immune cell species in the gut compartment, as seen in Figure 19, which can be inferred as inflammation in the gut compartment caused due to radiation. This immune modulation in the gut can potentially affect the gut microbiome dynamics, such as changes in the composition of microbial species and microbial metabolites resulting in functionality changes of the gut microbiome, which can be investigated with the addition of microbiome interactions in the model in the future. Additionally, changes in microbial metabolites due to functional changes in the gut microbiome can lead to inflammation in the gut, which can have an inter-compartmental effect on the lung compartment, potentially affecting radiation pneumonitis dynamics in the lungs, which can be computationally tested using the model.

We also observed that the inflammation status of the gut compartment could affect the lung immune dynamics upon radiation (Figure 21), and this effect can be further enhanced with the addition of gut microbiota processes. This can also help us test hypotheses such as how modifying the gut microbiome, which increases the resilience of gut immunological processes to inflammatory perturbations by either strengthening anti-inflammatory feedback loops or weakening pro-inflammatory feedback loops, can have a positive effect in maintaining a healthy lung immune homeostasis and potentially reducing the susceptibility to develop radiation pneumonitis upon radiation treatment. This model, upon a thorough parameterisation and validation, will give us a preliminary insight into the potential mechanisms and players that govern the outcome

of radiotherapy, and how these can be exploited to develop new biomarkers to determine the eligibility criteria for radiotherapy and potential gut microbiota therapeutic strategies (such as faecal microbiota transplantation) to improve the outcomes of cancer treatments.

The preliminary model developed has given some mechanistic insights into how the immune processes in the gut and lungs can have an effect on systemic immune homeostasis. This influence at the systemic level can have subsequent effects on the gastrointestinal and pulmonary microbiome, which needs to be investigated. The mechanistic pathways that correspond to the microbiome and its related metabolites need to be included in the model to understand the influence of the microbiome on the 'gut-lung axis.' For example, it is known that pro-inflammatory markers, like IL-1 β , IL-6, and IL-8 in the lungs are stimulated by bile acid (Liu *et al.*, 2020), while microbial short-chain fatty acids (SCFAs) show anti-inflammatory properties by regulating several leukocyte functions, including the production of cytokines, including TNF α , IL-2, IL-6 and IL-10 (Vinolo *et al.*, 2011; Rutting *et al.*, 2019).

To incorporate these mechanisms into the model, we have to include new microbial-associated species and their corresponding pathways in the model. The model will then help us examine how gut microbiota, directly or indirectly through its metabolites and its subsequent effects on the immune components, actively regulates inflammation through its microbial-cytokine regulatory interactions, both locally and systemically. An additional line of investigation is to model gut dysbiosis, which causes damage to the intestinal mucosal barrier, leading to invading gut bacteria and metabolites affecting the host's immune homeostasis locally and systematically. The updated model can be additionally used to understand the dynamics of radiation fibrosis and the effect of the gut microbiota on the pathogenesis of radiation pneumonitis and fibrosis.

In order to fully incorporate the systemic immune interactions associated with the gut microbiome, new compartments, such as bone marrow, needs to be added to the model. For instance, in an attempt to integrate the dynamics of SCFAs in the 'gut-lung axis,' the model needs to account for the increased differentiation of macrophages and DC progenitor cells into Ly6c negative monocytes in the bone marrow in response to SCFA in blood, which in turn differentiate into alternatively activated macrophages

(M2) in the lungs, which has the capacity to reduce inflammation and repair damaged tissue by regulating the effects brought on by infiltrating neutrophils (Trompette *et al.*, 2018). Dysbiosis of gut microbiota leads to weakened anti-inflammatory effects by SCFA, and thus, chronic systemic inflammation can form a microenvironment prone to the occurrence and development of radiation therapy associated complications, including radiation-induced pneumonitis, which can be simulated and tested using the updated model.

The gut compartment of the final GLA model developed during the thesis was qualitatively evaluated (Figure 9), but the model needs to be quantitatively validated and parameterised for all compartments to fit the experimental data from murine samples. The parameters used in the model were parameterised by the authors of the IBD and SARS-Cov-2 models (Dai *et al.*, 2021; Rogers *et al.*, 2021a) using clinical and experimental data from human patients. The data that we will receive from DFG funded GRK2762 project will be from mice samples, which necessitates the reparameterisation of the combined model with murine data. The model will be parameterised and validated based on in-house data from the GRK2762 project as well as from published literature data (Rutting *et al.*, 2019; Flynn *et al.*, 2020).

For this purpose of parameterisation, one of the potential candidates is the Stepwise IIV algorithm (a parameter estimation algorithm) which is an in-built tool available in the IQR Tools package. This algorithm is a brute force method which estimates parameters for complex models with precision based on available data. The advantages of using this algorithm over other parameter estimation tools (such as NONMEM and MONOLIX) are faster convergence to the value through symbolic derivation of sensitivities and swift exploration of global parameter space, which quickens finding estimations to larger scale QSP problems such as ours.

A major limitation in this project is that the results shown in this thesis are generated from a single virtual patient which does not explain the biological heterogeneity seen in the experimental data as a single virtual patient cannot capture the variability and diversity that is present in the real patient population. A single virtual patient may not be representative of the broader population, and may not accurately reflect the range of responses that can be expected in real patients. To overcome this limitation, we can create a “Virtual Population” that captures the heterogeneity seen in the patient

population. Parameter sweeping methods (such as Latin hypercube sampling and Monte Carlo simulations) enables generating a plausible population to fit physiological values of cell population numbers and cytokines levels (Allen *et al.*, 2016). This can be done by exporting each individual parameter estimate from experimental data as 'Virtual Subjects'. From this, we can also generate a virtual patient population by sampling from the estimated population distributions. After generating a virtual patient population, we can simulate the model from this virtual population which can help in addressing concerns with the biological variability seen in the experimental data.

Moreover, there is a need to check the global robustness of the model through parameter sensitivity analysis. By contrasting the simulation results from the model with the experimental levels observed in the patient population, the applicability and robustness of the model need to be assessed. The validated model can potentially be used for testing biological hypotheses and suggesting predictive biomarkers. The same approach can potentially be applied to identify novel treatment strategies and combination therapies through virtual clinical trials. This can help to modulate knowledge from basic sciences into translational approaches, which can be tested in clinical settings, saving costs regarding time, resources, and animal lives.

5. Bibliography

- Aghamiri, SS, Amin, R, and Helikar, T (2021). Recent applications of quantitative systems pharmacology and machine learning models across diseases. *Journal of Pharmacokinetics and Pharmacodynamics* 2021 49:1 49, 19–37.
- Allen, RJ, Rieger, TR, and Musante, CJ (2016). Efficient Generation and Selection of Virtual Populations in Quantitative Systems Pharmacology Models. *CPT Pharmacometrics Syst Pharmacol* 5, 140–146.
- Baumann, M, Krause, M, Overgaard, J, Debus, J, Bentzen, SM, Daartz, J, Richter, C, Zips, D, and Bortfeld, T (2016). Radiation oncology in the era of precision medicine. *Nat Rev Cancer* 16, 234–249.
- Bercovici, N, Guérin, M V., Trautmann, A, and Donnadieu, E (2019). The remarkable plasticity of macrophages: A chance to fight cancer. *Front Immunol* 10, 1563.
- Biasi, F, Leonarduzzi, G, Oteiza, PI, and Poli, G (2013). Inflammatory Bowel Disease: Mechanisms, Redox Considerations, and Therapeutic Targets. <https://HomeLiebertpubCom/Ars> 19, 1711–1747.
- Budden, KF, Gellatly, SL, Wood, DLA, Cooper, MA, Morrison, M, Hugenholtz, P, and Hansbro, PM (2016). Emerging pathogenic links between microbiota and the gut–lung axis. *Nature Reviews Microbiology* 2016 15:1 15, 55–63.
- Capelozzi, VL et al. (2017). Molecular and Immune Biomarkers in Acute Respiratory Distress Syndrome: A Perspective From Members of the Pulmonary Pathology Society. *Arch Pathol Lab Med* 141, 1719–1727.
- Dai, W, Rao, R, Sher, A, Tania, N, Musante, CJ, and Allen, R (2021). A Prototype QSP Model of the Immune Response to SARS-CoV-2 for Community Development. *CPT Pharmacometrics Syst Pharmacol* 10, 18–29.
- Eftimie, R, Gillard, JJ, and Cantrell, DA (2016). Mathematical Models for Immunology: Current State of the Art and Future Research Directions. *Bull Math Biol* 78, 2091–2134.
- Eklund, CM (2009). Proinflammatory cytokines in CRP baseline regulation. *Adv Clin Chem* 48, 111–136.
- Erbayrak, M, Turkay, C, Eraslan, E, Cetinkaya, H, Kasapoglu, B, and Bektas, M (2009). The Role of Fecal Calprotectin in Investigating Inflammatory Bowel Diseases. *Clinics (Sao Paulo)* 64, 421.
- Ermakov, S, Schmidt, BJ, Musante, CJ, and Thalhauser, CJ (2019). A Survey of Software Tool Utilization and Capabilities for Quantitative Systems Pharmacology:

What We Have and What We Need. *CPT Pharmacometrics Syst Pharmacol* 8, 62–76.

Fabbiano, S et al. (2018). Functional Gut Microbiota Remodeling Contributes to the Caloric Restriction-Induced Metabolic Improvements. *Cell Metab* 28, 907-921.e7.

Fagan, EA, Dyck, RF, Maton, PN, Hodgson, HJF, Chadwick, VS, Petrie, A, and Pepys, MB (1982). Serum levels of C-reactive protein in Crohn's disease and ulcerative colitis. *Eur J Clin Invest* 12, 351–359.

Flynn, S, Reen, FJ, Caparrós-Martín, JA, Woods, DF, Peplies, J, Ranganathan, SC, Stick, SM, and O'gara, F (2020). Bile Acid Signal Molecules Associate Temporally with Respiratory Inflammation and Microbiome Signatures in Clinically Stable Cystic Fibrosis Patients. *Microorganisms* 8, 1–17.

Gallacher, DJ, and Kotecha, S (2016). Respiratory Microbiome of New-Born Infants. *Front Pediatr* 4, 1.

Geginat, J, Paroni, M, Maglie, S, Alfen, JS, Kastirr, I, Gruarin, P, de Simone, M, Pagani, M, and Abrignani, S (2014). Plasticity of human CD4 T cell subsets. *Front Immunol* 5, 630.

Gerassy-Vainberg, S et al. (2017). Radiation induces proinflammatory dysbiosis: transmission of inflammatory susceptibility by host cytokine induction. *Gut* 67, 97–107.

Glassner, KL, Abraham, BP, and Quigley, EMM (2020). The microbiome and inflammatory bowel disease. *Journal of Allergy and Clinical Immunology* 145, 16–27.

Gopalakrishnan, V, Helmink, BA, Spencer, CN, Reuben, A, and Wargo, JA (2018). The influence of the gut microbiome on cancer, immunity, and cancer immunotherapy. *Cancer Cell* 33, 570.

Graves, PR, Siddiqui, F, Anscher, MS, and Movsas, B (2010). Radiation pulmonary toxicity: from mechanisms to management. *Semin Radiat Oncol* 20, 201–207.

Helmlinger, G et al. (2019a). Quantitative Systems Pharmacology: An Exemplar Model-Building Workflow With Applications in Cardiovascular, Metabolic, and Oncology Drug Development. *CPT Pharmacometrics Syst Pharmacol* 8, 380–395.

Helmlinger, G et al. (2019b). Quantitative Systems Pharmacology: An Exemplar Model-Building Workflow With Applications in Cardiovascular, Metabolic, and Oncology Drug Development. *CPT Pharmacometrics Syst Pharmacol* 8, 380.

Herbst, RS, Morgensztern, D, and Boshoff, C (2018). The biology and management of non-small cell lung cancer. *Nature* 553, 446–454.

- Hoops, S, Hontecillas, R, Abedi, V, Leber, A, Philipson, C, Carbo, A, and Bassaganya-Riera, J (2016). Ordinary Differential Equations (ODEs) Based Modeling. *Computational Immunology: Models and Tools*, 63–78.
- Indaram, AVK, Visvalingam, V, Locke, M, and Bank, S (2000). Mucosal cytokine production in radiation-induced proctosigmoiditis compared with inflammatory bowel disease. *Am J Gastroenterol* 95, 1221–1225.
- IntiQuan GmbH (2022). IQR Tools: Supporting Model Informed Drug Development with R. Available at: <https://iqrtools.intiquan.com/>. Accessed April 25, 2023.
- Jafarnejad, M, Gong, C, Gabrielson, E, Bartelink, IH, Vicini, P, Wang, B, Narwal, R, Roskos, L, and Popel, AS (2019). A Computational Model of Neoadjuvant PD-1 Inhibition in Non-Small Cell Lung Cancer. *AAPS J* 21.
- Jarzebska, N, Karetnikova, ES, Markov, AG, Kasper, M, Rodionov, RN, and Spieth, PM (2021). Scarred Lung. An Update on Radiation-Induced Pulmonary Fibrosis. *Front Med (Lausanne)* 7, 1100.
- De Jong, M, and Maina, T (2010). Of mice and humans: are they the same?-- Implications in cancer translational research. *J Nucl Med* 51, 501–504.
- Keely, S, Talley, NJ, and Hansbro, PM (2012). Pulmonary-intestinal cross-talk in mucosal inflammatory disease. *Mucosal Immunol* 5, 7–18.
- Kehrmann, J et al. (2019). Gut Microbiota in Human Immunodeficiency Virus–Infected Individuals Linked to Coronary Heart Disease. *J Infect Dis* 219, 497–508.
- Knight-Schrijver, VR, Chelliah, V, Cucurull-Sanchez, L, and Le Novère, N (2016). The promises of quantitative systems pharmacology modelling for drug development. *Comput Struct Biotechnol J* 14, 363–370.
- Leil, TA, and Bertz, R (2014). Quantitative systems pharmacology can reduce attrition and improve productivity in pharmaceutical research and development. *Front Pharmacol* 5, 247.
- Leil, TA, and Ermakov, S (2015). Editorial: The emerging discipline of quantitative systems pharmacology. *Front Pharmacol* 6, 129.
- Liu, NN, Ma, Q, Ge, Y, Yi, CX, Wei, LQ, Tan, JC, Chu, Q, Li, JQ, Zhang, P, and Wang, H (2020). Microbiome dysbiosis in lung cancer: from composition to therapy. *Npj Precision Oncology* 2020 4:1 4, 1–12.
- Liu, X et al. (2021). The Role of Gut Microbiota in Lung Cancer: From Carcinogenesis to Immunotherapy. *Front Oncol* 11, 3118.

- Lv, Y, Qin, X, Jia, H, Chen, S, Sun, W, and Wang, X (2019). The association between gut microbiota composition and BMI in Chinese male college students, as analysed by next-generation sequencing. *British Journal of Nutrition* 122, 986–995.
- Martins, D, Mendes, F, and Schmitt, F (2021). Microbiome: A Supportive or a Leading Actor in Lung Cancer? *Pathobiology* 88, 198–207.
- Metzcar, J, Wang, Y, Heiland, R, and Macklin, P (2019). A Review of Cell-Based Computational Modeling in Cancer Biology. *JCO Clin Cancer Inform* 3, 1–13.
- Moniuszko, A, Wiśniewska, A, and Rydzewska, G (2013). Biomarkers in management of inflammatory bowel disease. *Prz Gastroenterol* 8, 275.
- Niarakis, A, and Helikar, T (2021). A practical guide to mechanistic systems modeling in biology using a logic-based approach. *Brief Bioinform* 22.
- Peterson, MC, and Riggs, MM (2015). FDA Advisory Meeting Clinical Pharmacology Review Utilizes a Quantitative Systems Pharmacology (QSP) Model: A Watershed Moment? *CPT Pharmacometrics Syst Pharmacol* 4, 189–192.
- Reinold, J et al. (2021). A Pro-Inflammatory Gut Microbiome Characterizes SARS-CoV-2 Infected Patients and a Reduction in the Connectivity of an Anti-Inflammatory Bacterial Network Associates With Severe COVID-19. *Front Cell Infect Microbiol* 11, 1154.
- Reinold, J et al. (2022). The Fungal Gut Microbiome Exhibits Reduced Diversity and Increased Relative Abundance of Ascomycota in Severe COVID-19 Illness and Distinct Interconnected Communities in SARS-CoV-2 Positive Patients. *Front Cell Infect Microbiol* 12, 466.
- Rogers, GB, Keating, DJ, Young, RL, Wong, ML, Licinio, J, and Wesselingh, S (2016). From gut dysbiosis to altered brain function and mental illness: mechanisms and pathways. *Molecular Psychiatry* 21:6 21, 738–748.
- Rogers, K V., Martin, SW, Bhattacharya, I, Singh, RSP, and Nayak, S (2021a). A Dynamic Quantitative Systems Pharmacology Model of Inflammatory Bowel Disease: Part 1 – Model Framework. *Clin Transl Sci* 14, 239–248.
- Rogers, K V., Martin, SW, Bhattacharya, I, Singh, RSP, and Nayak, S (2021b). A Dynamic Quantitative Systems Pharmacology Model of Inflammatory Bowel Disease: Part 2 – Application to Current Therapies in Crohn’s Disease. *Clin Transl Sci* 14, 249–259.
- Rooks, MG, and Garrett, WS (2016). Gut microbiota, metabolites and host immunity. *Nature Reviews Immunology* 16:6 16, 341–352.

- Rutsch, A, Kantsjö, JB, and Ronchi, F (2020). The Gut-Brain Axis: How Microbiota and Host Inflammasome Influence Brain Physiology and Pathology. *Front Immunol* 11, 3237.
- Rutten, EPA, Lenaerts, K, Buurman, WA, and Wouters, EFM (2014). Disturbed Intestinal Integrity in Patients With COPD. *Chest* 145, 245–252.
- Rutting, S, Xenaki, D, Malouf, M, Horvat, JC, Wood, LG, Hansbro, PM, and Oliver, BG (2019). Short-chain fatty acids increase TNF α -induced inflammation in primary human lung mesenchymal cells through the activation of p38 MAPK. *Am J Physiol Lung Cell Mol Physiol* 316, L157–L174.
- Saltelli, A, Ratto, M, Andres, T, Campolongo, F, Cariboni, J, Gatelli, D, Saisana, M, and Tarantola, S (2007). *Global Sensitivity Analysis. The Primer*, Wiley.
- Sancho-Araiz, A, Mangas-Sanjuan, V, and Trocóniz, IF (2021). The Role of Mathematical Models in Immuno-Oncology: Challenges and Future Perspectives. *Pharmaceutics* 13.
- Schaue, D, Micewicz, ED, Ratikan, JA, Xie, MW, Cheng, G, and McBride, WH (2015). Radiation and Inflammation. *Semin Radiat Oncol* 25, 4–10.
- Schluter, J et al. (2020). The gut microbiota is associated with immune cell dynamics in humans. *Nature* 2020 588:7837 588, 303–307.
- Sher, A, Niederer, SA, Mirams, GR, Kirpichnikova, A, Allen, R, Pathmanathan, P, Gavaghan, DJ, van der Graaf, PH, and Noble, D (2022). A Quantitative Systems Pharmacology Perspective on the Importance of Parameter Identifiability. *Bull Math Biol* 84, 39.
- Śliwińska-Mossoń, M, Wadowska, K, Trembecki, Ł, and Bil-Lula, I (2020). Markers Useful in Monitoring Radiation-Induced Lung Injury in Lung Cancer Patients: A Review. *J Pers Med* 10, 1–16.
- Sorger, PK et al. (2011). Quantitative and Systems Pharmacology in the Post-genomic Era: New Approaches to Discovering Drugs and Understanding Therapeutic Mechanisms Author Affiliations. In: *QSP Workshop Group White Paper Vol. 48* (National Institutes of Health, Bethesda, MD).
- Sové, RJ, Jafarnejad, M, Zhao, C, Wang, H, Ma, H, and Popel, AS (2020). QSP-IO: A Quantitative Systems Pharmacology Toolbox for Mechanistic Multiscale Modeling for Immuno-Oncology Applications. *CPT Pharmacometrics Syst Pharmacol* 9, 484–497.
- Stein, AM, and Looby, M (2018). Benchmarking QSP Models Against Simple Models: A Path to Improved Comprehension and Predictive Performance. *CPT Pharmacometrics Syst Pharmacol* 7, 487.

- Sung, H, Ferlay, J, Siegel, RL, Laversanne, M, Soerjomataram, I, Jemal, A, and Bray, F (2021). Global Cancer Statistics 2020: GLOBOCAN Estimates of Incidence and Mortality Worldwide for 36 Cancers in 185 Countries. *CA Cancer J Clin* 71, 209–249.
- Thai, AA, Solomon, BJ, Sequist, L V., Gainor, JF, and Heist, RS (2021). Lung cancer. *The Lancet* 398, 535–554.
- Trompette, A, Gollwitzer, ES, Pattaroni, C, Lopez-Mejia, IC, Riva, E, Pernot, J, Ubags, N, Fajas, L, Nicod, LP, and Marsland, BJ (2018). Dietary Fiber Confers Protection against Flu by Shaping Ly6c- Patrolling Monocyte Hematopoiesis and CD8+ T Cell Metabolism. *Immunity* 48, 992-1005.e8.
- Tyldesley, S, Boyd, C, Schulze, K, Math, M, Walker, H, and Mackillop, WJ (2001). Estimating the need for radiotherapy for lung cancer: an evidence-based, epidemiologic approach. *Int J Radiat Oncol Biol Phys* 49, 973–985.
- Uribe-Herranz, M et al. (2020). Gut microbiota modulate dendritic cell antigen presentation and radiotherapy-induced antitumor immune response. *J Clin Invest* 130, 466–479.
- Valdes, AM, Walter, J, Segal, E, and Spector, TD (2018). Role of the gut microbiota in nutrition and health. *BMJ* 361, 36–44.
- Valentinuzzi, D, and Jeraj, R (2020). Computational modelling of modern cancer immunotherapy. *Phys Med Biol* 65.
- Vinolo, MAR, Rodrigues, HG, Nachbar, RT, and Curi, R (2011). Regulation of Inflammation by Short Chain Fatty Acids. *Nutrients* 3, 858.
- Visser, SAG, De Alwis, DP, Kerbusch, T, Stone, JA, and Allerheiligen, SRB (2014). Implementation of Quantitative and Systems Pharmacology in Large Pharma. *CPT Pharmacometrics Syst Pharmacol* 3, 1–10.
- Wang, H, Milberg, O, Bartelink, IH, Vicini, P, Wang, B, Narwal, R, Roskos, L, Santa-Maria, CA, and Popel, AS (2019). In silico simulation of a clinical trial with anti-CTLA-4 and anti-PD-L1 immunotherapies in metastatic breast cancer using a systems pharmacology model. *R Soc Open Sci* 6.
- Wéra, O, Lancellotti, P, and Oury, C (2016). The Dual Role of Neutrophils in Inflammatory Bowel Diseases. *J Clin Med* 5.
- Wirsdörfer, F, and Jendrossek, V (2016). The Role of Lymphocytes in Radiotherapy-Induced Adverse Late Effects in the Lung. *Front Immunol* 7.
- Wong, SH, and Yu, J (2019). Gut microbiota in colorectal cancer: mechanisms of action and clinical applications. *Nature Reviews Gastroenterology & Hepatology* 2019 16:11 16, 690–704.

Zhang, S, Cai, Y, Meng, C, Ding, X, Huang, J, Luo, X, Cao, Y, Gao, F, and Zou, M (2021). The role of the microbiome in diabetes mellitus. *Diabetes Res Clin Pract* 172, 108645.

Zheng, Y et al. (2020). Specific gut microbiome signature predicts the early-stage lung cancer. *Gut Microbes* 11, 1030–1042.

Zhuang, H et al. (2019). Dysbiosis of the gut microbiome in lung cancer. *Front Cell Infect Microbiol* 9, 112.

(1997). A Survey of Models for Tumor-Immune System Dynamics.

(2023). Spectral Viewer. Beckman Coulter Inc. Available at: https://www.beckman.de/en/flow-cytometry/fluorescence-spectrum-analyzer?_ga=2.128571020.1415262954.1680210005-1899072458.1680210003. Accessed March 31, 2023.

6. Appendix

6.1. Appendix 1: List of State Variables and Parameters for ‘Gut-Lung Axis’ Model

Table 7 and Table 8 contains the list of state variables (species) and parameters in the final ‘Gut-Lung Axis’ model respectively.

Species	Description	Compartment	Units
Gut_Th0	Naïve T helper cells	Gut	cells
Gut_Th1	T helper 1 cells	Gut	cells
Gut_Th2	T helper 2 cells	Gut	cells
Gut_Th17	T helper 17 cells	Gut	cells
Gut_Treg	T regulatory cells	Gut	cells
Gut_IL4	Interleukin 4	Gut	picomole
Gut_IL10	Interleukin 10	Gut	picomole
Gut_TGFb	Transforming growth factor beta 1	Gut	picomole
Gut_M1	Classically activated macrophages	Gut	cells
Gut_eDC	Effector dendritic cells	Gut	cells
Gut_IL12	Interleukin 12	Gut	picomole
Gut_IFNg	Interferon gamma	Gut	picomole
Gut_TL1A	TNF like ligand A	Gut	picomole
Gut_IL2	Interleukin 2	Gut	picomole
Gut_IL21	Interleukin 21	Gut	picomole
Gut_IL23	Interleukin 23	Gut	picomole
Gut_IL6	Interleukin 6	Gut	picomole
Gut_IL17	Interleukin 17	Gut	picomole
Gut_tDC	Tolerogenic dendritic cells	Gut	cells
Gut_M2	Alternatively activated macrophages	Gut	cells
Gut_M0	Resting macrophages	Gut	cells
Gut_GMCSF	Granulocyte-macrophage colony-stimulating factor	Gut	picomole
Gut_TNFa	Tumour Necrosis Factor alpha	Gut	picomole
Gut_IL13	Interleukin 13	Gut	picomole
Gut_iDC	Immature dendritic cells	Gut	cells
Gut_NK1	Natural Killer 1 cells	Gut	cells
Gut_NKT	Natural Killer T cells	Gut	cells
Gut_IL5	Interleukin 5	Gut	picomole
Gut_IL15	Interleukin 15	Gut	picomole
Gut_IL18	Interleukin 18	Gut	picomole
Gut_NK	Natural Killer cells	Gut	cells
Gut_NK2	Natural Killer 2 cells	Gut	cells
Gut_IL22	Interleukin 22	Gut	picomole
Gut_Neu	Neutrophils	Gut	cells
Gut_IL8	Interleukin 8	Gut	picomole
Gut_Neu_act	Activated neutrophils	Gut	cells
Blood_IL6	Interleukin 6	Blood	picomole
Blood_CRP	C-Reactive Protein	Blood	picomole

Blood_Neu	Neutrophils	Blood	picomole
Blood_IL8	Interleukin 8	Blood	picomole
Blood_IL17	Interleukin 17	Blood	picomole
Blood_IL12	Interleukin 12	Blood	picomole
Blood_TGFb	Transforming growth factor beta 1	Blood	picomole
Blood_TNFa	Tumour Necrosis Factor alpha	Blood	picomole
Blood_IL1b	Interleukin 1 beta	Blood	picomole
Blood_IFNb	Interferon beta	Blood	picomole
Blood_IFNg	Interferon gamma	Blood	picomole
Blood_IL2	Interleukin 2	Blood	picomole
Blood_IL10	Interleukin 10	Blood	picomole
Blood_GMCSF	Granulocyte-macrophage colony-stimulating factor	Blood	picomole
Liver_IL6	Interleukin 6	Liver	picomole
Liver_CRPE	C-Reactive Protein Extracellular	Liver	picomole
Extracellular V	Damage-associated molecular patterns	Lungs	molecules
AT1	Pulmonary alveolar type I cells	Lungs	cells
AT2	Pulmonary alveolar type II cells	Lungs	cells
I	Irradiated cells	Lungs	cells
dAT1	Damaged AT1 cells	Lungs	cells
dAT2	Damaged AT2 cells	Lungs	cells
pDC	Pulmonary dendritic cells	Lungs	cells
M1	Classically activated macrophages	Lungs	cells
N	Neutrophils	Lungs	cells
Th1	T helper 1 cells	Lungs	cells
Th17	T helper 17 cells	Lungs	cells
CTL	Cytotoxic T cells	Lungs	cells
Treg	T regulatory cells	Lungs	cells
TNFa	Tumour Necrosis Factor alpha	Lungs	picomole
IL6	Interleukin 6	Lungs	picomole
IL1b	Interleukin 1 beta	Lungs	picomole
IFNb	Interferon beta	Lungs	picomole
IFNg	Interferon gamma	Lungs	picomole
IL2	Interleukin 2	Lungs	picomole
IL12	Interleukin 12	Lungs	picomole
IL17	Interleukin 17	Lungs	picomole
IL10	Interleukin 10	Lungs	picomole
TGFb	Transforming growth factor beta 1	Lungs	picomole
GMCSF	Granulocyte-macrophage colony-stimulating factor	Lungs	picomole
SPD	Surfactant protein D	Lungs	picomole

Table 7: List of all state variables (species) in the GLA model

Parameter	Description	Value
k1_1	Adjustment, IL4 on Th0 to Th1 differentiation	0.0353
k2_1	Adjustment, IL10 on Th0 to Th1 differentiation	0.062
k3_1	Adjustment, TGFb on Th0 to Th1 differentiation	0.0011
k4_1	Half-sat, IL12 on Th0 to Th1 differentiation	0.000249
k5_1	Half-sat, IFNg on Th0 to Th1 differentiation	0.0154
k6_1	Half-sat, TL1A on Th0 to Th1 differentiation	0.227
kbasal_1	Basal Th0 to Th1 differentiation rate	0.123
vf_1	Rate of Th0 to Th1 differentiation	0.222
k1_2	Adjustment, IFNg on Th0 to Th2 differentiation	0.0734
k2_2	Adjustment, IL10 on Th0 to Th2 differentiation	0.0445
k3_2	Adjustment, TGFb on Th0 to Th2 differentiation	0.005373
k4_2	Half-sat, IL4 on Th0 to Th2 differentiation	0.0001169
kbasal_2	Basal Th0 to Th2 differentiation rate	0.0212
vf_2	Rate of Th0 to Th2 differentiation	0.217
k1_3	Adjustment, IL4 on Th0 to Th17 differentiation	0.0085
k2_3	Adjustment, IL2 on Th0 to Th17 differentiation	0.0086
k3_3	Adjustment, IFNg on Th0 to Th17 differentiation	0.00885
k4_3	Half-sat, IL6 on Th0 to Th17 differentiation	0.0007
k5_3	Half-sat, TGFb on Th0 to Th17 differentiation	0.316653
k6_3	Half-sat, TL1A on Th0 to Th17 differentiation	0.342739
k7_3	Half-sat, IL23 on Th0 to Th17 differentiation	0.000695
k8_3	Half-sat, IL21 on Th0 to Th17 differentiation	0.0373
kbasal_3	BasalTh0 to Th17 differentiation rate	0.016
vf_3	Rate of Th0 to Th17 differentiation	0.173
k1_4	Adjustment, IL17 on Th0 to Treg differentiation	0.123
k2_4	Adjustment, IL23 on Th0 to Treg differentiation	0.107
k3_4	Adjustment, IL6 on Th0 to Treg differentiation	0.113
k4_4	Half-sat, IL2 on Th0 to Treg differentiation	0.0000297
k5_4	Half-sat, TGFb on Th0 to Treg differentiation	0.016
k6_4	Half-sat, tDC on Th0 to Treg differentiation	45603
kbasal_4	Basal Th0 to Treg differentiation rate	0.07
vf_4	Rate of Th0 to Treg differentiation	0.2
k1_5	Half-sat, eDC on Th0 Transport rate to gut	12365
kbasal_Th0	Basal production rate of Th0	1.21
vf_5	Rate of Th0 Production	0.56
kdeg_Th0	Degradation rate of Th0	0.4711
kdeg_Th1	Degradation rate of Th1	0.315
kdeg_Th2	Degradation rate of Th2	0.2695
kdeg_Th17	Degradation rate of Th17	0.5187
kdeg_Treg	Degradation rate of Treg	0.355
k1_11	Half-sat, Treg on Th17 to Treg differentiation	82697
k2_11	Half-sat, tDC on Th17 to Treg differentiation	129996
k3_11	Half-sat, M2 on Th17 to Treg differentiation	84770
kbasal_11	Basal rate of Th17 to Treg differentiation	0.1
vf_11	Rate of Th17 to Treg differentiation	0.11
k2_12	Half-sat, eDC on Treg to Th17 differentiation	120674
k3_12	Half-sat, M1 on Treg to Th17 differentiation	107612
k4_12	Half-sat, Th1 on Treg to Th17 differentiation	103804
kbasal_12	Basal rate of Treg to Th17 differentiation	0.1

vf_12	Rate of Treg to Th17 differentiation	0.08
k1_12	Half-sat, Th17 on Treg to Th17 differentiation	112162
k1_17	Recruitment of M0 induced by eDC	0.325
k2_17	Recruitment of M0 induced by activated Macrophages	0.325
kbasal_M0	Basal recruitment of M0	2500
k1_18	Half-sat, eDC on M0 to M1 activation	99088
k2_18	Half-sat, Th1 on M0 to M1 activation	511349
kbasal_18	Basal activation of M0 to M1	0.01
vf_18	Rate of activation of M0 to M1	0.01
k3_18	Half-sat, Th17 on M0 to M1 activation	154009
k4_18	Half-sat, TNFa on M0 to M1 activation	0.05292
k5_18	Half-sat, IFNg on M0 to M1 activation	0.02646
k6_18	Half-sat, GMCSF on M0 to M1 activation	0.00938
k1_19	Half-sat, tDC on M0 to M2 activation	159088
k2_19	Half-sat, Treg on M0 to M2 activation	231319
k3_19	Half-sat, IL4 on M0 to M2 activation	0.00245
k4_19	Half-sat, IL13 on M0 to M2 activation	0.002549
k5_19	Half-sat, IL10 on M0 to M2 activation	0.0017
k6_19	Half-sat, TGFb on M0 to M2 activation	0.21
kbasal_19	Basal activation of M0 to M2	0.007
vf_19	Rate of activation of M0 to M2	0.009
k1_20	Half-sat, tDC on M1 to M2 activation	109023
k2_20	Half-sat, Treg on M1 to M2 activation	69961
k3_20	Half-sat, M2 on M1 to M2 activation	142177
kbasal_20	Basal activation of M1 to M2	0.44
vf_20	Rate of activation of M1 to M2	0.323
k1_21	Half-sat, Th1 on M2 to M1 activation	98653
k2_21	Half-sat, M1 on M2 to M1 activation	132039
k3_21	Half-sat, eDC on M2 to M1 activation	129288
k4_21	Half-sat, Th17 on M2 to M1 activation	122968
kbasal_21	Basal activation of M2 to M1	1.21
vf_21	Rate of activation of M2 to M1	0.1
k1_25	Half-sat, eDC on iDC recruitment	24124
kbasal_iDC	Basal recruitment of iDC	1.4
vf_25	Rate of iDC recruitment	1
k2_25	Half-sat, M1 on iDC recruitment	32174
k1_26	Half-sat, IL10 on iDC activation to tDC	0.000431
kbasal_26	Basal rate of iDC activation to tDC	0.0123
k1_27	Half-max inhibition, IL10 on iDC activation to eDC	0.00153
k2_27	Half-max inhibition, TNFa on iDC activation to eDC	0.0528
k3_27	Half-max inhibition, IFNg on iDC activation to eDC	0.0176
k4_27	Half-max inhibition, IL6 on iDC activation to eDC	0.0023
kbasal_27	Basal rate of iDC activation to eDC	0.01
vf_27	Rate of iDC activation to eDC	0.023
vf_26	Rate of iDC activation to tDC	0.066
k2_31	IL12 production by M1	6.18E-09
kbasal_IL12	Basal production of IL12	0.0000171
k1_33	IFNg production by eDC	4.34E-08
k2_33	IFNg production by Th1	0.000000123
k3_33	IFNg production by NK1	0.000000488

kbasal_IFNg	Basal production of IFNg	0.000149966
k1_31	IL12 production by eDC	4.98E-09
k1_35	IL2 production by eDC	0.000000056
k2_35	IL2 production by Th1	0.000000002
kbasal_IL2	Basal production of IL2	0.0000368
fi12	Adjustment, IL4 on activated M1	2.49
k3_31	IL12 production by M0	3.36E-11
w_17	Weight of M1 and M2 recruitment of M0	0.13
k2_5	Half-sat, M1 on Treg differentiation	18900
k1_63	Half-sat, M1 on Th0 proliferation	12045
vf_63	Rate of Th0 proliferation	0.49
k1_37	IL6 production by eDC	1.97E-09
k2_37	IL6 production by Th17	4.46E-09
k3_37	IL6 production by M1	5.17E-10
k4_37	IL6 production by Neu_act	3.87E-11
kbasal_IL6	Basal production of IL6	0.002
k1_39	IL23 production by eDC	0.000000065
k2_39	IL23 production by M1	0.00000031
k3_39	IL23 production by Neu_act	6.85E-11
kbasal_IL23	Basal production of IL23	0.0000226
k1_41	IL21 production by Th17	0.0000005
k2_41	IL21 production by NKT	0.00000011
kbasal_IL21	Basal IL21 production	0.0000551
k1_43	TGFb production by Th17	0.000000742
k2_43	TGFb production by Treg	0.000000715
k3_43	TGFb production by NKT	0.000000224
k4_43	TGFb production by M2	0.000000477
kbasal_TGFb	Basal production of TGFb	0.00381
k1_45	IL10 production by Treg	1.91E-09
k2_45	IL10 production by NKT	0.000000004
kbasal_IL10	Basal production of IL10	0.0000515
k1_47	TL1A production by Th1	0.000000562
k2_47	TL1A production by eDC	0.000000462
kbasal_TL1A	Basal production of TL1A	0.047
k1_49	IL13 production by Th2	4.79E-09
k2_49	IL13 production by NKT	4.61E-09
kbasal_IL13	Basal production of IL13	0.0000757
k1_51	IL17 production by Th17	0.000000105
k2_51	IL17 production by NKT	3.45E-09
kbasal_IL17	Basal production of IL17	0.0000921
k1_53	IL5 production by Th2	6.22E-09
k2_53	IL5 production by NKT	6.6E-10
kbasal_IL5	Basal production of IL5	0.0000204
k1_55	IL4 production by Th2	1.07E-08
k2_55	IL4 production by NKT	1.76E-09
kbasal_IL4	Basal IL4 production	0.0000322
k1_57	IL15 production by M2	1.28E-08
kbasal_IL15	Basal IL15 production	0.0000348
k3_55	IL4 production by Th0	9.8E-11
k3_45	IL10 production by tDC	3.72E-09

k4_45	IL10 production by M2	2.33E-09
k4_20	Half-sat, IL10 on M1 to M2 activation	0.005536
c72	Half-sat, IL10 on M2 production of IL10	0.002084
ci72	Adjustment, IFNg on IL10 effect on M2 production of IL10	0.0477
k1_68	Adjustment, TGFb on Th17 differentiation to Th1	1.729
k2_68	Half-sat, IL12 on Th17 differentiation to Th1	0.0000163
kbasal_68	Basal differentiation of Th17 to Th1	0.1
vf_68	Rate of differentiation of Th17 to Th1	0.1
k1_69	Half-sat, IL4 on Th17 differentiation to Th2	0.0000588
kbasal_69	Basal differentiation of Th17 to Th2	0.1
vf_69	Rate of differentiation of Th17 to Th2	0.1
k1_70	Half-sat, IL12 on Treg differentiation to Th1	0.000346
kbasal_70	Basal differentiation of Treg to Th1	0.1
vf_70	Rate of differentiation of Treg to Th1	0.1
kbasal_NK	Basal production of NK	10250
vf_72	Rate of NK to NK1 differentiation	0.0014
k1_72	Half-sat, IL15 on NK to NK1 differentiation	0.000385
kbasal_72	Basal NK to NK1 differentiation	0.5
k1_73	Half-sat, IL23 on NK to NK2 differentiation	0.0005
kbasal_73	Basal NK to NK2 differentiation	0.3
vf_73	Rate of NK to NK2 differentiation	0.0008
kdeg_IL22	Degradation of IL22	2.45
k1_74	IL22 production by NK2	0.00000203
kbasal_IL22	Basal production of IL22	0.0000583
k1_76	Half-sat, IL12 on NKT production	0.000495
k2_76	Half-sat, IL18 on NKT production	0.001435
k3_76	Half-sat, eDC on NKT production	11015
kbasal_NKT	Basal NKT production	0.763
vf_76	Rate of NKT production	0.962
k2_64	Half-sat, Treg on Th1 proliferation	134103
vf_64	Rate of Th1 proliferation	0.001
k2_65	Half-sat, Treg on Th2 proliferation	10063
vf_65	Rate of Th2 proliferation	0.000863
vf_66	Rate of Th17 proliferation	0.000948
k2_67	Half-sat, tDC on Treg proliferation	73114
k3_67	Half-sat, GMCSF on Treg proliferation	0.00166
vf_67	Rate of Treg proliferation	0.000707
kdeg_eDC	Degradation rate of eDC	0.025
k1_67	Half-Sat, IL2 effect on Treg proliferation	0.00205
kdeg_TNFa	Degradation rate of TNFa	3.16
kdeg_TL1A	Degradation rate of TL1A	3.61
k1_65	Half-Sat, IL2 effect on Th2 proliferation	0.0000635
k1_66	Half-Sat, IL2 effect on Th17 proliferation	0.0000608
k1_64	Half-Sat, IL2 effect on Th1 proliferation	0.0000608
kdeg_TGFb	Degradation rate of TGFb	1.9
kdeg_tDC	Degradation rate of tDC	0.0118
kbasal_Treg	Basal production rate of Treg	0.125
kbasal_Th2	Basal production rate of Th2	0.09
kbasal_Th17	Basal production rate of Th17	0.128
kbasal_Th1	Basal production rate of Th1	0.1

kdeg_NKT	Basal production rate of NKT	0.0588
kdeg_NK2	Basal production rate of NK2	0.0674
kdeg_NK1	Basal production rate of NK1	0.0342
kdeg_NK	Basal production rate of NK	0.051774
kdeg_M2	Degradation rate of M2	0.067
kdeg_M1	Degradation rate of M1	0.075
kdeg_M0	Degradation rate of M0	0.044
kdeg_IL6	Degradation rate of IL6	35
kdeg_IL5	Degradation rate of IL5	3.003
kdeg_IL4	Degradation rate of IL4	3.95
kdeg_IL23	Degradation rate of IL23	2.17
kdeg_IL21	Degradation rate of IL21	1.913
kdeg_IL2	Degradation rate of IL2	1.89
kdeg_IL18	Degradation rate of IL18	1.98
kdeg_IL17	Degradation rate of IL17	2.11
kdeg_IL15	Degradation rate of IL15	2.5
kdeg_IL13	Degradation rate of IL13	2.73
kdeg_IL12	Degradation rate of IL12	1.22
kdeg_IL10	Degradation rate of IL10	3.59
kdeg_IFNg	Degradation rate of IFNg	4.26
kbasal_IL18	Basal production rate of IL18	0.0000613
kbasal_TNFa	Basal production rate of TNFa	0.0028
k1_61	TNFa production by M1	0.00000031
k2_61	TNFa production by M2	5.64E-08
k3_61	TNFa production by Th1	4.12E-08
k1_59	IL18 production by M1	0.0000014
k2_59	IL18 production by eDC	0.00000163
kbasal_IL8	Basal production of IL8	0.00086
kdeg_IL8	Degradation of IL8	3.07
k1_83	IL8 production by M1	1.07E-09
k2_83	IL8 production by Neu_act	4.29E-10
k1_85	GMCSF production by Th1	9.77E-10
k2_85	GMCSF production by Th2	1.15E-09
k3_85	GMCSF production by Th17	1.27E-08
k4_85	GMCSF production by M1	1.09E-08
k5_85	GMCSF production by M2	1.1E-09
kbasal_GMCSF	Basal production of GMCSF	0.00007949
kdeg_GMCSF	Degradation of GMCSF	1.24
Th0_blood_constant	Amount of Th0 available to move to the gut	121802
iDC_blood_constant	Amount of iDC available to move to the gut	310.5
NKT_constant	NKT production constant	1886
k5_45	IL10 production by NK1	3.16E-08
k4_55	IL4 production by NK2	6.49E-11
k3_k5	IL5 production by NK2	4.17E-10
k3_49	IL13 production by NK2	1.47E-08
KmProtSyn	Half-sat, IL6 on CRP production	0.0055
VmProtSynth	Rate of CRP production	163132
KmCalprotectin	Half-sat, Neu_Total on Calprotectin	7614680
VmCalprotectin	Rate of Calprotectin production	414
k5_37	Half-sat, TNFa on IL6 production	0.0112

kdeg_CRP	Degradation of CRP	0.618
kbasal_Neu	Basal production of Neu in Blood	7935430
kdeg_Neu	Degradation of Neu	3.3
kIL12_bloodtogut	Transport rate of IL12 from blood to gut	0
kIL12_guttoblood	Transport rate of IL12 from gut to blood	0.055
kIL17_bloodtogut	Transport rate of IL17 from blood to gut	0
kIL17_tissuetoblood	Transport rate of IL17 from gut to blood	1.31
kIL8_bloodtogut	Transport rate of IL8 from blood to gut	0
kIL8_guttoblood	Transport rate of IL8 from gut to blood	0.057
kTGFB_bloodtogut	Transport rate of TGFb from blood to gut	0
kTGFB_guttoblood	Transport rate of TGFb from gut to blood	0.88
k1_115	Half-sat, IFNg on activation of Neu	0.087
k2_115	Half-sat, TNFa on activation of Neu	0.051
kbasal_94	Basal transport of Neu from Blood to Gut	0.012
k3_115	Half-sat, GMCSF on activation of Neu	0.0047
vf_94	Rate of transport of Neu from Blood to Gut	0.4
k2_94	Half-sat, IL8 on transport of Neu from Blood to Gut	0.000563
kbasal_CRP	Basal level of CRP production	0.469
kCRP_LivertoBlood	Transport rate of CRP from liver to blood	0.884406
kCRP_BloodtoLiver	Transport rate of CRP from blood to liver	0.909
kCRPSecretion	Secretion of CRP from liver hepatocytes	0.475
kIL6_livertoblood	Transport rate of IL6 from liver to blood	0.693
kIL6_guttoblood	Transport rate of IL6 from gut to blood	0.009
kIL6_bloodtogut	Transport rate of IL6 from blood to gut	0
kIL6_bloodtoliver	Transport rate of IL6 from blood to liver	20.3
kbasal_IL8_b	Basal rate of IL8 production in the blood	0.003168
kTNFa_guttoblood	Transport rate of TNFa from gut to blood	0.0455
kTNFa_bloodtogut	Transport rate of TNFa from blood to gut	0
kbasal_TNFa_b	Basal rate of TNFa production in the blood	0.00577
kbasal_IL6_b	Basal rate of IL6 production in the blood	0.008
kbasal_TGFb_b	Basal rate of TGFb production in the blood	0.1655
kbasal_IL12_b	Basal rate of IL12 production in the blood	0.000286
kbasal_IL17_b	Basal rate of IL17 production in the blood	0.002335
kbasal_115	Basal activation of Neu	0.1
vf_115	Rate of Neu activation	0.9433
k4_115	Half-sat, IL8 on activation of Neu	0.037
k1_77	Half-sat, IL17 on Neu production in blood	0.01
k2_77	Half-sat, GMCSF on Neu production in blood	0.000821
kmax_IL6_b	Maximum IL6 production rate in the blood	0.0232
k1_94	Half-sat, TNFa on transport of Neu from Blood to Gut	0.086
k_IL6_neu	Half-sat, IL6 on Neu degradation rate in Gut	0.000914
Imax_Neu_deg	Max inhibition of IL6 on Neu degradation rate in Gut	0.5
kdeg_iDC	Degradation of iDC	0.019
kneu_guttoblood	Transport rate of Neu from gut to blood	0.185
k3_51	Half-sat, IL23 on Th17 production of IL17	0.0000514
k6_85	Half-sat, IL23 on Th17 production of GMCSF	0.00648
k2_74	IL22 production by Th17	0.00000027
k3_74	Half-sat, IL23 on Th17 production of IL22	0.003725
k6_37	Half-sat, IL17 on IL6 production	0.01
k7_85	Half-sat, IL17 on GMCSF production	0.000875

k7_37	Half-sat, IL23 on Th17 production of IL6	0.00126
k3_41	Half-sat, IL23 on Th17 production of IL21	0.000808
k_IL17_Th17	Basal rate of IL17 production by Th17	0.125
k_IL22_Th17	Basal rate of IL22 production by Th18	0.108
k4_33	Half-sat, IL12 on NK1 production of IFNg	0.001285
k_IFNg_NK1	Basal rate of IL12 production by NK1	0.0858
k_IL21_Th17	Basal rate of IL21 production by Th17 cells	0.16
k_GMCSF_IL23	Basal rate of GMCSF production by Th17 cells	0.075
k4_51	Half-sat, IL23 on NKT production of IL17	0.0000594
k_IL17_NKT	Basal rate of IL17 by NKT cells	0.097
gamma_IL8	Basal weight of IL8 production	0.008716
k1_114	Half-sat, M1 on TNFa production in the blood	19282
k2_114	Half-sat, M2 on TNFa production in the blood	173591
k3_114	Half-sat, Th1 on TNFa production in the blood	255758
k4_61	Half-sat, IL17 on TNFa production	0.00678
k8_85	Half-sat, TNFa on GMCSF production	0.012
k3_83	Half-sat, IL17 on IL8 production	0.011
k4_83	Half-sat, TNFa on IL8 production	0.011
gamma_TNFa	Basal weight of TNFa production	0.129
k_epidam	Half-sat, IL17 effect on Epthelial Damage	0.00025
gamma_TGFb	Basal weight of TGFb production	0.1
k1_107	Half-sat, Th17 on TGFb production in the blood	100000
k2_107	Half-sat, Treg on TGFb production in the blood	100000
k3_107	Half-sat, NKT on TGFb production in the blood	150000
k4_107	Half-sat, M2 on TGFb production in the blood	150000
gamma_IL12	Basal weight of IL12 production	0.1
k1_104	Half-sat, eDC on IL12 production in the blood	150000
k2_104	Half-sat, M1 on IL12 production in the blood	150000
k3_104	Half-sat, M0 on IL12 production in the blood	15000
gamma_IL17	Basal weight of IL17 production	1
gamma_damage	Rate effect of epithelial damage on activation of M0 and iDC	10
alpha_damage_par	Coefficient of Damage	0
A_V	Rate of production of DAMPs	0.8
k_int	Rate of damage by DAMPs	4.73E-12
km_int_IFNb	IC50 for anti-damage effect of Type I IFN	36
b_V	Clearance rate of DAMPs	0.00555
k_V_innate	Irradiated cell clearance by phagocytic immune cells	1E-11
mu_AT2	Rate constant for basal regeneration of AT2	0.000267417
k_ROS_AT2	Rate constant for ROS-induced damage of healthy cells	0.00000032
km_ROS_AT2	IC50 for ROS-induced damage of healthy cells	50000000000
k_AT1_AT2	Rate constant for basal differentiation of AT2 to AT1	0.000106967
km_AT1_AT2	Half-sat for differentiation of AT2 to AT1	0.9
k_IFNb_kill	Rate constant for induction of CD8+ irradiated cell clearance by Type I IFN	1.1
k_kill	Rate constant for irradiated cell clearance by CD8+ cell clearance	1.84E-09
km_kill	IC50 for induction of CD8+ irradiated cell clearance by Type I IFN	500000
b_AT2	Death rate for AT2 cells	0.00016045
b_I	Death rate for irradiated cells	0.015
mu_AT1	Rate constant for regeneration for AT1 cells (options)	0

k_ROS_AT1	Rate constant for ROS-induced damage of healthy AT1 cells	1
km_ROS_AT1	EC50 for ROS-induced damage of healthy AT1 cells	1
b_AT1	Death rate for AT1 cells	0.00016045
b_dAT1	Death rate for damaged AT1 cells	0.05
k_damage_TNFa	Rate constant for TNF- α induced damage	0.01
km_damage_TNFa	IC50 for TNF- α induced damage	319334.4
k_damage_IL6	Rate constant for IL-6 induced damage	0.01
km_damage_IL6	IC50 for IL-6 induced damage	11592
k_damage_IL1b	Rate constant for IL-1 β induced damage	0.01
km_damage_IL1b	IC50 for IL-1 β induced damage	1727404.56
k_damage_IFNg	Rate constant for IFN γ induced damage	0.01
km_damage_IFNg	IC50 for IFN γ induced damage	53222.4
k_damage_cyt	Rate constant overall cytokine damage	0.05
k_mu_AT2	Rate constant for threshold regeneration of AT2	30
k_diff_AT1	Rate constant for threshold differentiation of AT2 to AT1	30
a_DC	Rate constant for production of mature dendritic cells	115000000
kbasal_DC	Basal activation of dendritic cells	0
b_DC	Death rate for mature dendritic cells	0.001041667
k_DC_TNFa	Rate constant for maturation of dendritic cells by TNF- α	10
km_DC_TNFa	EC50 for maturation of dendritic cells by TNF- α	3193.344
k_DC_IFNg	Rate constant for maturation of dendritic cells by IFN γ	10
km_DC_IFNg	EC50 for maturation of dendritic cells by IFN γ	1064.448
k_DC_IL6	Rate constant for maturation of dendritic cells by IL-6	10
km_DC_IL6	EC50 for maturation of dendritic cells by IL-6	139.104
km_DC_IL10	IC50 for inhibition of DC activation by IL-10	46.2672
a_M1	Rate constant for activation of macrophages	400000000
kbasal_M1	Rate constant for basal activation of macrophages	0
k_v	Rate constant for innate immune activation by DAMPs	0.3
k_I	Rate constant for innate immune activation by irradiated cells	0.03
k_dAT	Rate constant for innate immune activation by damaged cells	0.3
km_v	EC50 for innate immune activation by DAMPs	5E+11
km_I	EC50 for innate immune activation by irradiated cell	5000000000
km_dAT	EC50 for innate immune activation by damaged cells	5000000000
k_M1_IL6	Rate constant for macrophage activation by IL-6	10
km_M1_IL6	EC50 for macrophage activation by IL-6	139.104
b_M1	Death rate of activated macrophages	0.002791667
k_M1_TNFa	Rate constant for macrophage activation by TNF	10
km_M1_TNFa	EC50 for macrophage activation by TNF	3200.6016
k_M1_GMCSF	Rate constant for macrophage activation by GM-CSF	10
km_M1_GMCSF	EC50 for macrophage activation by GM-CSF	567.3024
k_M1_IFNg	Rate constant for macrophage activation by IFN	10
km_M1_IFNg	EC50 for macrophage activation by IFN	800.1504
km_M1_IL10	IC50 for inhibition of macrophage activation by IL-10	167.40864
kbasal_N	Basal recruitment of activated neutrophils	0
a_N	Rate constant for activation of neutrophils	79354300000
k_N_IFNg	Rate constant for neutrophil activation by IFN	10
km_N_IFNg	EC50 for neutrophil activation by IFN	53222.4
k_N_TNFa	Rate constant for neutrophil activation by TNF	0.1
km_N_TNFa	EC50 for neutrophil activation by TNF	5261.76
k_N_GMCSF	Rate constant for neutrophil activation by GM-CSF	1

km_N_GMCSF	EC50 for neutrophil activation by GM-CSF	725.76
k_N_IL17c	Rate constant for neutrophil recruitment by IL-17	10
km_N_IL17c	EC50 for neutrophil recruitment by IL-17	2237.76
b_N	Death rate of activated neutrophils	0.618003353
a_Th1	Rate constant for activation of Th1 cells	0.02
b_Th1	Death rate for activated Th1 cells	0.019629167
k_Th1_IL2	Rate constant for activation of by Th1 cells by IL-2	1.5
K_Th1_IL12	EC50 for activation of Th1 cells by IL-2	0.501984
k_Th1_IL12IL2	Rate constant for induction of IL-2 activity for activation of Th1 cells by IL-12	2
K_Th1_IL12IL2	EC50 for activation of Th1 cells by IL-12	7.52976
K_Th1_IL10	IC50 for inhibition of activated Th1 cells by IL-10	32516.12903
K_Th1_TGFb	IC50 for inhibition for activated Th1 cells by TGF	1832727.273
k_Th1_IFNg	Rate constant for activation of Th1 cells by IFN	1
K_IFNg_Th1	EC50 for activation of Th1 cells by IFN	931.392
K_Th1_IL6	EC50 for inhibition of Th1 activation by IL-6	267610.6195
k_Th1_Th17	Rate constant for differentiation of activated Th17 cells to Th1 cells	0.01
K_Th1_Th17	EC50 for differentiation of activated Th17 cells to Th1 cells	0.0328608
k_Th1_Treg	Rate constant for differentiation of activated Treg cells to Th1 cells	0.005
K_Th1_Treg	EC50 for differentiation of activated Treg cells to Th1 cells	20.92608
a_Th17	Rate constant for activation of Th17 cells	0.0346
b_Th17	Death rate of activated Th17 cells	0.0216125
k_Th17_TGFb	Rate constant for activation of Th17 cells by TGF	4
K_Th17_TGFb	EC50 for activation of Th17 cells by TGF	638.372448
K_Th17_IL2	IC50 for inhibition of Th17 activation by IL-2	7032558.14
K_Th17_IFNg	IC50 for inhibition of Th17 activation by IFN	6833898.305
K_Th17_IL10	IC50 for inhibition of Th17 activation by IL-10	1359101.124
k_Th17_IL6	Rate constant for Th17 activation by IL-6	1
km_Th17_IL6	EC50 for Th17 activation by IL-6	42.336
k_Th17_IL1b	Rate constant for Th17 activation by IL-1	1
km_Th17_IL1b	EC50 for Th17 activation by IL-1	20728.85472
a_CTL	Rate constant for CTL activation	0.0007215
b_CTL	Death rate of activated CTL	0.00245
k_CTL_IL2	Rate constant for CTL activation by IL-2	3
K_CTL_IL12	EC50 for CTL activation by IL-12	7.52976
k_CTL_IL12IL2	Rate constant for CTL activation by IL-12	4
K_CTL_IL12IL2	EC50 for CTL activation by IL-12	7.52976
K_CTL_IL10	IC50 for inhibition of CTL activation by IL-10	32516.12903
K_CTL_TGFb	IC50 for inhibition of CTL activation by TGF	1832727.273
K_CTL_IL6	IC50 for inibition of CTL activation by IL-5	535221.2389
k_CTL_IFNg	Rate constant for CTL activation by IFN	1
K_CTL_IFNg	EC50 for CTL activation by IFN	931.392
kmax_MHC1	Rate constant for Type I interferon & MHC-1 induced activation of CTL	1
km_MHC1_IFNb	EC50 for Type I interferon & MHC-1 induced activation of CTL	5
a_Treg	Rate constant for Treg activation	0.02
b_Treg	Death of activated Treg cells	0.014791667
k_Treg_IL2	Rate constant for Treg activation by IL-2	1
K_Treg_IL2	EC50 for Treg activation by IL-2	1.796256

K_Treg_IL17	IC50 constant for Treg inhibition by IL-17	491707.3171
K_Treg_IL6	IC50 constant for Treg inhibition by IL-6	535221.2389
k_Treg_TGFb	Rate constant for Treg activation by TGF	1
K_Treg_TGFb	EC50 for Treg activation by TGF	32.256
kbasal_SPD	Basal SP-D production rate	40
a_SPD	Rate constant for SP-D production by damaged and irritated alveolar cells	5.00E-07
b_SPD	Clearance rate of SP-D	0.069315
a_tnf	Basal induction Rate of TNF	0.012975984
a_tnf_at1	Production rate of TNF by damaged AT1 cells	0.00014
a_tnf_i	Production rate of TNF by irradiated AT2 cells	0.000056
a_tnf_at2	Production rate of TNF by damaged AT2 cells	0.00014
a_tnf_m1	Production rate of TNF by activated macrophages	0.000042
a_tnf_th1	Production of TNF by activated Th1 cells	1.13E-09
a_tnf_th17	Production of TNF by activated Th17 cells	1.13E-09
b_tnf	Clearance rate of TNF	3.16
a_il6	Basal induction rate of IL-6	0.00056448
b_il6	Clearance rate of IL-6	0.044
a_il6_at1	Production rate of IL-6 by damaged AT1 cells	0.00000312
a_il6_i	Production rate of IL-6 by irradiated AT2 cells	0.00000125
a_il6_at2	Production rate of IL-6 by damaged AT2 cells	0.00000312
a_il6_m1	Production rate of IL-6 by activated macrophages	0.00000145
a_il6_th17	Production of IL-6 by activated Th17 cells	0.00000125
a_il6_neu	Production of IL-6 by activated neutrophils	0.000000108
a_ifng	Basal induction rate of IFN	0.126979181
b_ifng	Clearance rate of IFN	3.59
a_ifng_dc	Production of IFN by mature dendritic cells	2.17E-09
a_ifng_th1	Production of IFN by activated Th1 cells	0.000000615
a_ifng_ctl	Production of IFN by activated CTL	0.0000293
a_ifnb	Basal induction of Type I IFN	0.031744795
b_ifnb	Clearance rate of Type I IFN	3.59
a_ifnb_at1	Production of Type I IFN by damaged AT1 cells	0.00004
a_ifnb_i	Production of Type I IFN by irradiated AT2 cells	0.00007
a_ifnb_d	Production of Type I IFN by damaged cells	0.0001
a_ifnb_dc	Production of Type I IFN by mature dendritic cells	0.00007
a_il2_dc	Production of IL-2 by mature dendritic cells	0.000000056
a_il2_th1	Production of IL-2 by activated Th1 cells	0.00000002
b_il2	Clearance rate of IL-2	1.913
a_il2	Basal induction rate of IL-2	25.96608
a_il12_m1	Production rate of IL-2 by activated macrophages	6.18E-08
a_il12_dc	Production rate of IL-2 by mature dendritic cells	4.98E-08
b_il12	Clearance rate of IL-12	2.73
a_il12	Basal induction of IL-12	48.26304
a_il17_th17	Production rate of IL-17 by activated Th17 cells	0.0000105
a_il17_ctl	Production rate of IL-17 by activated CTL	3.45E-09
b_il17	Clearance rate of IL-17	0.0825
a_il17	Basal induction rate of IL-17	0.12997152
a_il10_treg	Production rate of IL-10 by Treg cells	0.0000115
b_il10	Clearance rate of IL-10 by Treg cells	1.22
a_il10	Basal induction rate of IL-10	0.272538
a_tgfb_th17	Production rate of TGF by activated Th17 cells	0.00000742

a_tgfb_treg	Production rate of TGF by activated Treg cells	0.00000715
b_tgfb	Clearance rate of TGF	1.9
a_tgfb	Basal induction rate of TGF	2.1506688
a_gmcsf_m1	Production rate of GM-CSF by activated macrophages	0.00000127
a_gmcsf_th1	Production rate of GM-CSF by activated Th1 cells	4.29E-08
a_gmcsf_th17	Production ratio of GM-CSF by activated Th17 cells	0.000000115
b_gmcsf	Clearance rate of GM-CSF	1
a_gmcsf	Basal induction of GM-CSF	15.5232
a_il1b	Basal induction rate of IL-1	0.084672
b_il1b	Clearance rate of IL-1	0.088
a_il1b_at1	Production rate of IL-1 by damaged AT1 cells	5.17E-10
a_il1b_i	Production rate of IL-1 by irradiated AT1 cells	2.07E-09
a_il1b_at2	Production rate of IL-1 by damaged AT2 cells	5.17E-09
a_il1b_m1	Production rate of IL-1 by activated macrophages	2.07E-08
a_il1b_dc	Production rate of IL-1 by mature dendritic cells	0
kbasal_ROS	Basal Production rate of reactive oxygen species (ROS)	0
b_ROS	Clearance rate of ROS	0
basal_tnfa	Basal Production rate of TNF	24
basalil6	Basal Production rate of IL-6	40
basalil1	Basal Production rate of IL-1	5.714285714
basalifng	Basal Production rate of IL-1	20
basalifnb	Basal Production of Type I IFN	8
basalil2	Basal Production rate of IL-2	4
basalil12	Basal Production of IL-12	1.2
basalil10	Basal Production rate of IL-10	10
basaltgfb	Basal Production rate of TGF	1
basalgmcsf	Basal Production of GM-CSF	4
ktr_TNFa	Transport rate of TNF from lung to blood compartment	0.1
ktr_IL6	Transport rate of IL-6 from lung to blood compartment	0.1
ktr_IL1b	Transport rate of IL-1 from lung to blood compartment	0.1
ktr_IFNb	Transport rate of Type I IFN from lung to blood compartment	0.1
ktr_IFNg	Transport rate of IFN from lung to blood compartment	0.1
ktr_IL2	Transport rate of IL-2 from lung to blood compartment	0.2
ktr_IL12	Transport rate of IL-12 from lung to blood compartment	0.1
ktr_IL17	Transport rate of IL-17 from lung to blood compartment	0.1
ktr_IL10	Transport rate of IL-10 from lung to blood compartment	0.1
ktr_TGFb	Transport rate of TGF from lung to blood compartment	0.1
ktr_GMCSF	Transport rate of GM-CSF from lung to blood compartment	0.1
Gut	Volume of Gut Compartment	933
Lung	Volume of Lung Compartment	2016
Blood	Volume of Blood Compartment	4500
Liver	Volume of Liver Compartment	1660

Table 8: List of all parameters in GLA model

6.2. Appendix 2: List of Weighted Parameters for CD and UC modes of the Gut model

Table 9 contains the list of parameters that vary between HV, CD and UC modes of the Gut model and their corresponding weights. The weights are multiplied with the original parameter value (Table 2) and the model is simulated with the new parameter values.

Parameter	Description	CD weight	UC weight
kbasal_Th0	basal production/transport of Th0 cells	1.3232	1.2815
kbasal_iDC	basal rate of production of iDC	0.70816	1.0587
kbasal_IL12	basal production of IL12	12.03	10.161
kbasal_IFNg	basal production of IFNg	1.477	2.3055
kbasal_IL2	basal production of IL2	0.40747	0.62802
kbasal_IL6	basal production of IL6	38.865	45.653
kbasal_IL23	basal production of IL23	2.761	1.7523
kbasal_IL21	basal production of IL21	1.4232	1.4249
kbasal_TGFb	basal production of TGFb	1.5605	1.2589
kbasal_IL10	basal production of IL10	1.9374	1.4905
kbasal_TL1A	basal production of TL1a	1.5048	1.4516
kbasal_IL13	basal production of IL13	1.2563	1.1232
kbasal_IL17	basal production of IL17	1.6542	0.76111
kbasal_IL5	basal production of IL5	0.76665	1.3089
kbasal_IL4	basal production of IL4	0.81628	0.56996
kbasal_IL15	basal production of IL15	3.1125	0.95477
kbasal_IL18	basal production of IL18	0.82712	0.86236
kbasal_TNFa	basal production of TNFa	51.606	15.752
kbasal_NK	basal production/transport of NK cells	0.65321	0.88643
kbasal_IL22	basal production of IL22	3.7278	86.925
kbasal_NKT	basal production of NKT	0.81046	0.48696
kbasal_Neu	basal production of Neu	1.3929	0.7581
kbasal_IL8	basal production of IL8	6.1081	5.08
kbasal_GMCSF	base production of GMCSF	0.79432	0.98607

Table 9: List of weighted parameters for CD and UC modes of the Gut model

6.3. Appendix 3: Simulation of Gut Model

Figure 23 shows the dynamics of the simulations of the gut model for the immune cell populations and cytokines.

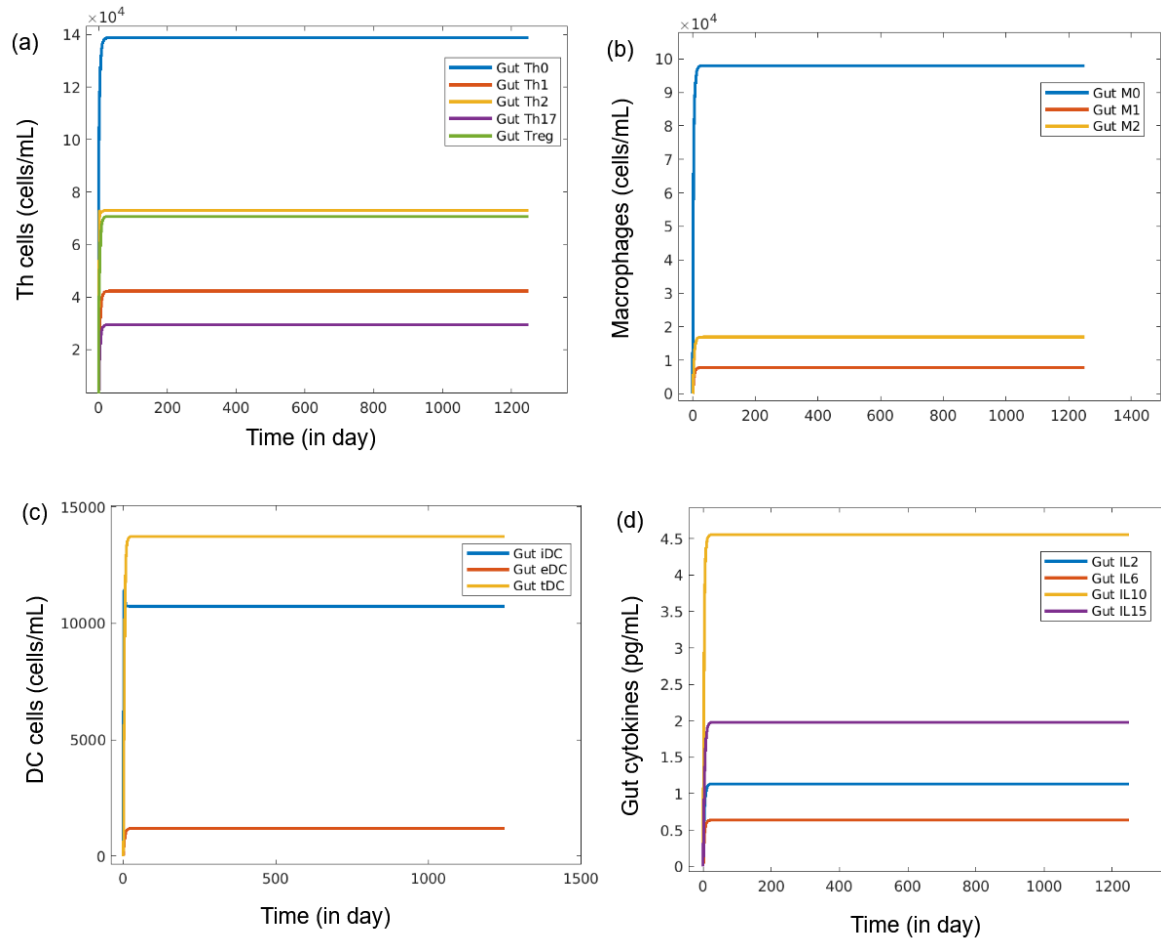


Figure 23: Time Evolution of immune cell population and cytokines for the Gut model. The dynamics of the simulation of gut model for helper T cell subpopulations (a), macrophage subpopulations (b), dendritic cell (DC) subpopulations and cytokines (d) indicate that the model reaches steady state at the end of the simulation.

6.4. Appendix 4: Sensitivity Analysis of Gut Model

Table 10 and Table 11 shows the description of parameters identified in the sensitivity analysis of state variables Blood_CRP and Gut_Neu_act in the Gut model respectively.

Parameter	Description
kdeg_IL6	Degradation rate of IL6
kmax_IL6_b	Maximum IL6 production rate in the blood
KmProtSyn	Half-sat, IL6 on CRP production
kIL6_bloodtoliver	Transport rate of IL6 from blood to liver
kdeg_IL17	Degradation rate of IL17
kbasal_IL17_b	Basal rate of IL17 production in the blood
k6_37	Half-sat, IL17 on IL6 production
VmProtSynth	Rate of CRP production
kCRP_LivertoBlood	Transport rate of CRP from liver to blood
kdeg_TNFa	Degradation rate of TNFa
k5_37	Half-sat, TNFa on IL6 production
gamma_IL17	Basal weight of IL17 production
kbasal_TNFa_b	Basal rate of TNFa production in the blood
kCRP_BloodtoLiver	Transport rate of CRP from blood to liver
vf_5	Rate of Th0 Production
Th0_blood_constant	Amount of Th0 available to move to the gut
kdeg_M0	Degradation rate of M0
kbasal_Th0	Basal production rate of Th0
kdeg_CRP	Degradation of CRP
kbasal_M0	Basal recruitment of M0
kdeg_M2	Degradation rate of M2
kdeg_Th1	Degradation rate of Th1
vf_19	Rate of activation of M0 to M2
kdeg_Th0	Degradation rate of Th0
vf_21	Rate of activation of M2 to M1

Table 10: Description of the top 25 sensitive parameters from the sensitivity analysis of CRP in blood of the Gut model

Parameter	Description
kdeg_Neu	Degradation of Neu
vf_5	Rate of Th0 Production
Th0_blood_constant	Amount of Th0 available to move to the gut
kbasal_Th0	Basal production rate of Th0
kbasal_Neu	Basal production of Neu in Blood
vf_94	Rate of transport of Neu from Blood to Gut
vf_115	Rate of Neu activation
kdeg_M0	Degradation rate of M0
kdeg_Th0	Degradation rate of Th0
kbasal_M0	Basal recruitment of M0
kdeg_Th1	Degradation rate of Th1
kdeg_M2	Degradation rate of M2
k2_94	Half-sat, IL8 on transport of Neu from Blood to Gut
kbasal_IL8	Basal production of IL8
vf_19	Rate of activation of M0 to M2
vf_21	Rate of activation of M2 to M1
kbasal_115	Basal activation of Neu
vf_20	Rate of activation of M1 to M2
kdeg_Th17	Degradation rate of Th17
vf_1	Rate of Th0 to Th1 differentiation
kdeg_IL8	Degradation of IL8
kdeg_M1	Degradation rate of M1
kbasal_21	Basal activation of M2 to M1
kdeg_TNFa	Degradation rate of TNFa
vf_18	Rate of activation of M0 to M1

Table 11: Description of the top 25 sensitive parameters from the sensitivity analysis of gut activated neutrophils of the Gut model

6.5. Appendix 5: Simulation of Lung Model

Figure 24 shows the dynamics of the simulations of the lung model for the pulmonary alveolar and immune cell populations, and cytokines.

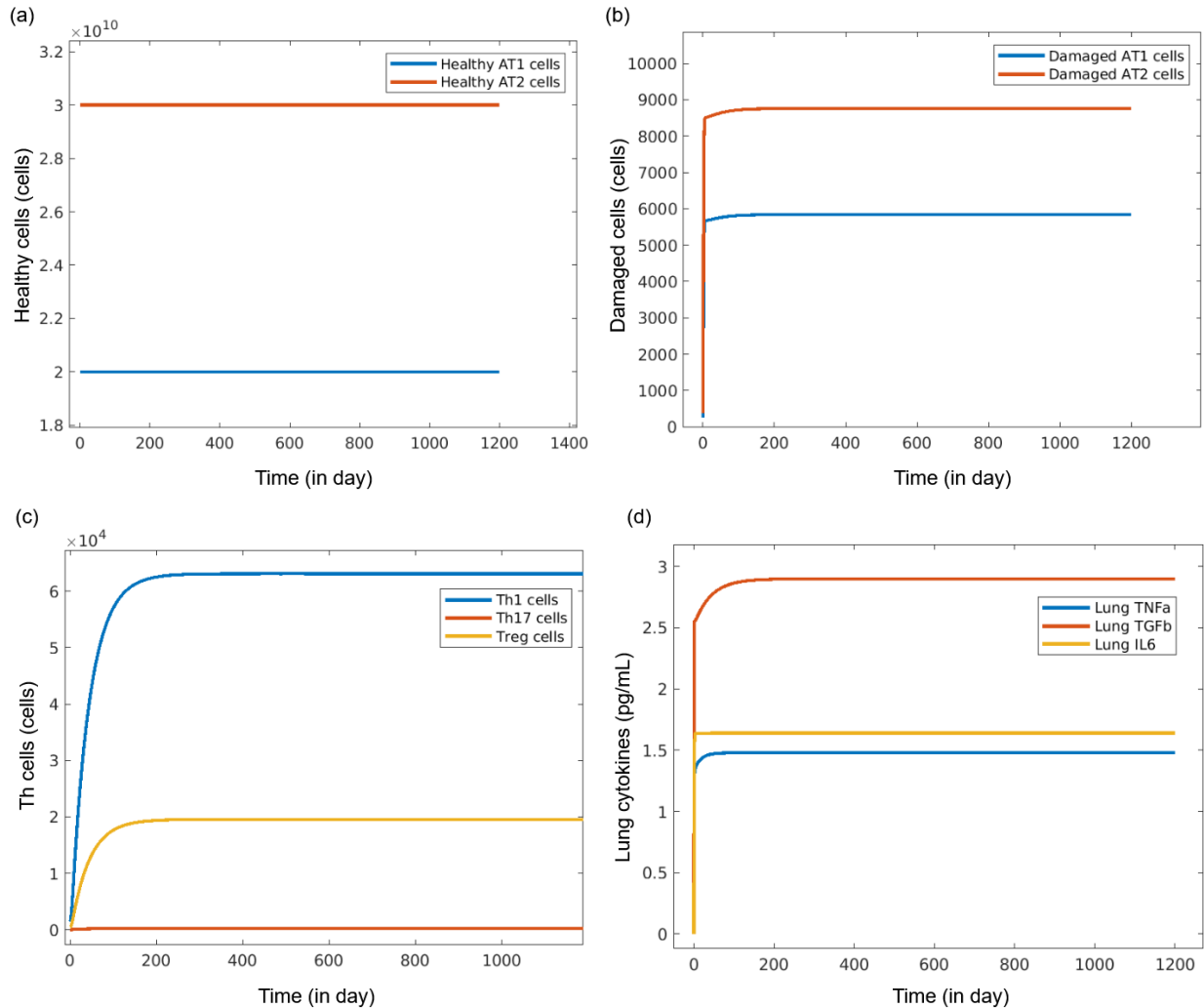


Figure 24: Time Evolution of pulmonary alveolar population, immune cell population and cytokines for the Lung model. The dynamics of the simulation of lung model for healthy AT1 and AT2 cells (a, blue and red respectively), damaged AT1 and AT2 cells (b, blue and red respectively), T cell subpopulations (c) and cytokines (d) indicate that the model reaches steady state at the end of the simulation.

6.6. Appendix 6: Sensitivity Analysis of Lung Model

Table 12, Table 13 and Table 14 shows the description of parameters identified in the sensitivity analysis of state variables Blood_CRP, Blood_SPD and dAT2 in the Lung model respectively.

Parameter	Description
kbasal_CRP	Basal level of CRP production
kdeg_CRP	Degradation of CRP
b_il6	Clearance rate of IL-6
kCRP_BloodtoLiver	Transport rate of CRP from blood to liver
a_il6	Basal induction rate of IL-6
k_livercrp	Secretion of CRP from liver hepatocytes
kCRP_LivertoBlood	Transport rate of CRP from liver to blood
basalil6	Basal Production rate of IL-6
ktr_IL6	Transport rate of IL-6 from alveolar to plasma compartment
mu_AT2	Rate constant for basal regeneration of AT2
k_damage_cyt	Rate constant overall cytokine damage
b_dAT1	Death rate for damaged AT1 cells
k_dAT	Rate constant for innate immune activation by damaged cells
km_dAT	EC50 for innate immune activation by damaged cells
a_M1	Rate constant for activation of macrophages
a_ifng	Basal induction rate of IFN γ
k_damage_IFN γ	Rate constant for IFN γ induced damage
km_damage_IFN γ	IC50 for IFN γ induced damage

Table 12: Description of the top 20 sensitive parameters from the sensitivity analysis of CRP in blood of the Lung model

Parameter	Description
mu_AT2	Rate constant for basal regeneration of AT2
k_damage_cyt	Rate constant overall cytokine damage
b_dAT1	Death rate for damaged AT1 cells
a_SPD	Basal induction rate of SPD
ktr_SPD	Transport rate of SPD from alveolar to plasma compartment
a_ifng	Basal induction rate of IFN γ
k_damage_IFN γ	Rate constant for IFN γ induced damage
km_damage_IFN γ	IC50 for IFN γ induced damage
k_damage_IL6	Rate constant for IL-6 induced damage
a_il6	Basal induction rate of IL-6
basalil6	Basal Production rate of IL-6
km_damage_IL6	IC50 for IL-6 induced damage
b_ifng	Clearance rate of IFN γ
basalifng	Basal Production rate of IFN γ

ktr_IL6	Transport rate of IL-6 from alveolar to plasma compartment
b_il6	Clearance rate of IL-6
a_il1b	Basal induction of IL-1 β
k_damage_IL1b	Rate constant for IL-1 β induced damage
basalil1	Basal Production rate of IL-1
km_damage_IL1b	IC50 for IL-1 β induced damage

Table 13: Description of the top 20 sensitive parameters from the sensitivity analysis of SPD in blood of the Lung model

Parameter	Description
mu_AT2	Rate constant for basal regeneration of AT2
k_damage_cyt	Rate constant overall cytokine damage
b_dAT1	Death rate for damaged AT1 cells
a_ifng	Basal induction rate of IFN
k_damage_IFNg	Rate constant for IFN γ induced damage
km_damage_IFNg	IC50 for IFN γ induced damage
km_damage_IL6	IC50 for IL-6 induced damage
a_il6	Basal induction rate of IL-6
basalil6	Basal Production rate of IL-6
km_damage_IL6	IC50 for IL-6 induced damage
b_ifng	Clearance rate of IFN
basalifng	Basal Production rate of IFN γ
km_AT1_AT2	Half-sat for differentiation of AT2 to AT1
ktr_IL6	Transport rate of IL-6 from alveolar to plasma compartment
b_il6	Clearance rate of IL-6
a_il1b	Basal induction of IL-1 β
k_damage_IL1b	Rate constant for IL-1 β induced damage
basalil1	Basal Production rate of IL-1
km_damage_IL1b	IC50 for IL-1 β induced damage
k_dAT	Rate constant for innate immune activation by damaged cells

Table 14: Description of the top 20 sensitive parameters from the sensitivity analysis of damaged alveolar AT2 cells of the Lung model

6.7. Appendix 7: Flow Cytometric Data of Immune Populations from Mice

Table 15 describes the immune cell counts from the individual mice samples and the corresponding calculations.

Mice ID	Organ	Cell Type	Count Recorded	Total Immune Counts	Percentage	Average Percentage
Mice 1	Lungs	T cells	7118	30418	23.4	20.09
Mice 2	Lungs	T cells	4951	33277	14.88	
Mice 3	Lungs	T cells	8258	37545	21.99	
Mice 1	Lungs	Cytotoxic T cells	2106	30418	6.92	7.1
Mice 2	Lungs	Cytotoxic T cells	1333	33277	4.01	
Mice 3	Lungs	Cytotoxic T cells	3892	37545	10.37	
Mice 1	Lungs	B cells	10751	30418	35.34	41.15
Mice 2	Lungs	B cells	15287	33277	45.94	
Mice 3	Lungs	B cells	15830	37545	42.16	
Mice 1	Lungs	NK cells	81	30418	0.27	0.26
Mice 2	Lungs	NK cells	66	33277	0.2	
Mice 3	Lungs	NK cells	121	37545	0.32	
Mice 1	Lungs	Neutrophils	9820	61459	15.98	14.52
Mice 2	Lungs	Neutrophils	12430	79703	15.6	
Mice 3	Lungs	Neutrophils	8531	71140	11.99	
Mice 1	Lungs	Monocytes	7021	61459	11.42	7.98
Mice 2	Lungs	Monocytes	4077	79703	5.12	
Mice 3	Lungs	Monocytes	5270	71140	7.41	
Mice 1	Lungs	Total Macrophages	13682	61459	22.26	19.49
Mice 2	Lungs	Total Macrophages	13893	79703	17.43	
Mice 3	Lungs	Total Macrophages	13366	71140	18.79	
Mice 1	Lungs	Alveolar Macrophages	4157	48414	8.59	11.61
Mice 2	Lungs	Alveolar Macrophages	6299	50000	12.6	
Mice 3	Lungs	Alveolar Macrophages	6827	50000	13.65	
Mice 1	Lungs	Interstitial Macrophages	8210	48414	16.96	15.34
Mice 2	Lungs	Interstitial Macrophages	8292	50000	16.58	
Mice 3	Lungs	Interstitial Macrophages	6234	50000	12.47	
Mice 1	Blood	T cells	7427	48848	15.2	12.92
Mice 2	Blood	T cells	6887	65070	10.58	
Mice 3	Blood	T cells	6826	52614	12.97	
Mice 1	Blood	Cytotoxic T cells	4383	48848	8.97	6.08
Mice 2	Blood	Cytotoxic T cells	2694	65070	4.14	
Mice 3	Blood	Cytotoxic T cells	2703	52614	5.14	
Mice 1	Blood	Helper T cells	1977	48848	4.05	4.95
Mice 2	Blood	Helper T cells	3354	65070	5.15	
Mice 3	Blood	Helper T cells	2971	52614	5.65	
Mice 1	Blood	B cells	10742	48848	21.99	24.09
Mice 2	Blood	B cells	14558	65070	22.37	
Mice 3	Blood	B cells	14678	52614	27.9	

Mice 1	Blood	NK cells	239	48848	0.49	0.49
Mice 2	Blood	NK cells	143	65070	0.22	
Mice 3	Blood	NK cells	393	52614	0.75	
Mice 1	Spleen	T cells	13306	35824	37.14	38.71
Mice 2	Spleen	T cells	16169	39859	40.57	
Mice 3	Spleen	T cells	15974	41575	38.42	
Mice 1	Spleen	Cytotoxic T cells	6771	35824	18.9	16.94
Mice 2	Spleen	Cytotoxic T cells	6746	39859	16.92	
Mice 3	Spleen	Cytotoxic T cells	6233	41575	14.99	
Mice 1	Spleen	Helper T cells	4468	35824	12.47	16.17
Mice 2	Spleen	Helper T cells	7137	39859	17.91	
Mice 3	Spleen	Helper T cells	7543	41575	18.14	
Mice 1	Spleen	B cells	17831	35824	49.77	49.39
Mice 2	Spleen	B cells	18747	39859	47.03	
Mice 3	Spleen	B cells	21353	41575	51.36	
Mice 1	Spleen	NK cells	37	35824	0.1	0.06
Mice 2	Spleen	NK cells	11	39859	0.03	
Mice 3	Spleen	NK cells	17	41575	0.04	
Mice 1	Spleen	Dendritic Cells	1660	38535	4.31	3.71
Mice 2	Spleen	Dendritic Cells	1436	36452	3.94	
Mice 3	Spleen	Dendritic Cells	1114	38515	2.89	
Mice 1	Lymph Nodes	T cells	11180	25217	44.34	51.48
Mice 2	Lymph Nodes	T cells	16239	30334	53.53	
Mice 3	Lymph Nodes	T cells	19081	33724	56.58	
Mice 1	Lymph Nodes	Cytotoxic T cells	6034	25217	23.93	24.47
Mice 2	Lymph Nodes	Cytotoxic T cells	6560	30334	21.63	
Mice 3	Lymph Nodes	Cytotoxic T cells	9389	33724	27.84	
Mice 1	Lymph Nodes	Helper T cells	4011	25217	15.91	22.1
Mice 2	Lymph Nodes	Helper T cells	7902	30334	26.05	
Mice 3	Lymph Nodes	Helper T cells	8206	33724	24.33	
Mice 1	Lymph Nodes	B cells	9576	25217	37.97	38.96
Mice 2	Lymph Nodes	B cells	12206	30334	40.24	
Mice 3	Lymph Nodes	B cells	13045	33724	38.68	
Mice 1	Lymph Nodes	NK cells	6	25217	0.02	0.01
Mice 2	Lymph Nodes	NK cells	1	30334	0.003	
Mice 3	Lymph Nodes	NK cells	7	33724	0.02	
Mice 1	Lymph Nodes	Dendritic Cells	1285	42550	3.02	2.59
Mice 2	Lymph Nodes	Dendritic Cells	1412	42982	3.29	
Mice 3	Lymph Nodes	Dendritic Cells	657	44733	1.47	

Table 15: Calculations of immune cell population in different tissues of the individual mice samples. The table shows the immune cell type recorded by the flow cytometer present in the tissue sample of the corresponding mice ID. The averages shown in the above table are rounded off to the nearest two-digit decimals.

6.8. Appendix 8: Sensitivity Analysis of Gut-Lung Axis Model

Table 16 and Table 17 shows the description of parameters identified in the sensitivity analysis of state variables Blood_CRP and Blood_SPD in the Gut-Lung Axis model respectively.

Parameter	Description
kdeg_IL6	Degradation rate of IL6
KmProtSyn	Half-sat, IL6 on CRP production
kmax_IL6_b	Maximum IL6 production rate in the blood
kIL6_bloodtoliver	Transport rate of IL6 from blood to liver
kdeg_M0	Degradation rate of M0
k5_37	Half-sat, TNFa on IL6 production
k2_17	Recruitment of M0 induced by activated Macrophages
Th0_blood_constant	Amount of Th0 available to move to the gut
kCRP_LivertoBlood	Transport rate of CRP from liver to blood
vf_5	Rate of Th0 Production
kbasal_TNFa_b	Basal rate of TNFa production in the blood
kdeg_M2	Degradation rate of M2
VmProtSynth	Rate of CRP production
kCRP_LivertoBlood	Transport rate of CRP from liver to blood
kdeg_TNFa	Degradation rate of TNFa
kdeg_Th1	Degradation rate of Th1
vf_21	Rate of activation of M2 to M1
vf_20	Rate of activation of M1 to M2
kdeg_M1	Degradation rate of M1
kbasal_Th0	Basal production rate of Th0
vf_19	Rate of activation of M0 to M2
vf_18	Rate of activation of M0 to M1
kCRP_BloodtoLiver	Transport rate of CRP from blood to liver
kbasal_M0	Basal recruitment of M0
kbasal_IL17_b	Basal rate of IL17 production in the blood
k6_37	Half-sat, IL17 on IL6 production

Table 16: Description of the top 25 sensitive parameters from the sensitivity analysis of CRP in blood of the Gut-Lung Axis model

Parameter	Description
mu_AT2	Rate constant for basal regeneration of AT2
b_SPD	Clearance rate of SPD
k_damage_cyt	Rate constant overall cytokine damage
b_dAT1	Death rate for damaged AT1 cells
a_SPD	Basal induction rate of SPD
k_damage_IL6	Rate constant for IL-6 induced damage
km_damage_IL6	IC50 for IL-6 induced damage

kmax_IL6_b	Maximum IL6 production rate in the blood
a_il1b	Basal induction of IL-1 β
k_damage_IL1b	Rate constant for IL-1 β induced damage
km_damage_IL1b	IC50 for IL-1 β induced damage
a_il6	Basal induction rate of IL-6
basalil6	Basal Production rate of IL-6
b_ifng	Clearance rate of IFN
basalifng	Basal Production rate of IFN γ
kdeg_M0	Degradation rate of M0
kdeg_IL6	Degradation rate of IL6
k2_17	Recruitment of M0 induced by activated Macrophages
k5_37	Half-sat, TNFa on IL6 production
b_il6	Clearance rate of IL-6
Th0_blood_constant	Amount of Th0 available to move to the gut
vf_5	Rate of Th0 Production
kbasal_TNFa_b	Basal rate of TNFa production in the blood
kdeg_M2	Degradation rate of M2
kdeg_TNFa	Degradation rate of TNFa

Table 17: Description of the top 25 sensitive parameters from the sensitivity analysis of SPD in blood of the Gut-Lung Axis model